



Multiscale modeling of non-isothermal fluid transport in porous media

Applications to loop heat pipe evaporator and superheated steam drying

Dissertation

zur Erlangung des akademischen Grades

Doktoringenieur

(Dr.-Ing.)

von M.Sc. Kieu Hiep Le

geb. am 20.03.1985 in Ha Tinh, Vietnam

genehmigt durch die Fakultät für Verfahrens- und Systemtechnik

der Otto-von-Guericke-Universität Magdeburg

Promotionskommission:

Prof. Dr.-Ing. habil. Ulrich Krause	(Vorsitz)
Prof. Dr.-Ing. habil. Evangelos Tsotsas	(Gutachter)
Prof. Dr.-Ing. habil. Eckehard Specht	(Gutachter)
Dr. Nima Shokri	(Gutachter)

eingereicht am: 17.10.2017

Promotionskolloquium am: 12.03.2017

Acknowledgment

This work has been financially supported by Project No. 911, Ministry of Education and Training (MOET) of the Socialist Republic of Vietnam. I wish to express my deeply acknowledgment to MOET since its support was *vital*. I wish to express my heartfelt gratitude to my primary supervisor, **Prof. Dr.-Ing. Evangelos Tsotsas**, who gave me the opportunity to work at the Chair of Thermal Process Engineering. We had many fruitful discussions with large impact on the results of this work. It was my privilege to work at his chair.

I wish to express my acknowledgment to my immediate advisor, **Dr.-Ing. Abdolreza Kharaghani**, who directly mentored me all the time at the Chair of Thermal Process Engineering. Throughout my PhD project, he was a constant source of energy, ideas and enthusiasm. Not only my advisor, he also has been and is my big friend. A special thank goes to him for being an excellent mentor, as well as for his help, consultation and support in both my academic and non-academic life.

Moreover, I would like to warmly thank **Prof. Dr.-Ing. Eckehard Specht**, **Dr. Nima Shokri** for accepting to review my thesis, and **Prof. Dr.-Ing Ulrich Krause** for chairing my defense.

I express my thanks to **Dr. Christoph Kirsch** who co-authored several publications made during my PhD project. As a mathematician with a sharp and clear mind, he was my best critic. I also express my thanks to **Jun.-Prof. Dr.-Ing Andress Bück** and **Dr.-Ing. Neli Hampel** for their collaboration in wood particle experiments and their fruitful discussions during preparing our collaborative publications.

I am particularly indebted to **Dipl.-Phys. Diethardt Kürschner** who helped me to set up my experimental apparatus and to perform my experimental work. I also thank all my colleagues at the Chair of Thermal Process Engineering for the warmth they showed on me. We had a very friendly and relaxed atmosphere in our office as well as outside the university.

Last but not least, my whole hearted gratitude goes to my family who have been supporting me throughout my life. Without their unconditional love, encouragement and support, I would never have been able to come this far.

Non-isothermal fluid flow within a porous medium has been a subject of interest for decades in various fields such as heat pipes, superheated steam drying, vacuum contact drying, porous burners, transpiration cooling devices, to name only a few. It is still a very active field of research not only because of the continuous emergence of new applications, but also because fluid flow with phase transition in porous media is not yet completely understood. This work aims to provide a better fundamental understanding of non-isothermal liquid-vapor transport at both the continuum scale and the pore scale, and to pave the way for designing, operating and optimizing relevant industrial processes.

In the first part of this work, a two-dimensional pore network model is developed to study the steady state heat and mass transfer inside a capillary porous wick with opposite fluid and energy replenishment in dry-out operating regime. The porous medium is approximated by a network of cylindrical throats interconnected by pore nodes. The mass flow rate in each throat of the pore network is computed according to the Hagen-Poiseuille law, and the heat flux is calculated based on Fourier's law with an effective local thermal conductivity. By coupling the heat and the mass transfer, a numerical method is devised to determine the evolution of the liquid-vapor interface. The model is verified by comparing the tendency of effective heat transfer coefficient evolution over heat load with experimental observations. By performing a comparative assessment, a higher heat transfer is provided by water compared to methanol and ethanol. For increasing heat load, an inflation/deflation of the vapor pocket is observed. Via a sensitivity analysis, the influences of microstructural properties and operating parameters on the vapor pocket pattern and on the effective heat transfer coefficient are discussed. Moreover, several methods that can enhance the heat transfer efficiency such as creating vertical macro channels, attaching a fine porous layer with small pores at the top of the wick are also suggested.

This thesis also focuses on the heat and mass transfer involved in a capillary porous medium during the superheated steam drying process, which can be seen as a transient process. Firstly, a non-isothermal two-dimensional pore network model is developed to describe the superheated steam drying of a non-deformative capillary porous medium with impermeable solid phase. A main feature of this pore network model is the full treatment of condensed liquid by introducing new liquid invasion rules. Pores with volume are introduced in the network to remedy the overlap of neighboring throats which appears in

classical pore network model with volumeless pore nodes. During the network drying period, the liquid transport is driven by capillary action, whereas vapor transport occurs due to convection. The simulation results, presented as temperature and moisture content profiles over time, indicate qualitative agreement with available experimental observations. The inclusion of the new liquid invasion rules is shown to accommodate more of the condensed water mass compared to earlier models, in which condensation is only partly treated. Due to the viscous vapor flow, the vapor overpressure within the network, which is the driving force of vapor transport, is reproduced in these simulations. The influence of vapor overpressure on the disintegration of the liquid phase is also discussed.

Secondly, a continuum-scale model is developed to describe heat and mass transfer within a single hygroscopic porous particle with impermeable solid phase subjected to superheated steam drying. Key thermophysical properties of the wood particle, serving as drying sample, needed as input data of the continuum-scale model are determined experimentally. The continuum-scale model is validated against experimental data obtained by using a magnetic suspension balance. Then, the validated continuum-scale model is reduced into a lumped model, the so-called characteristic drying curve model, by establishing correlations of the lumped model parameters with the drying conditions, based on numerical results obtained from the continuum-scale model. Simulation results of both the sophisticated and the reduced model are validated by comparing against experimental data gained with a magnetic suspension balance system. The influence of drying conditions on the critical moisture content is also discussed in detail.

Lastly, the aforementioned continuous model is extended to describe the dynamics of heat and mass transfer in a cellular plant porous medium. This model accounts for advective liquid and vapor flows in the intercellular void space as well as for diffusive liquid flow across the solid cell membrane of the porous medium. The model is validated against drying experiments which were carried out by the magnetic suspension balance at three different superheated steam temperatures for potato samples. A comparison between simulations and the measurements shows that the drying characteristics can satisfactorily be predicted. The influence of cell membrane water conductivity on the spatio-temporal distribution of moisture content and temperature within the porous medium is studied by numerical simulations. It is pointed out that water diffusion across the cell membrane controls the dynamics of heat and mass transfer in the porous medium, and thus its drying kinetics.

Die nicht-isotherme Strömung innerhalb eines porösen Mediums wird seit Jahrzehnten in verschiedenen Bereichen wie z. B. Heißdampftrocknung, Vakuumkontakttrocknung, poröse Brenner, Wärmerohre, Transpirationskühlvorrichtungen untersucht. Dies ist ein sehr aktives Forschungsgebiet, nicht nur auf Grund des kontinuierlichen Auftretens neuer Anwendungen, sondern auch, weil das Verständnis über Transportvorgänge mit Phasenübergang in porösen Medien immer noch unvollständig ist. Das Ziel der Arbeit ist es daher, zum fundamentalen Verständnis nicht-isothermer Transportvorgänge sowohl im Kontinuums- als auch im Porenmaßstab beizutragen, und somit den Weg für die bessere Gestaltung, den effizienten Betrieb und die Optimierung entsprechender industrieller Prozesse zu ebnen.

Im ersten Teil dieser Arbeit wird ein zweidimensionales Porennetzwerkmodell entwickelt, um die stationäre Wärme- und Stoffübertragung innerhalb eines kapillarporösen Dochts mit entgegengesetzter Flüssigkeits- und Energie-Einspeisung im Austrocknungsbetrieb zu untersuchen. Das poröse Medium wird durch ein Netzwerk von zylindrischen Halsen approximiert, die durch Porenknoten miteinander verbunden sind. Der Massendurchsatz in jedem Hals des Porennetzwerkes wird nach dem Hagen-Poiseuille-Gesetz berechnet und der Wärmestrom wird auf Basis des Fourier-Gesetzes mit einer effektiven lokalen Wärmeleitfähigkeit ermittelt. Durch Kopplung der Wärme- und Stoffübertragung wird ein numerisches Verfahren zur Bestimmung der Evolution der Flüssig-Dampf-Grenzfläche entwickelt. Das Modell wird durch Vergleich der Veränderung des effektiven Wärmeübergangskoeffizienten mit der Wärmelast mit experimentellen Daten überprüft. Durch vergleichende Simulationen wird eine höhere Wärmeübertragung durch Wasser im Vergleich zu Methanol oder Ethanol festgestellt. Bei Erhöhung der Wärmebelastung wird eine Inflation/Deflation der Dampftasche beobachtet. Im Rahmen einer Sensitivitätsanalyse werden die Einflüsse von mikrostrukturellen Eigenschaften und Betriebsparametern auf die Dampftaschenkontur und auf effektiven Wärmeübergangskoeffizienten diskutiert. Darüber hinaus werden Maßnahmen vorgeschlagen, die die Wärmeübertragungseffizienz erhöhen können, beispielsweise die Anbringung von vertikalen Makrokanälen oder die Befestigung einer feinporösen Schicht mit kleineren Poren an der Oberseite des Dochts.

Die Arbeit konzentriert sich weiterhin auf die Wärme- und Stoffübertragung in einem kapillaren porösen Medium während der Trocknung mit überhitztem Dampf. Zuerst wird ein nicht-isothermes zweidimensionales Porennetzwerkmodell entwickelt, um die Heißdampftrocknung eines nicht verformbaren kapillarporösen Mediums mit

undurchlässiger fester Phase zu beschreiben. Wichtiges Merkmal dieses Porennetzwerkmodells ist die vollständige Erfassung von kondensierter Flüssigkeit durch die Einführung von neu formulierten Flüssigkeitsinvasionsregeln. Poren mit Volumen werden in das Netzwerk eingeführt, um die Überlappung benachbarter Hälse im klassischen Porennetzwerkmodell zu beheben. Bei der Trocknung des Netzwerkes wird der Flüssigkeitstransport durch Kapillarwirkung angetrieben, während der Dampftransport durch Konvektion erfolgt. Die Simulationsergebnisse, die als Temperatur- und Feuchtigkeitsprofile im Laufe der Zeit dargestellt werden, zeigen qualitative Übereinstimmung mit verfügbaren experimentellen Daten. Die Einbeziehung der neuen Invasionsregeln verbessert die Erfassung der kondensierten Wassermasse im Vergleich zu früheren Modellen, bei denen die Kondensation nur teilweise berücksichtigt wurde. Reibungsbehaftete Dampfströmung in diesen Simulationen ermöglicht es, die treibende Kraft des Dampftransports — den Dampfüberdruck innerhalb des Netzwerkes — wiedergegeben. Der Einfluss des Dampfüberdrucks auf den Zerfall der Flüssigphase in Cluster wird ebenfalls diskutiert.

Des Weiteren wird ein Kontinuumsmodell entwickelt, um die Wärme- und Stoffübertragung innerhalb eines einzigen hygroscopischen porösen Einzelpartikels mit undurchlässiger fester Phase zu beschreiben. Wichtige thermophysikalische Eigenschaften von Holzpartikeln, die als Beispiel hierfür dienen, werden als Eingabe des Kontinuumsmodells experimentell bestimmt. Das Kontinuumsmodell wird anhand von experimentellen Daten validiert, die mit einer Magnetschwebewaage experimentell gemessen wurden. Dann wird dieses komplexe Kontinuumsmodell in ein einfacheres Modell, die sogenannte charakteristische Trocknungskurve, reduziert. Dabei werden Korrelationen der Parameter des reduzierten Modells in Abhängigkeit von den Trocknungsbedingungen aus den numerischen Ergebnissen hergeleitet. Simulationsergebnisse, die sowohl vom komplexen als auch vom reduzierten Modell erhalten wurden, werden durch Vergleich mit den experimentellen Daten validiert. Der Einfluss der Trocknungsbedingungen auf den kritischen Feuchtegehalt wird auch ausführlich diskutiert.

Zum Schluss wird das vorgenannte kontinuierliche Modell erweitert, um die Dynamik der Wärme- und Stoffübertragung in einem zellularen porösen pflanzlichen Ursprungs zu beschreiben. Dieses Modell berücksichtigt die konjugierten Flüssigkeits- und Dampfströme im interzellulären Hohlraum sowie den diffusiven Flüssigkeitsfluss über die Zellmembran des porösen Mediums. Das Modell wird gegen Trocknungsexperimente validiert, die in der Magnetschwebewaage bei drei verschiedenen Temperaturen des überhitzten Dampfes für Kartoffelproben durchgeführt wurden. Ein Vergleich zwischen den Simulationen und den Experimenten zeigt, dass die Trocknungseigenschaften zufriedenstellend vorhergesagt werden können. Der Einfluss der Wasserleitfähigkeit der Zellmembran auf die räumlich-zeitliche Verteilung von Feuchte und Temperatur im porösen Medium wird durch numerische Simulationen analysiert. Es wird gezeigt, dass die Wasserdiffusion über die Zellmembran die Dynamik der Wärme- und Stoffübertragung im porösen Medium und damit die Trockenkinetik steuert.

Nomenclature

A	area, m^2
A_v	specific internal area per unit volume, $m^2 m^{-3}$
c_p	constant pressure specific heat capacity, $J kg^{-1} K^{-1}$
d	diameter, m
d_s	characteristic length, m
e	relative coarse layer thickness, -
f	drying rate retardation coefficient, -
f_v	area fraction of the vapor region, -
h	specific enthalpy, $J kg^{-1}$
Δh_{evp}	specific evaporation enthalpy, $J kg^{-1}$
j_w	water diffusion flux across cell membrane, $kg m^{-2} s^{-1}$
K	absolute permeability, m^2
K_r	relative permeability, -
L	length / thickness, m
L_p	water conductivity of cell membrane, $m^3 N^{-1} s^{-1}$
L_t	throat length, m
\dot{M}	mass flow rate, $kg s^{-1}$
\tilde{M}_v	molar mass of water vapor, $kg mol^{-1}$
\dot{m}	mass flux, $kg m^{-2} s^{-1}$
\dot{m}_v	volumetric evaporation rate, $kg m^{-3} s^{-1}$
\mathbf{n}	outward unit normal vector, -
p	pressure, Pa
\dot{Q}	heat flow rate, W
\dot{q}	heat flux, $W m^{-2}$
\tilde{R}	universal gas constant, $J K^{-1} mol^{-1}$
r	radius, m
r_0	mean radius, m
S	saturation, -
T	temperature, $^{\circ}C$
t	time, s
v	superficial velocity, $m s^{-1}$
v_0	interstitial velocity, $m s^{-1}$
W	network thickness, m

Greek symbols

α	heat transfer coefficient, $\text{W m}^{-2} \text{K}^{-1}$
δ_{evp}	evaporation coefficient, -
ε	volume fraction, -
θ	contact angle, -
λ	thermal conductivity, $\text{Wm}^{-1} \text{K}^{-1}$
μ	dynamic viscosity, Pa s
ν	kinematic viscosity, $\text{m}^2 \text{s}^{-1}$
ξ	used in the stopping criterion of the pore network algorithm, -
ρ	liquid mass density, kg m^{-3}
σ	surface tension, N m^{-1}
σ_0	radius standard deviation, m
σ_{rad}	Stefan-Boltzmann constant, $\text{W m}^{-2} \text{K}^{-4}$
ϕ	water potential, Pa
φ	relative humidity, -
ψ	porosity, -
<i>Subscripts/superscripts</i>	
c	capillary
ch	channel
$conv$	convection
cn	index of liquid cluster
cr	critical
cv	control volume
eff	effective
evp	evaporation
ext	extracellular
f	fluid
fin	fin
i, j, k, m, n	pore index
in	inlet
inc	incipient point
int	intracellular
$intr$	intruded
l	liquid
n	nomalized
out	outlet
p	pore
rad	radiation
ref	reference
s	solid
sat	saturation
st	index of single liquid throat
$surf$	surface
v	vapor

w	water
x, y, z	Cartesian coordinates
0	initial
<i>Abbreviations</i>	
CDC	characteristic drying curve
CFD	computational fluid dynamic
CFT	condensation fully treated
CPL	capillary pumped loop
CPT	condensation partly treated
CDR	constant drying rate
DEM	discrete element method
FDR	falling drying rate
HAD	hot air drying
LHP	loop heat pipe
REV	representative elementary volume
SSD	superheated steam drying

Acknowledgment	i
Abstract	ii
Kurzzusammenfassung	iv
Nomenclature	vi
Table of contents.....	ix
1 Introduction	1
1.1 Background	1
1.1.1 Porous media	1
1.1.2 Transport phenomena in porous media	2
1.2 Modeling of transport phenomena in porous media	3
1.2.1 Continuum-scale models	4
1.2.2 Pore-scale models.....	5
1.3 Motivation of this thesis	6
1.4 Outline of this thesis	8
2 Pore network simulations of heat and mass transfer inside capillary porous wick in dry-out operating regime	10
2.1 Literature review	10
2.2 Problem description	13
2.3 Pore network model	14
2.3.1 Mass transfer model	14
2.3.2 Heat transfer model	15
2.3.3 Heat and mass transfer at the liquid-vapor interface and at the boundaries.....	16
2.3.4 Working fluid	18
2.3.5 Numerical algorithm	19
2.4 Simulation results and discussion	21
2.4.1 Model verification	22
2.4.2 Temperature and pressure distributions	23

2.4.3 Influence of the heat load on the shape of the vapor pocket and on the heat transfer efficiency.....	25
2.4.4 Influence of the porous structure on the heat transfer efficiency.....	27
2.4.5 Influence of the liquid inlet pressure and of the liquid inlet temperature on heat transfer efficiency.....	33
2.5 Conclusion	36
3 Pore network simulations of the superheated steam drying process in porous media	37
3.1 Literature review.....	37
3.2 Pore network model.....	40
3.2.1 Surface condensation and evaporation model.....	41
3.2.2 Network drying model	43
3.3 Results and discussion	50
3.3.1 Qualitative model validation	50
3.3.2 Impact of liquid invasion events on the temperature and moisture content evolution.....	53
3.3.3 Impact of liquid invasion rules on condensed liquid treatment and phase distribution	55
4 Continuum-scale modeling of the superheated steam drying process in a single wood particle and its reduction to a lump model	61
4.1 Literature review.....	61
4.2 Continuum-scale model.....	64
4.2.1 Mass and energy conservation equations.....	65
4.2.2 Closure relations.....	66
4.2.3 Initial and boundary conditions.....	67
4.3 Characteristic drying curve model.....	68
4.3.1 Mass and energy conservation equations.....	68
4.3.2 Drying rate retardation coefficient and critical moisture content	69
4.4 Material properties and drying experiment.....	69
4.4.1 Particle size distribution.....	69
4.4.2 Sorption isotherm.....	70
4.4.3 Effective thermal conductivity.....	71
4.4.4 Specific heat capacity.....	72
4.4.5 Particle density and porosity	72
4.4.6 Pore size distribution and equilibrium capillary pressure curve	73
4.4.7 Experimental setup for drying of a single wood particle	75
4.5 Results and discussion	76

4.5.1 Continuum model assessment	76
4.5.2 Critical moisture content	80
4.5.3 Drying rate retardation coefficient	82
5 Continuum-scale modeling of superheated steam drying of cellular plant porous media.....	85
5.1 Literature review	85
5.2 Model description	87
5.2.1 Mass conservation for water in intercellular void space	88
5.2.2 Energy conservation equation	89
5.2.3 Constitutive relationships	90
5.2.4 Surface shrinkage	92
5.2.5 Initial and boundary conditions	93
5.3 Material and experimental setup	95
5.4 Results and discussion	98
5.4.1 Model validation	98
5.4.2 Impact of cell membrane water conductivity on drying behavior	99
5.4.3 Impact of sample thickness on drying behavior.....	103
6 Conclusions and outlook	108
6.1 Conclusions.....	108
6.2 Future research work	111
References.....	113
Appendix	123
A Thermal properties of water	123
B Influence of convergence parameter on the vapor pocket pattern and on the computation time	124
C Contribution of convective heat transfer and viscous dissipation on energy conservation	125
D Experimental data obtained from single wood particle drying	127
E Experimental data obtained from potato sample drying	131
Publications and student works	140
Curriculum Vitae.....	143

Chapter 1

Introduction

1.1 Background

1.1.1 Porous media

In both natural systems (clays, aquifers, oil and gas reservoirs, plants and biological tissues, etc.) and industrial application (fuel cells, concrete, textiles, polymer composites, capillary heat pipe and paper, etc.), porous media are encountered. Morphologically, a porous medium is composed of a solid skeleton and an interconnected void space. The morphology of a porous system can vary from a simple structure such as bed packed with particles to extremely complex one such as porous catalysts. The traditional concepts, models and algorithms for porous media were developed in the geosciences, but they are based on several strong simplifications and are not directly applicable in most of industrial processes. The first primary reason is that the industrial porous media are more complicated than soils and reservoirs. For example, the geological porous media are usually hydrophilic, however, industrial porous materials can be completely hydrophobic or the wettability may change in time and/or space. Additionally, complex porous materials appear with various pore structures (granular, fibrous, foamy, layered, fractured etc.) at different length scales (nano-, micro-, and macroscales) and with a wide range of porosity values (1 to 90%). The second primary reason is that the fluid flow in an industrial porous medium may occur in completely different regime compared to a natural porous medium. Since the flow in the soils and rocks is slow, the constitutive relations such as capillary pressure curve are obtained under equilibrium conditions. However, in many industrial processes, the flows are very fast and far from equilibrium. Additionally, chemical reactions with high rate (e.g. in fuel cells, food processing) or fast deformation in

biological porous media may strongly affect the fluid flow. As a result, there is a very strong need for both tailored models and measurement techniques to study the mechanism of fluid flow in porous materials and their characteristics.

1.1.2 Transport phenomena in porous media

As common as porous media, phenomena of transport in porous media are encountered in a number of scientific and engineering disciplines [1]. The applications of transport in porous media can vary from the oil reservoirs [3], groundwater flows [4], compact heat exchangers [5,6] to trickle bed reactions [7], to name only a few. Several reviews on these applications of porous media are available in literature [8–11].

EXCHANGE PROCESSES

Heat

- Convection
- Radiation (infrared & solar)
- Phase change (latent heat of evaporation)
- Conduction (in contact with solid)

Liquid water

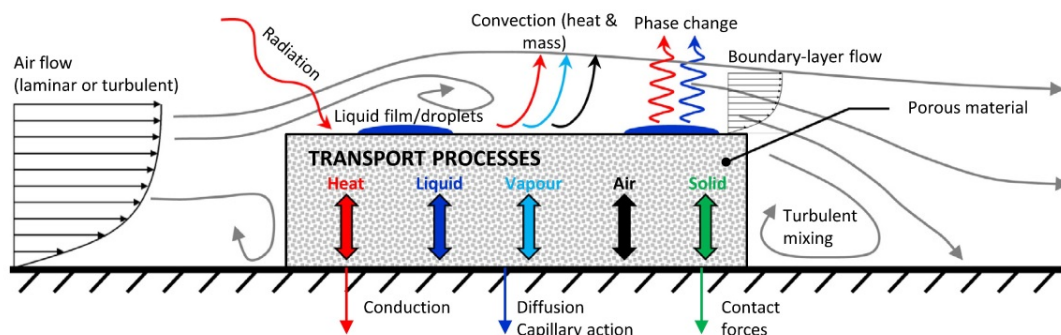
- Phase change (evaporation)
- Diffusion (e.g. osmotic dehydration)
- Capillary action

Water vapour & Air

- Convection

Solid

- Contact forces



TRANSPORT PROCESSES

Transported variable	Heat	Mass Liquid	Mass Water vapour	Mass Air	Mass Solid
Transport mechanisms	<ul style="list-style-type: none"> • Diffusion (Fourier, mass diffusion, Dufour effect) • Advection (mass convection) 	<ul style="list-style-type: none"> • Diffusion (capillary, osmosis, surface diffusion, thermally driven) • Convection (Darcy) 	<ul style="list-style-type: none"> • Diffusion (Fick, Knudsen diffusion, Soret effect) • Convection (Darcy) 	<ul style="list-style-type: none"> • Diffusion (Fick, Knudsen diffusion, Soret effect) • Convection (Darcy) 	<ul style="list-style-type: none"> • Mechanical deformation^a
Volumetric sources/sinks	<ul style="list-style-type: none"> • Phase change (latent heat of evaporation & heat of desorption) • Electromagnetic radiation (e.g. microwave) • Chemical binding/release energy (e.g. water in gypsum) 	<ul style="list-style-type: none"> • Phase change (evaporation & desorption) • Chemical binding/release of water • Gravity 	<ul style="list-style-type: none"> • Phase change (evaporation & desorption) 	<ul style="list-style-type: none"> • None 	<ul style="list-style-type: none"> • Gravity
Driving forces	<ul style="list-style-type: none"> • Temperature • Concentration (of gas) 	<ul style="list-style-type: none"> • Capillary pressure (surface tension) • Gas/liquid pressure^b • Concentration (of solutes) • Temperature 	<ul style="list-style-type: none"> • Gas pressure • Concentration (of vapour) • Temperature 	<ul style="list-style-type: none"> • Gas pressure • Concentration (of dry air) • Temperature 	<ul style="list-style-type: none"> • Water content • Temperature

Figure 1.1: Conceptual representation of transport phenomena in porous medium during the convective drying process (reprinted from [12]).

In consideration of any transport phenomena that involve a porous medium, the complex morphology of the medium and its influences on the distribution, flow, displacement of fluids are encountered. Furthermore, in multiphase fluid flow or multicomponent fluid flow, an interaction or reaction between these phases or these components may occur. For an example, the convective drying process of porous medium shown in Fig. 1.1 can

comprise by many different mechanisms, such as heat and mass transfer mechanisms, thermodynamic phase change, momentum transport mechanisms under various forces such as viscous, buoyance and capillary forces. Another example is the crystallization of solute during the flow. Besides the heat and mass transfer mechanisms, thermodynamic phase change and the appearance of crystals lead to a variation of hydraulic conductance of fluid flow. To investigate the complicated transport phenomena in porous media, several approaches were developed based on different theoretical standing points. In the next section of this chapter, a brief overview of approaches used to model the transport processes is presented.

1.2 Modeling of transport phenomena in porous media

The transport phenomena in porous medium may be considered at different scales (c.f. Fig. 1.2 for an example, i.e. the drying process presented from plant scale to nanoscale). At different scales, the approaches used to describe the transport processes may be quite different.

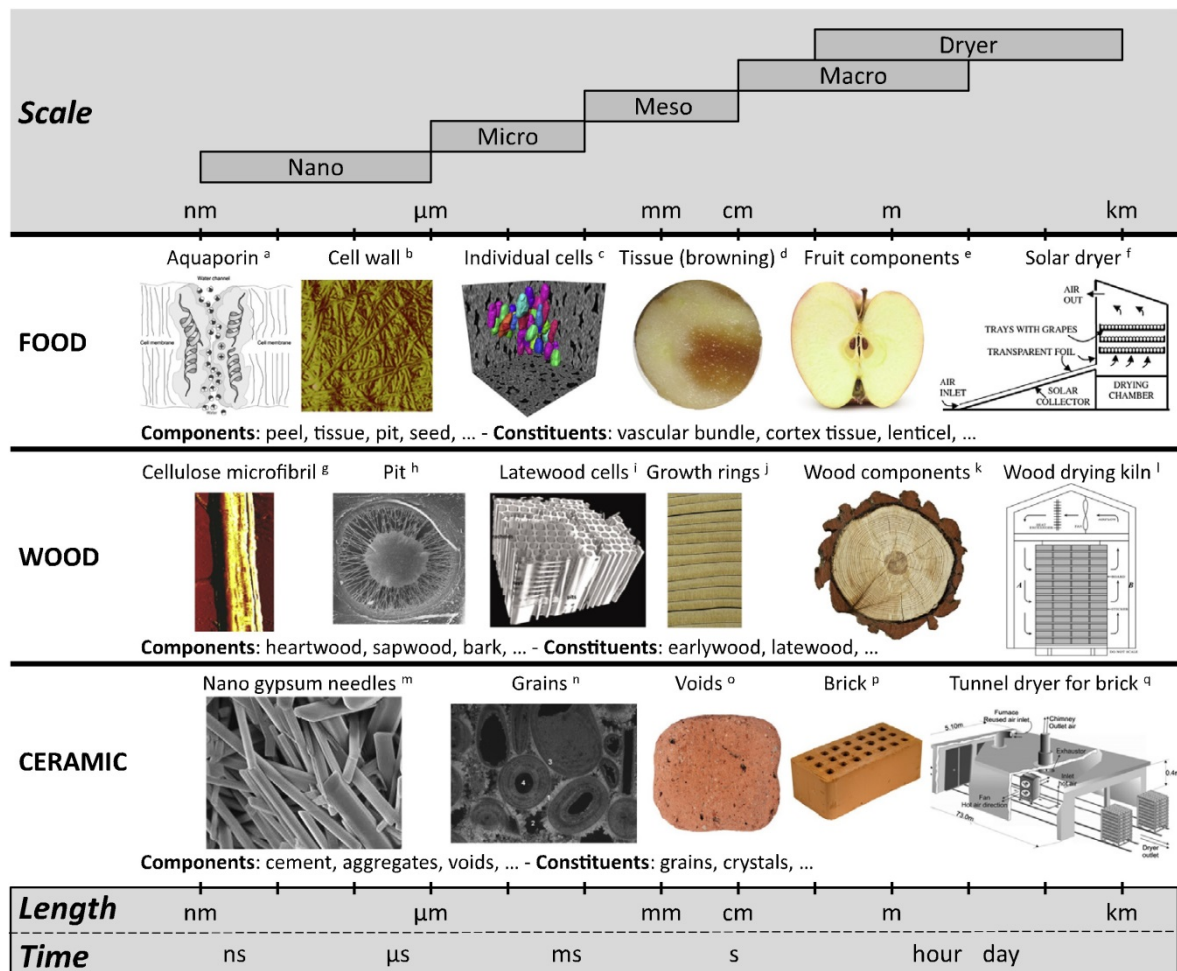


Figure 1.2: Multiple scales to be considered in porous medium drying processes (reprinted from [12]).

For instance, at the plant scale, lumped approaches are usually used to present, the transport processes in the porous product and the transport within the porous medium is simplified as much as possible to reduce the computational demand. At macro scale, mathematical continuous models are developed based on homogenous and isotropic assumptions. Since the fluid transport in a porous sample is often structure dependent and thus anisotropic, the underlying idea is that the properties of fluid and solid phases such as velocity, density, pressure are averaged in a Representative Elementary Volume (REV). The REV often refers to a sample size providing statistical robustness to an averaging procedure (c.f. Fig. 1.3). Thus, in a domain larger than the REV, the impact of medium micro-heterogeneity on the transport properties is assumed to be negligible. Coming to a smaller scale, micro or nanoscale, the transport processes are considered at the pore level and the heterogeneity plays a role in the transport behavior. At this pore-scale, the homogeneous assumption is not valid since the domain may be much smaller than the REV. As an alternative method, pore-scale approaches which consider the transport processes in individual pores are then used. In this section, an overview of continuous and pore-scale approaches which are practically used for modeling the transport processes in porous media from the micro- to the macro-scale is presented.

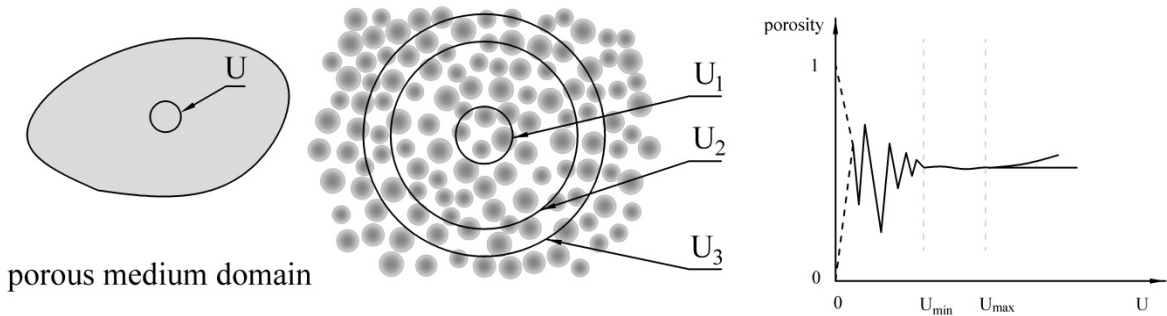


Figure 1.3: The variation of porosity on different domain sizes and the size of Representative Elementary Volume (REV) from U_{\min} to U_{\max} (adapted from [13]).

1.2.1 Continuum-scale models

Generally, the continuum-scale models are developed based on macroscopic mass and heat transfer laws such as Darcy law, Fick law, Stefan law, Fourier law [13,14]. The heat and mass conservation equations are expressed in terms of microscale variables. However, the variables of the problem at the microscale are obtained by averaging in the control volume. The size of control volume considered in continuum-scale models is often quite large compared to the size of REV. The transport processes at pore-scale are considered via several effective parameters which take into account the average structural properties such as pore size, pore shape and porosity. Therefore, the major assumption used to develop this kind of model is that of an isotropic and homogeneous medium. The most rigorous continuum-scale models are obtained based on the volume averaging technique in which

variables defined at the microscale are averaged over a volume of interest to obtain macroscale average values.

The equations of continuous models are inherently coupled to each other. By applying numerical methods such as finite element, finite volume or finite difference methods, the continuum-scale model equations can be solved. Since the effective parameters used in the model are experimentally fitted, the obtained results of continuum-scale models are often a good representation of experimental observations. Naturally, the use of a finer mesh in numerical methods leads to higher accuracy solutions. Nevertheless, when the number of mesh elements is larger than a critical value, which is often not too large, further improvement of the solution by still finer mesh becomes negligible. The critical size of the mesh is often around some hundreds of nodes. Therefore, the computational cost of continuum-scale models is not expensive compared to discrete pore-scale models presented in Sec. 1.2.2.

Despite of these aforementioned strengths and the wide application of continuum-scale models, the needed effective parameters of the models must be estimated from a series of experiments which are usually time consuming and expensive. It should be noted that the measurement can be challenging, especially for multiphase flow conditions. Additionally, the continuum-scale approaches sometimes are not appropriate to be applied particularly for thin porous materials such as fibrous media or membranes where the size of the medium is smaller than the size of REV [15].

1.2.2 Pore-scale models

The first, by now classical paper on pore-network modeling was probably published by Fatt [16] in the mid-1950s, and the author probably had not thought that his proposed approach would become one of the major approaches in porous media research. Fatt recognized that the void space in most porous media can be represented by a network of voids space complementary to the solid skeleton and the transport processes can be described by a discrete system of equations written for the pore nodes of the network, the so-called pore network approach. Afterwards, other pore-scale approaches, such as the direct numerical approach, the volume of fluid approach, and the density functional method have also been developed. These discrete pore-scale approaches enable the investigation of the heat and mass transfer by solving the transport equations directly at the pore-scale. Fluid flow in a heterogeneous porous material can be better understood in this way. Furthermore, a better macroscopic understanding of the transport processes in porous media can be provided by computing macroscopic transport coefficients such as the relative permeabilities of multiphase flow, or the dynamic capillary pressure – as functions of the saturation – from pore-scale simulation results. Due to these merits, pore-scale approaches have been widely used for modeling and simulation in the context of various

applications such as liquid imbibition [17], oil recovery [18], water management in the porous layer of fuel cells [19,20], and fluid transport in the porous wick of a loop heat pipe [21].

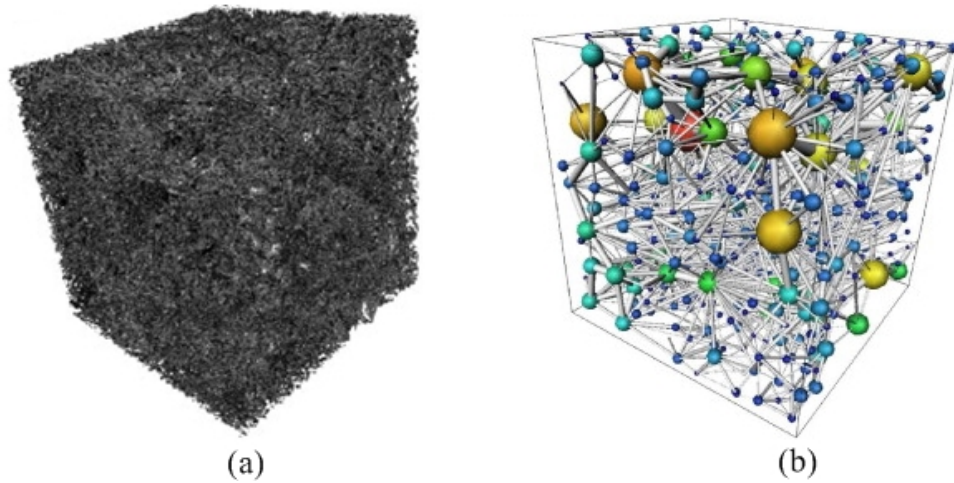


Figure 1.4: Pore-space image (a) and pore network (b) extracted from this image (reprinted from [22]).

The disadvantage of pore-scale models is their high computational cost due to a large system of equations which stems from the number of pore nodes; see Fig. 1.4 for an example. The computational domain size that can be used for the simulation of a real medium is a compromise between the available computational resources (CPU and RAM) and the REV size of the problem one would like to study, or the mechanism to reproduce.

1.3 Motivation of this thesis

As discussed in Sec. 1.2.2, pore network models are powerful tools to fundamentally investigate the transport processes, whereas continuum models are very helpful in predicting the macroscopic transport behavior. In this thesis, both continuum and pore-network models are developed to study the non-isothermal vapor-liquid transport taking place in a porous medium. In the processes considered, the evaporation of pure liquid occurs in a porous medium and the heat and mass transfer are therefore strongly coupled. Main characteristics of two-phase flow are: (1) the transport of gas phase (pure vapor) is driven by the advective mechanism, (2) the liquid is transported under capillary action and (3) phase transition intensively occurs under the thermal effect. Such kind of vapor-liquid flow may be encountered in both industrial devices (i.e. porous burner, loop heat pipe, transpiration cooling device) and industrial processes (i.e. superheated steam drying, vacuum contact drying). Related transport phenomena may be either time-independent or time dependent. Furthermore, the porous medium involved in respective processes may be constructed by an impermeable solid skeleton or be structured by permeable elements of

the solid phase. A coarse overview of multiscale approaches previously developed to simulate such processes is presented in Fig. 1.5. Non-isothermal transport processes in a porous medium constructed by impermeable solid skeleton have rather exhaustively been investigated by continuous models, so that several reviews on this research area can be found in literature [6,23,24]. Therefore, this thesis firstly aims to investigate the thermal and hydrodynamic characteristics of steady-state vapor-liquid flow involved in a capillary porous medium by pore network modeling only. Then, attempts are undertaken to investigate several transient processes by both pore network and continuum models. From the practical point of view, the thesis is particularly focused on the steady-state evaporation process in a capillary porous wick and the superheated steam drying (SSD) process.

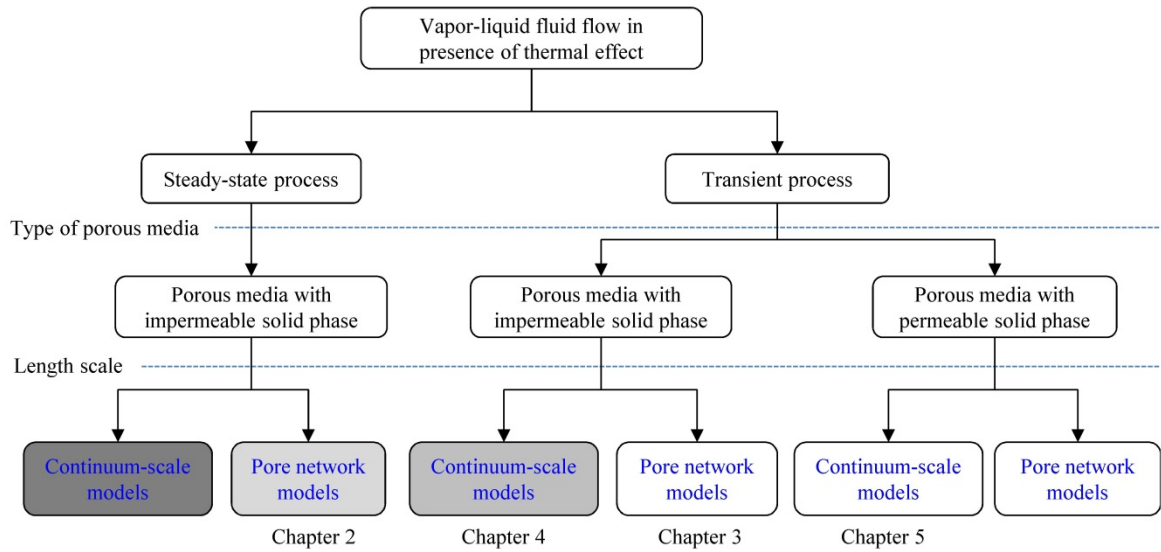


Figure 1.5: Motivation and structure of this thesis. The color of the boxes in the last row indicates the exhaustiveness of models available in the literature. The color gradient from dark to light visualizes the most to the least exhaustive investigation.

Evaporation in a capillary porous wick is widely applied to fabricate passive micro and miniature energy systems such as loop heat pipe or capillary pumped loop. Continuum-scale models of heat and mass transfer in the porous evaporator have been developed intensively, so that several reviews on this topic can be found [6,24]. However, the influence of wick structure on the operating behavior was not investigated via these continuum-scale models. Recently, pore-network models have also been developed by Prat and his co-authors [21,25–28] to study the transport phenomena within the evaporator. By using pore network models, several parametric studies were performed to investigate the influence of pore size disorder and thermal properties on the effective conductance of the evaporator. However, no exhaustive research work currently exists on the heat and mass transfer processes inside a capillary porous wick with opposite replenishment or on the effect of operation and structural parameters on heat transfer efficiency. Therefore, a pore network model was developed in this work to perform a parametric study of the heat and

mass transfer in the porous wick in dry-out operating regime at steady state. The model aims to pave the way to improve and to optimize the structure of wicks for lower pressure drop and higher thermal efficiency of the evaporators.

The thesis also aims to provide better macro and micro scale understanding of the superheated steam drying process of capillary porous media. During the past decade, superheated steam drying has gained importance because of its environmental advantages, and its immense potential for saving energy and for improving product quality. While being more than 100 years old and common in numerous industrial applications [29], the SSD of porous materials is still poorly understood from a theoretical standpoint. A better fundamental understanding of this drying process at both pore-scale and continuum-scale may help to design better products and processes. Firstly, a pore network model and a continuum-scale model are developed to simulate the drying process of rigid porous medium constructed by impermeable solid phase. Parametric studies are performed on both models to investigate the influence of drying conditions and structural parameters on drying behavior. Secondly, a continuum-scale model is developed to describe the heat and mass transfer during superheated steam drying of wood particles. Then, the comprehensive continuum-scale model is reduced into a simpler model, the characteristic drying curve model, which is more suitable to be incorporated in CFD-DEM solvers due to low computational cost. Furthermore, the continuum model is extended to simulate the drying process of cellular plant material where the moisture is mostly accumulated within the cells. By introducing water diffusion across the permeable cell membrane, the model takes into account both fluid flow in the intercellular void space and fluid flow across the membrane from the cell space to the intercellular void space. Whenever possible, the thesis also attempts to validate the numerical results by comparison to experimental observations.

1.4 Outline of this thesis

The main content of this thesis is organized as follows (c.f. Fig. 1.5):

In Chapter 2, the pore network approach is applied to simulate the evaporation process within a capillary porous wick in dry-out regime. The pore network model is introduced after a detailed literature review of this research area. Model validity is checked by comparing with experimental data. After that, the influence of pore structure on the operating behavior is investigated.

In Chapters 3, a pore network model is developed to simulate heat and mass transfer in a porous medium during the superheated steam drying process. First, literature is reviewed and the motivation of this work is explained. After that, the pore network drying model is presented in detail. In this model, newly formulated liquid invasion rules are introduced to fully treat condensation in pores within the material. The model is validated by comparing

against the experimental observations. The influence of the liquid invasion rules on the drying behavior is explored.

Chapter 4 presents the development of a continuum model for heat and mass transfer within a wood particle subjected to superheated steam drying and the reduction procedure to determine the parameters of a characteristic drying curve model. Both the continuum model and the characteristic drying curve model are validated against experimental data obtained from a magnetic suspension balance drying system. In Chapter 5, this continuum-scale model is extended to take into account the intracellular moisture and its diffusion across cell membranes. The numerical results obtained from the extended continuum-scale model are successfully validated by comparing with experimental data. The influence of the water conductance of the cell membrane on the evolution of moisture content and temperature is discussed in detail.

The main contents of this thesis together with the major conclusions are summarized in Chapter 6, where suggestions for future work are also made.

Chapter 2

Pore network simulations of heat and mass transfer inside capillary porous wick in dry-out operating regime

This chapter is an extended version of the paper *Pore network simulations of heat and mass transfer inside capillary porous wick in dry-out operating regime* published in *Transport in Porous Media* (2016), DOI: 10.1007/s11242-016-0737-4.

2.1 Literature review

Non-isothermal fluid flow with phase transition in porous media occurs in numerous heat exchange devices. The advantage of using porous material in the fabrication of these devices is its very large specific area, which enhances the heat and mass transfer process at the pore-scale. The phase transition phenomena such as evaporation or condensation yield a very high value of the heat transfer coefficient, allowing devices to be more compact. Furthermore, the liquid phase can be transported through the porous medium by wicking, which is driven by the capillary suction taking place at the three-phase contact line. Therefore, the porous medium works like a capillary pump and thus moving parts are not needed in the equipment. Two major applications utilizing these benefits of two-phase flow porous wicks are the Loop Heat Pipe (LHP) and the Capillary Pumped Loop (CPL). The model considered here is inspired by a typical situation in LHP and CPL evaporators; however, this model is not limited to this context. Therefore, this chapter will not use the LHP terminology except in Section 2.4, where the pattern of the vapor pocket in an LHP is discussed.

A porous layer in which the liquid and the thermal energy are replenished at opposite sides is considered in this study. This configuration appears in several applications, not only in

LHP evaporators [6] but also in porous burners [30], for example. As shown in the two-dimensional cross-section image (Fig. 2.1), the liquid is supplied from the bottom and it invades the porous wick due to capillary action. The heat load is applied at the top surface via a metallic fin, which is in contact with the porous structure. For high heat load the liquid evaporates inside the wick, and the vapor flows towards the open segments of the top surface. The heat and mass transfer processes are thus strongly coupled in this device. Many parameters and properties may influence the heat and mass transfer inside the capillary porous wick, such as, the solid phase material, thickness, porosity, and permeability of the porous wick, the working fluid, and the heat load as well as other operating conditions. Parametric studies shall allow us to select some of these parameters for evaluation and to analyze the behavior of the system under parameter variations.

Conventionally, as assumed in the literature [24,25], the system can be in one of two different regimes: In the low heat load regime, the porous wick is fully wetted and the evaporation occurs only at the wick surface. In the high heat load regime, however, the porous wick is only partially saturated and evaporation occurs also inside the wick. Cao and Faghri [31] developed a two-dimensional analytical model for the heat and mass transfer in a fully wetted porous wick. In their model, the liquid and vapor flows are coupled via the mass balance equation at the porous wick surface. The liquid flow in the porous wick and the vapor transport between the fins are determined from numerical simulations using the finite element method. In a later study of the same authors [32], an approximate analytical solution of the model equations is given for flat segments of the porous wick. Li and Peterson [33] developed three-dimensional models for a square flat wick, which has a liquid reservoir at the top and a heating substrate at the bottom. Chernysheva and Maydanik [34] as well as Zhang et al. [35] presented 3D models for capillary porous wicks with longitudinal replenishment. In these studies, the liquid flow is assumed to be perpendicular to the heat flux at the wick wall, whereas in the work of Li and Peterson [33] the fluid and energy flows are counter current. The model in Chernysheva and Maydanik [34] accounts for the dependence of the thermal properties on the temperature (but not on the pressure), whereas the other models mentioned so far assume constant thermal properties. Since these models are restricted to fully wet homogeneous and isotropic porous wicks, they are valid only in the low heat load regime.

For high heat load (the so-called dry-out regime), several heat and mass transfer models for the unsaturated porous wick were developed. Zhao and Liao [36] presented a 1D analytical model to determine the heat and mass transfer in the porous layer wick. They assumed that the working fluid is a mixture of liquid and vapor in the two-phase zone, and therefore, the capillary effect and the liquid-vapor interface are not considered in their model. A 2D model based on Darcy's law showing the vapor zone inside a flat wick was presented by Demidov and Yatsenko [37]. This mathematical model used the moving evaporation front

method of Figus et al. [25]. The Demidov and Yatsenko model was also used by Kaya and Goldak [38] to investigate the heat and mass transfer in a cylindrical wick. In these models, the incipient boiling superheat value, the operating point at which the fully saturated wick changes to a partially wet wick, is assumed to be constant, whereas in Kaya and Goldak [38] the incipient boiling superheat value was defined and discussed based on bubble nucleation in liquids. A time-dependent 2D continuum-scale model for an unsaturated wick was presented by Boubaker et al. [39]. In that study, the evaporation rate is described by the Langmuir law instead of using energy balance equations as in the rest of studies that treat the dry-out regime of porous wick. Ren [40] developed an axisymmetric 2D model to determine the shape and position of the vapor zone for different values of the heat load in a cylindrical porous wick. In their studies, the capillary forces are taken into account, but the pressure jump across the liquid-vapor interface induced by the capillary pressure thresholds is not present in the pressure profiles [25,40,41]. The previous work cited up to here considers homogeneous and isotropic porous wicks in which the liquid-vapor interface is smooth as the capillarity at the liquid-vapor interface is uniform. Therefore, these models cannot explain the evolution of a non-smooth liquid-vapor interface, which was observed, however, in experimental studies by Zhao and Liao [36,42,43], and by Byon and Kim [44]. In addition to continuum approaches, discrete pore network models provide another way to investigate flow and transport in porous media. Prat and his co-workers [21,25,26] used this approach to simulate the heat and mass transfer in 2D and in 3D capillary wicks at steady state. They also investigated the transient behavior of the capillary porous wick by a 2D pore network simulation [45].

Very recently, Mottet et al. [27] and Nishikawara et al. [28] presented 3D pore network models for different fluid configurations. In the work of Mottet et al. [27] the thermally conductive fin is made of a solid metallic blade, whereas in Nishikawara et al. [28] an etched porous fin is considered. The 3D simulation results [27] indicate that between the saturated wick and the dry-out regime there is another operating regime, the so-called two-phase zone regime, in which the liquid and the vapor phase coexist below the fin. In this two-phase zone regime, the bottom surface of the fin is partially wetted; therefore, the effective heat transfer coefficient stabilizes at a high value before decreasing significantly during the dry-out regime. This interesting finding obtained by numerical simulations still needs to be confirmed experimentally. The appearance of the two-phase zone regime leads to a qualitative analogy between the calculated and experimentally observed thermal conductances [27]. Due to the assumption of a macroscopically sharp evaporation front in the continuum approach this regime was overlooked in some previous studies based on both 2D pore network and 2D/3D continuum simulations [27]. In these studies the vapor pocket pattern is visualized only for pore networks with a unimodal pore size distribution and for constant thermal properties of the liquid and vapor phases.

No exhaustive research work currently exists on the heat and mass transfer processes inside a capillary porous wick with opposite replenishment or on the effects of operation and structural parameters on the heat transfer efficiency. A parametric study of the heat and mass transfer in the porous wick is introduced in this thesis. Although a 2D pore network model cannot represent the two-phase zone regime of a porous wick [27], it still has the ability to predict the operating behavior in the dry-out regime for various porous structures. The energy and fluid transports are investigated by pore network models with discrete as well as continuous unimodal and bi-modal pore size distributions. Bi-layer porous wicks are also investigated.

2.2 Problem description

A capillary wick with partial heating from the top surface is depicted in Fig. 2.1 (left). The liquid is supplied from the bottom of the wick, whereas the heat load is imposed near the top center of the wick. At the lateral edges of the wick symmetry boundary conditions are imposed. As discussed in the literature [24,27], for very high heat load, the capillary porous wick is in the dry-out regime. The incipient boiling superheat value is eventually reached as the heat load increases, and a vapor zone, the so-called vapor pocket, forms inside the wick. Liquid is continuously pumped from the bottom to the liquid-vapor interface by capillary action. Evaporation occurs at the liquid-vapor interface (both in the interior and at the surface of the porous wick), and the vapor flows towards the vapor outlet. A pore-scale representation of the unsaturated wick and of the processes involved is sketched in Fig. 2.1 (right). In this work, only steady-state operation is considered.

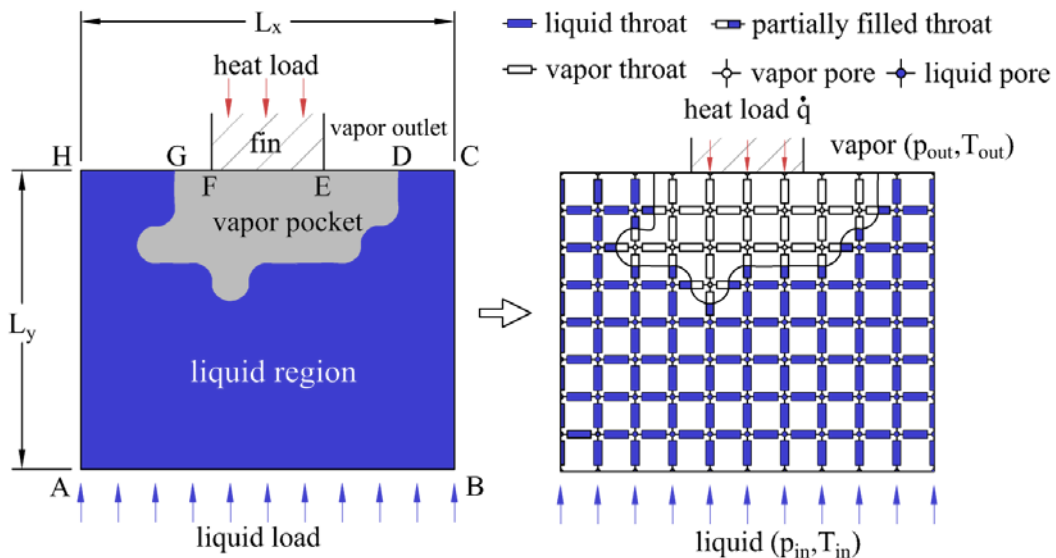


Figure 2.1: Schematic 2D drawing of the heat and mass transfer processes in a porous wick (left), and their representation in a pore network model (right).

2.3 Pore network model

A porous wick is composed of a solid matrix and an interconnected network of closed and open pores (i.e. transport pores) filled with fluid (liquid or gas). The heat and mass transfer is considered to take place only in the open pores. As in several previous studies [25,45,46], a 2D Cartesian network of pores (which have no volume) and cylindrical throats is employed to represent the microstructure of the porous wick (see Fig. 2.1). Each interior pore in the network is connected to four throats. The following assumptions were made in the development of our pore network model: The solid material is non-hygroscopic and saturated initially with a working fluid. Liquid films in the throats are neglected. The solid and fluid phases are in local thermal equilibrium. The liquid and vapor flows through the throats are laminar and the viscous dissipation is negligible (c.f. Appendices B and C). Gravitational effects are assumed to be small compared to capillary effects, and thus neglected. Heat transfer is by conduction only. Despite these simplifications, the model is still capable of capturing striking features involved during the steady-state operation of an unsaturated capillary porous wick and provides insights into various macroscopic phenomena resulting from pore-scale processes. In the following, the pore network model is described in detail.

2.3.1 Mass transfer model

In this work, we assume that there is not any non-condensable gas inside the wick. Hence, the Hagen-Poiseuille law is applied to compute the mass flow rate for both the liquid and the vapor phases:

$$\dot{M}_{ij} = \frac{\pi r_{t,ij}^4}{8\nu_f L_{t,ij}} (p_i - p_j), \quad (2.1)$$

where \dot{M}_{ij} denotes the flow rate through the throat connecting the pores i and j , ν_f denotes the fluid (liquid/vapor) kinematic viscosity, p_i and p_j denote the liquid/vapor pressure at pores i and j , respectively. $L_{t,ij}$ and $r_{t,ij}$ denote the throat length and radius, respectively.

To satisfy the mass conservation, the total mass flow at a pore i which is located either inside the liquid region or inside the vapor pocket (see Figs. 2.2a-b) must be equal to zero:

$$\sum_j \dot{M}_{ij} = 0. \quad (2.2)$$

If, however, the pore i connects to at least one partially liquid-filled throat (Figs. 2.2c-d), the mass conservation equation is instead given by

$$\sum_j \dot{M}_{ij} \pm \sum_k \dot{M}_{evp,ik} = 0, \quad (2.3)$$

where the “+” sign is used in the case of a liquid pore and the “-” sign is used in the case of a vapor pore. In Eqs. 2.2 and 2.3, the sums run over all neighboring pores of pore i ; j are the indices of neighboring pores containing the same phase as pore i , and k are the indices of neighboring pores containing a different phase than pore i . The evaporation flow rates, $\dot{M}_{evp,ik}$, are calculated by Eqs. 2.17 and 2.19. The resulting sparse system of linear equations (Eqs. 2.2, 2.3) is solved numerically to obtain the liquid and vapor pressure fields in the pore network.

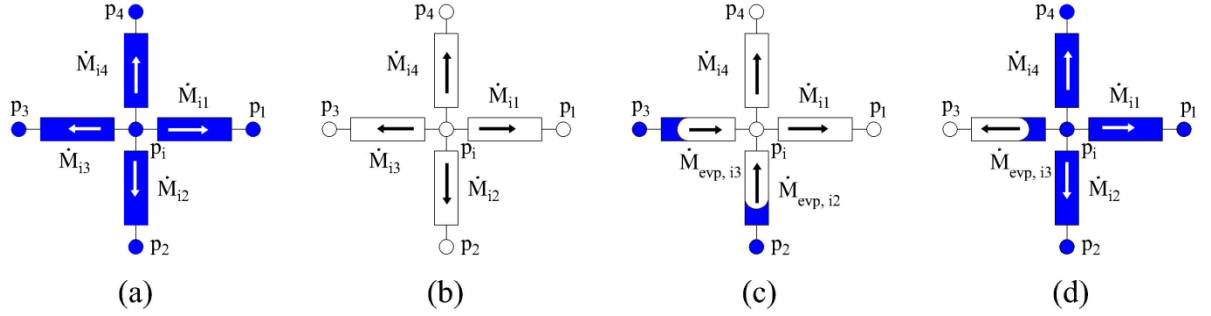


Figure 2.2: Illustration of the mass balance for: (a) a liquid pore and (b) a vapor pore with empty neighboring throats, (c) vapor and (d) liquid pores with partially filled neighboring throats. p denotes the pressure at the pores. Arrows indicate the flow directions of liquid or vapor.

2.3.2 Heat transfer model

Based on the local thermal equilibrium assumption, the temperatures of the solid and fluid phases must be equal. The heat transfer occurs only due to conduction in each phase. The latent heat of evaporation at the liquid-vapor interface is taken into account in this model. The heat conduction in the vapor pocket or in the saturated wick is described by a discrete version of Fourier’s law:

$$\dot{Q}_{ij} = A_{cv,ij} \lambda_{eff,ij} \frac{T_i - T_j}{L_{t,ij}}, \quad (2.4)$$

where $A_{cv,ij}$ denotes the heat transfer area and where $\lambda_{eff,ij}$ denotes the effective thermal conductivity between the pores i and j .

In a 2D Cartesian pore network, the heat transfer area is calculated as $A_{cv,ij} = WL_t$ (see Fig. 2.3). Several models for the effective thermal conductivity λ_{eff} can be found in the literature. It is usually a function of the solid phase conductivity, λ_s , the working fluid conductivity (vapor/liquid), λ_f , and the ratio between the solid and void areas of connected throats. For the pore network model considered here, the effective thermal conductivity is determined by the parallel heat flux model [47]:

$$A_{cv,ij} \lambda_{eff,ij} = (A_{cv,ij} - \pi r_{t,ij}^2) \lambda_s + \pi r_{t,ij}^2 \lambda_f. \quad (2.5)$$

For a pore i in the vapor pocket or in the liquid cluster, the energy balance equation is given by

$$\sum_j \dot{Q}_{ij} = \sum_j A_{cv,ij} \lambda_{eff,ij} \frac{T_i - T_j}{L_{t,ij}} = 0, \quad (2.6)$$

where j runs over all pores connected to pore i .

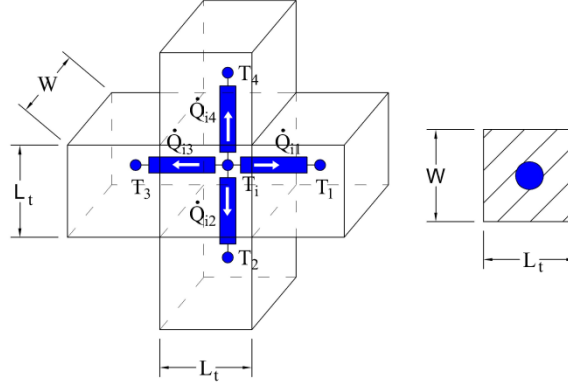


Figure 2.3: Energy balance at a liquid pore i . Arrows inside the throats indicate the heat flow directions.

2.3.3 Heat and mass transfer at the liquid-vapor interface and at the boundaries

At the liquid-vapor interface, the evaporation is driven by heat transfer. The boundary conditions at the evaporation front in this work are as follows

$$p_v - p_l = p_c, \quad (2.7)$$

$$T_v = T_l = T_{sat}(p_v), \quad (2.8)$$

$$\lambda_{eff,v} \nabla T_v \cdot \mathbf{n} - \lambda_{eff,l} \nabla T_l \cdot \mathbf{n} = \Delta h_{evp} \rho_l v_l \cdot \mathbf{n}. \quad (2.9)$$

In Eq. 2.7, p_v and p_l denote the vapor and liquid pressure, respectively, and $p_c = \frac{2\sigma \cos \theta}{r}$ denotes the capillary pressure. In Eq. 2.8, T_v and T_l denote the vapor and liquid temperature, respectively; T_{sat} denotes the saturation temperature. In Eq. 2.9, $\lambda_{eff,v}$ and $\lambda_{eff,l}$ denote the effective thermal conductivities of vapor and liquid filled regions, respectively; \mathbf{n} denotes the outward unit normal vector pointing out of the liquid phase; ρ_l and v_l denote the liquid mass density and velocity, respectively; Δh_{evp} denotes the latent

heat of evaporation. The other boundary conditions are listed as follows (refer to Fig. 2.1 (left) for edge labels):

At the bottom of the wick (edge AB)

$$T = T_{in}, \quad p = p_{in}, \quad (2.10)$$

where T_{in} and p_{in} denote the prescribed inlet liquid temperature and pressure, respectively.

At the symmetric boundary (edges AH and BC)

$$\frac{\partial T}{\partial x} = 0, \quad \frac{\partial p}{\partial x} = 0. \quad (2.11)$$

At the wick-fin interface (edge EF)

$$\lambda_{eff,v} \frac{\partial T}{\partial y} = \dot{q}, \quad \frac{\partial p}{\partial y} = 0. \quad (2.12)$$

At the dry part of the vapor outlet (edges DE and FG)

$$T = T_{out}, \quad p = p_{out}, \quad (2.13)$$

where T_{out} and p_{out} denote the prescribed vapor temperature and pressure at the vapor outlet, respectively. At the wet part of the vapor outlet (edges CD and GH)

$$T = T_{out}, \quad -\lambda_{eff,l} \nabla T_l \cdot \mathbf{n} = \Delta h_{evp} \rho_l v_l \cdot \mathbf{n}. \quad (2.14)$$

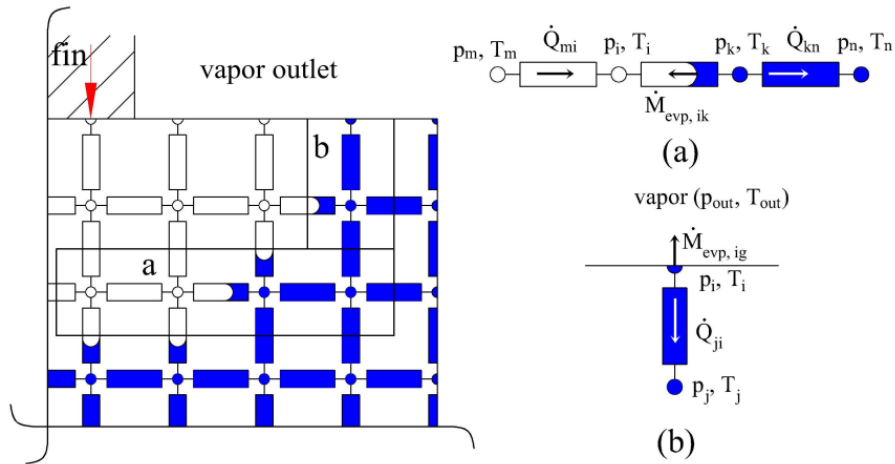


Figure 2.4: Illustration of heat and mass transfer processes at the liquid-vapor interface (a) inside the porous wick and (b) at the wick surface. Arrows indicate either mass or energy flow directions. The liquid and vapor phases are shown in blue and white, respectively.

These boundary conditions can be imposed directly in the pore network model, except the heat and mass transfer equations at the liquid-vapor interface (Eqs. 2.7 to 2.9 and Eq. 2.14). The evaporation rates $\dot{m}_{evp} = \rho_l v_l \cdot \mathbf{n}$ required at this interface are computed from energy balance equations (Eqs. 2.17 and 2.19). Examples of a vapor pore and of a liquid

pore at the liquid-vapor interface inside the wick, as well as of a liquid pore at the wet wick surface, are shown in Fig. 2.4. The interface conditions for these cases are explained in the following.

In the case where the front lies inside the wick (Fig. 2.4a), the temperatures at the liquid and vapor pores connected by a partially filled throat are given by the saturation temperature at the vapor pores, which depends on the vapor pressure,

$$T_i = T_k = T_{sat}(p_i). \quad (2.15)$$

The heat transfer condition (Eq. 2.9) at the liquid-vapor interface can be approximated by

$$A_{cv,mi} \lambda_{eff,mi} \frac{T_m - T_i}{L_t} - A_{cv,kn} \lambda_{eff,kn} \frac{T_k - T_n}{L_t} = \Delta h_{evp} \dot{M}_{evp,ik}, \quad (2.16)$$

which can be solved for the evaporation rate:

$$\dot{M}_{evp,ik} = \frac{1}{\Delta h_{evp}} \left(A_{cv,mi} \lambda_{eff,mi} \frac{T_m - T_i}{L_t} - A_{cv,kn} \lambda_{eff,kn} \frac{T_k - T_n}{L_t} \right). \quad (2.17)$$

The pressure difference between the vapor pore and the liquid pore is given by the capillary pressure

$$p_i - p_j = p_{c,ij} = \frac{2\sigma \cos \theta}{r_{t,ij}}. \quad (2.18)$$

In the case where the liquid pore is located at the top surface of the wick (Fig. 2.4b), the evaporation rate from pore i to the vapor outlet is computed by the heat balance equation

$$\dot{M}_{evp,ig} = \frac{A_{cv,ij} \lambda_{eff,ij} (T_j - T_i)}{\Delta h_{evp} L_t}. \quad (2.19)$$

2.3.4 Working fluid

The working fluid in LHPs and CPLs is chosen based on the operating temperature [6]. For a low operating temperature, ammonia or organic substances such as methanol or acetone are chosen as working fluid due to their low melting point and high vapor density. In the very high operating temperature range, the heat pipe is filled by liquid metal such as sodium or potassium. In this study, the major working fluid of the system is pure water. For LHPs and CPLs, water was shown to be one of the most suitable fluids for high operation temperatures (i.e. temperatures above 70 °C [6,23]) by comparing the measured heat transfer coefficient for different working fluids. In addition to pure water, methanol or ethanol is considered as a working fluid so as to compare and assess the effective heat transfer coefficient of a porous wick operating with a different type of working fluid. The physical-thermal properties of methanol and ethanol can be found in [6]. Due to the high

wettability of these working fluids on a solid substrate, glass in this study, the equilibrium contact angle θ is assumed to be zero.

Here, the equations of state for pure water were used according to the IAPWS Formulation 1995 [48]. For example, the temperature-dependent saturation vapor pressure is computed by

$$\ln\left(\frac{p_{sat}(T)}{p_{cr}}\right) = \frac{T_{cr} + 273.15}{T + 273.15} (a_1 v + a_2 v^{1.5} + a_3 v^3 + a_4 v^{3.5} + a_5 v^4 + a_6 v^{7.5}), \quad (2.20)$$

where T and T_{cr} denote the vapor and critical temperatures of water, respectively;

$$v = 1 - \frac{T + 273.15}{T_{cr} + 273.15} \quad \text{and} \quad a_1, a_2, a_3, a_4, a_5, a_6 \text{ denote empirically determined coefficients; } p_{cr}$$

denotes the critical pressure of pure water. The values of these parameters are given by $T_{cr} = 373.95$ °C, $p_{cr} = 22.06$ MPa, $a_1 = -7.85$, $a_2 = 1.84$, $a_3 = -11.78$, $a_4 = 22.68$, $a_5 = -15.96$ and $a_6 = 1.80$. The equations of state for other thermal properties such as the evaporation enthalpy, viscosity, thermal conductivity and density of liquid and vapor water can be found in [48]. For other application such as porous burners, the equations of state for the liquid fuels involved can be used in a similar way.

2.3.5 Numerical algorithm

Figure 2.5 illustrates the flow chart of the numerical algorithm implemented to determine the steady-state phase and temperature distributions inside a porous wick. First, the data structures of the pores and throats in the pore network are initialized. In the initialization routine, the throats in the first row underneath the fin are assumed to be empty, whereas all remaining throats are filled with liquid. The temperature field is computed by solving the system of Eqs. 2.6 for given boundary conditions (see Eq. 2.10 and Eqs. 2.12-2.15). After that, the thermal properties of vapor and water are updated by the equation of state for water [48]. The evaporation rates are determined by Eqs. 2.17 and 2.19, whereas the liquid and vapor pressure fields are obtained by solving the system of Eqs. 2.1-2.3. From the pressure field, the pressure difference Δp_{ij} between the vapor and the liquid pores of each interface throat is computed. These values are compared with the respective values of the throat capillary pressures. The pressure difference must be equal to the capillary pressure for menisci located inside the throats. However, for a meniscus located at the open end of a throat, the pressure difference may be smaller than the capillary pressure. Due to the discretization error, we assume that the location of the stationary liquid-vapor interface has been found when $\Delta p_{ij} \leq (1 + \xi) p_{c,ij}$ where ξ is a convergence criterion parameter, see Table 2.1. In the case where $\Delta p_{ij} > (1 + \xi) p_{c,ij}$, the throat ij becomes a vapor throat. After

updating the phase distribution, the new liquid-vapor interface throats are determined. Then the algorithm goes back to solving the energy equation and the overall procedure is iterated. The solution has converged when $\Delta p_{ij} \leq (1 + \xi) p_{c,ij}$ for all interface throats.

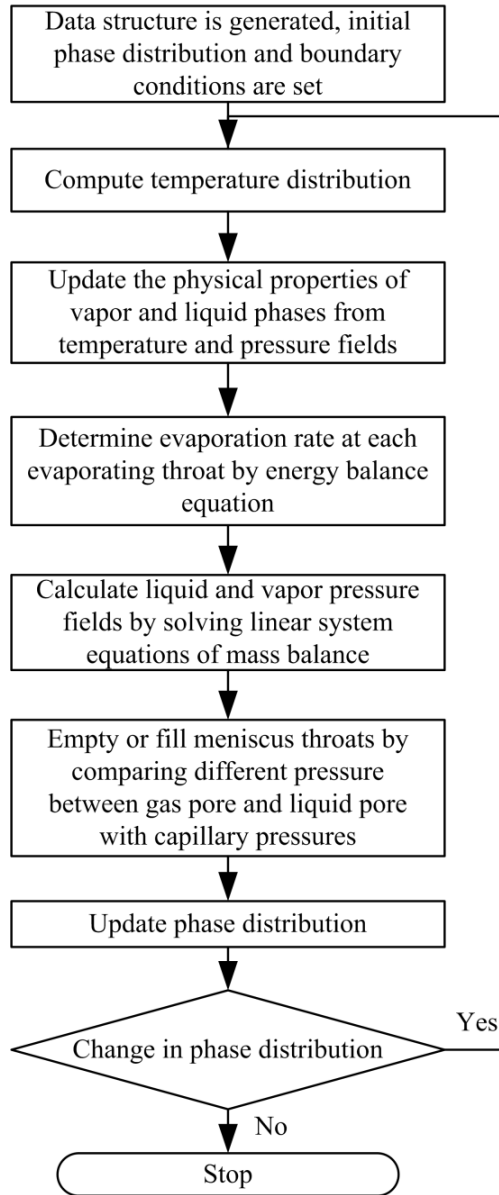


Figure 2.5: Flow chart of the numerical algorithm to determine the steady-state liquid-vapor interface inside the porous wick.

Because the vapor invasion within the network is mainly controlled by capillary action, the variation of the parameter ξ directly impacts the phase distribution. A lower value of ξ may lead to a solution with higher accuracy; however, it requires a longer computation time. In this sense, the parameter ξ introduces a trade-off between solution accuracy and the computational cost. As presented in Appendix B, the vapor area fraction varies only slightly (by less than 1%) when ξ increases from 0 to 0.01, whereas the computational time

is reduced by approximately 10%. Hence, the value of 0.01 was chosen for the simulations presented in this study.

2.4 Simulation results and discussion

The pore network model described in Sec. 2.3 is used to simulate the heat and mass transfer that occur in the computational domain shown in Fig. 2.1 during the wicking process. The numerical solution for the temperature and pressure distributions inside this domain as well as for the vapor pocket boundary is given for different values of the heat load. Moreover, the influence of the heat load, the porous structure, as well as the liquid inlet pressure and temperature on the heat transfer efficiency is investigated and discussed. The geometrical, physical, and numerical parameters used in the following pore network simulations are shown in Table 2.1. Although these throat diameters are not representative of a real porous wick structure, the parametric studies performed using the present model are still capable of capturing behaviors of the system under parameter variations.

Table 2.1: Parameters used for pore network simulations.

Parameter	Value	Unit
Number of columns in the pore network	50	-
Number of rows in the pore network	44	-
Horizontal length of the wick, L_x	49	mm
Vertical length of the wick, L_y	43	mm
Fin length	25	mm
Throat length, L_t	1000	μm
Throat radius, r_t	70	μm
Solid material	Glass	-
Thermal conductivity of solid phase, λ_s	10	W/mK
Vapor temperature at vapor outlet, T_{out}	100	$^{\circ}\text{C}$
Vapor pressure at vapor outlet, p_{out}	$p_{sat}(T_{out})$	Pa
Liquid inlet temperature, T_{in}	95	$^{\circ}\text{C}$
Liquid inlet pressure, p_{in}	$p_{out} - 100$	Pa
Convergence parameter, ξ	0.01	-

2.4.1 Model verification

Due to the irregular pore space structure of a real porous wick and the lack of information about the pore size distribution and throat length needed to generate a pore network, the operating characteristics of a pore network obtained from simulations cannot be fully experimentally validated. This pore network model will become predictive after further development and parametrization in well-defined experiments. Such a parametrization is not yet possible from the available data in the literature. In this work, the validity of the model is checked by comparing the heat transfer coefficient vs. the heat load with experimental observations extracted from Liao and Zhao [42]. Their experiment was conducted with a porous wick structured by staggered silver-copper cylinders with a diameter of 2 mm and water was used as the working fluid. In this section, the pore network simulations are performed for a throat length and radius of $L_t = 5$ mm and $r_t = 1$ mm, respectively. The effective heat transfer coefficient is calculated by

$$\alpha_{eff} = \frac{\dot{q}}{T_{fin} - T_{out}}. \quad (2.21)$$

Here $T_{fin} - T_{out}$ denotes the fin superheat value, which is the difference of the temperature at the center of the fin's bottom edge, T_{fin} , and of the vapor temperature at the vapor outlet, T_{out} . Since the heat transfer efficiency is proportional to α_{eff} , Eq. 2.21 implies that for a given heat load \dot{q} , a larger fin superheat value leads to a lower heat transfer efficiency of the capillary wick. The normalization is performed by comparing the temporary effective heat transfer coefficient α_{eff} and the heat load \dot{q} with their values at the incipient condition $\alpha_{eff, inc}$ and \dot{q}_{inc} (the lowest heat load where the vapor pocket starts to be formed under the fin). According to the experimental data, the incipient point is reached when the heat transfer coefficient starts to significantly decrease. The experimental heat load \dot{q}_{inc} and the effective heat transfer coefficient $\alpha_{eff, inc}$ at the incipient point are 189 kW/m² and 10 800 W/m²K, respectively, where the operating conditions are $T_{in} = 50^\circ\text{C}$, $p_{in} = p_{out} - 100$ Pa. Under these conditions, the respective values obtained from the simulation are $\dot{q}_{inc} = 175$ kW/m² and $\alpha_{eff, inc} = 33\,127$ W/m²K. The experimental effective heat transfer coefficient is significantly lower than the numerical value because the solid phase in the experimental apparatus is not inter-connected as in the pore network model. Therefore, the effective thermal conductivity and the conductive heat flux obtained for a real porous wick are smaller compared to the simulation values. The comparison between simulation and experimental observations is presented in Fig. 2.6. It can be seen that the effective heat transfer coefficients obtained from the pore network simulations for various values of the heat load follow a trend similar to the measured data. This qualitative agreement indicates

the predictive power of the model developed in the present study in the dry-out operating regime of an unsaturated capillary porous wick.

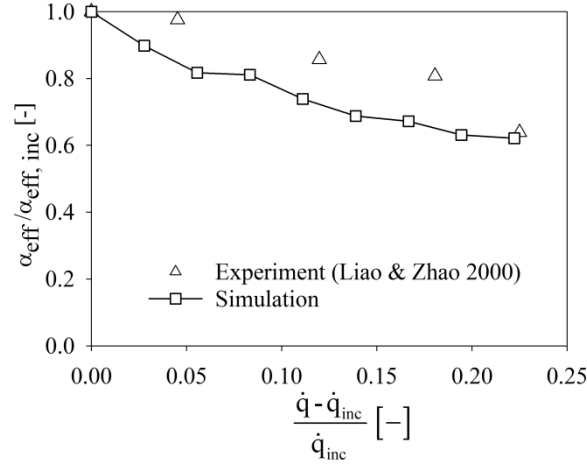


Figure 2.6: The effective heat transfer coefficient vs. the heat load during the dry-out operating regime with $T_{in} = 50^{\circ}\text{C}$, $p_{in} = p_{out} - 100$ Pa. The experimental data is extracted from Liao and Zhao [42].

2.4.2 Temperature and pressure distributions

In this section, the simulations are performed with pure water as the working fluid for two cases: (a) with constant thermal properties and (b) with thermal properties depending on both temperature and pressure. In case (a), the pore network model becomes similar to the model of Figus et al. [25]. However, in this work, the number of thermal nodes is two times smaller and the evaporation at the wet wick surface is taken into account. The temperature distribution as well as the evaporation front interface for a heat load of $\dot{q} = 140 \text{ kW/m}^2$ is presented in Fig. 2.7a. The evolution of the shape of the vapor pocket over time is qualitatively similar to previously published results [25]. However, a significant increase in temperature from the evaporation front to the top center of the porous wick in Fig.2.7a leads to a remarkable decrease of the vapor density, which can restrict the vapor transport. For a more realistic simulation, the dependency of the thermal properties on both temperature and pressure is taken into account (case (b)), and the simulation results are shown in Fig. 2.7b. The area fraction of the vapor region which is defined in Eq. 2.22 increases from 0.32 in case (a) to 0.39 in case (b):

$$f_v = \frac{A_{\text{vapor pocket}}}{A_{\text{porous wick}}}. \quad (2.22)$$

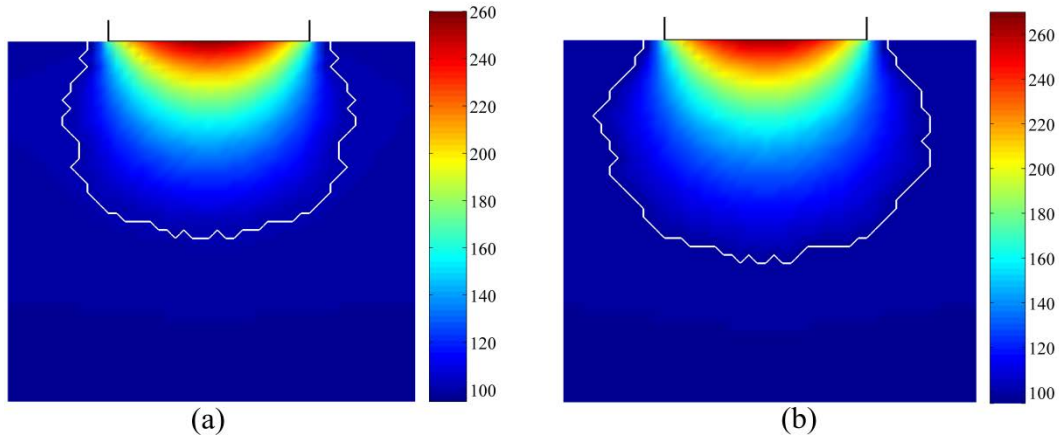


Figure 2.7: Spatial distributions of temperature at steady state for $\dot{q} = 140 \text{ kW/m}^2$: (a) with constant thermal properties, (b) with thermal properties that depend on both temperature and pressure. The liquid-vapor interface is indicated by a white line and the color indicates the temperature in $^{\circ}\text{C}$.

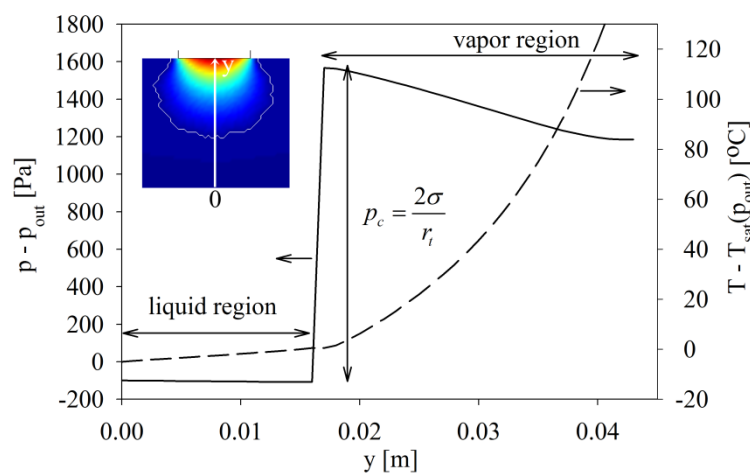


Figure 2.8: Cross-section of the pressure and temperature profiles in the pore network along the vertical arrow shown in the inset; $\dot{q} = 140 \text{ kW/m}^2$.

The reason for this increase is that the decrease in vapor density strongly intensifies both the kinematic viscosity of the vapor phase and the hydraulic resistance in the vapor region (c.f. Eq. 2.1). Therefore, the vapor pressure at the liquid-vapor interface increases and the liquid invades further. As a result, the size of the vapor pocket is larger in case (b) than in case (a).

Vertical cross-sections of the pressure and temperature profiles for case (b) are shown in Fig. 2.8. It can be seen that the temperature of the liquid and vapor phases at the evaporation front is equal to the saturation temperature at local vapor pressure $T_{\text{sat}}(p_v) = 100.44 \text{ }^{\circ}\text{C}$. Inside the vapor pocket, the vapor is superheated and the temperature maximum is located at the fin center. There is a discontinuity in the pressure field at the liquid-vapor interface. In the cross section (Fig. 2.8) it is shown that the liquid pressure decreases

slightly (by 8 Pa) within the liquid region. A large jump of the pressure occurs at the liquid-vapor interface due to the capillary pressure at the meniscus throats, where the pressure reaches its highest value. Note that although this jump is the driving force of the vapor and liquid transport, it was not shown in previous 2D pore network simulations [25]. In the vapor region, the pressure decreases due to the vapor flow from the liquid-vapor interface towards the dry wick surface. The pressure drop in the vapor region is more significant than in the liquid region (329 Pa). The difference between these pressure drops can be explained by the difference in kinematic viscosity ν between the liquid and vapor phases (in this simulation, the average kinematic viscosity of water in the liquid region is $3.01 \times 10^{-7} \text{ m}^2/\text{s}$, whereas the kinematic viscosity of vapor varies noticeably between $2.04 \times 10^{-5} \text{ m}^2/\text{s}$ at the evaporation front and $4.50 \times 10^{-5} \text{ m}^2/\text{s}$ at the center of the fin's bottom edge). The significant variation in the kinematic viscosity of the vapor indicates that incorporating the dependency of physical-thermal properties on the temperature and pressure can improve the accuracy of the model, especially for large heat load values, where a huge temperature gradient appears (see Fig. 2.7 for instance). Therefore, this dependency is taken into account in the following computations.

A supplementary investigation on the convective heat transfer and on the viscous dissipation is addressed in Appendix C. With the heat load $\dot{q} = 140 \text{ kW}/\text{m}^2$, the average interstitial velocities v_0 of the vapor and liquid phases are 0.45 m/s and $2.80 \times 10^{-4} \text{ m}/\text{s}$, whereas the average superficial velocities v of these phases are $6.90 \times 10^{-3} \text{ m}/\text{s}$ and $4.30 \times 10^{-6} \text{ m}/\text{s}$, respectively. The convective heat flux in the vapor and liquid regions is only 0.08% and 0.18% of the conductive heat flux, respectively. Furthermore, the temperature increase due to viscous heating in vapor and liquid flows in throats with vertical dimension $L_y = 0.044 \text{ mm}$ is only 0.51 K and 0.011 K, respectively; these values are much smaller than the fin superheat value at operating condition, $T_{fin} - T_{out} = 164.32 \text{ K}$. This implies that both convective heat transfer and viscous dissipation are truly negligible in the present pore network configurations.

2.4.3 Influence of the heat load on the shape of the vapor pocket and on the heat transfer efficiency

The effect of the heat load on the heat and mass transfer inside the porous wick is investigated in this section. The pore network simulations are carried out with the heat load \dot{q} varying from $20 \text{ kW}/\text{m}^2$ to $163 \text{ kW}/\text{m}^2$ and the simulation results are presented in Figs. 2.9 and 2.10. At $\dot{q} = 20 \text{ kW}/\text{m}^2$, the vapor pocket appears underneath the fin, where the vapor only occupies 2.72% of the porous area (Fig. 2.9a). As the heat load increases to $60 \text{ kW}/\text{m}^2$, the vapor pocket primarily expands towards the network bottom (Fig. 2.9b) while the vapor reaches the outlet through a narrow neck. With further increasing heat load,

several liquid throats near the neck empty and thus the vapor pocket starts to expand in the lateral direction. This leads to a decrease of the pressure inside the vapor pocket and several empty throats are refilled at the same time (Fig. 2.9c), such that the vapor pocket shrinks. As the heat load increases further, the vapor pocket expands again (Fig. 2.9d). The lengths of the dry edges DE and FG at the wick surface (c.f. Fig. 2.1) remain unchanged because the vapor outflow is not strong enough to invade the liquid throats at the surface. With an even higher heat load, the liquid throats at the surface are finally invaded and the hydraulic resistance of the vapor phase decreases again. Therefore, the vapor pressure inside the pocket drops and several empty throats are refilled by liquid, which leads to a decrease of the vapor pocket size (Fig. 2.9e). This inflation and deflation behavior of the vapor pocket repeats with further increasing heat load (Fig. 2.9f).

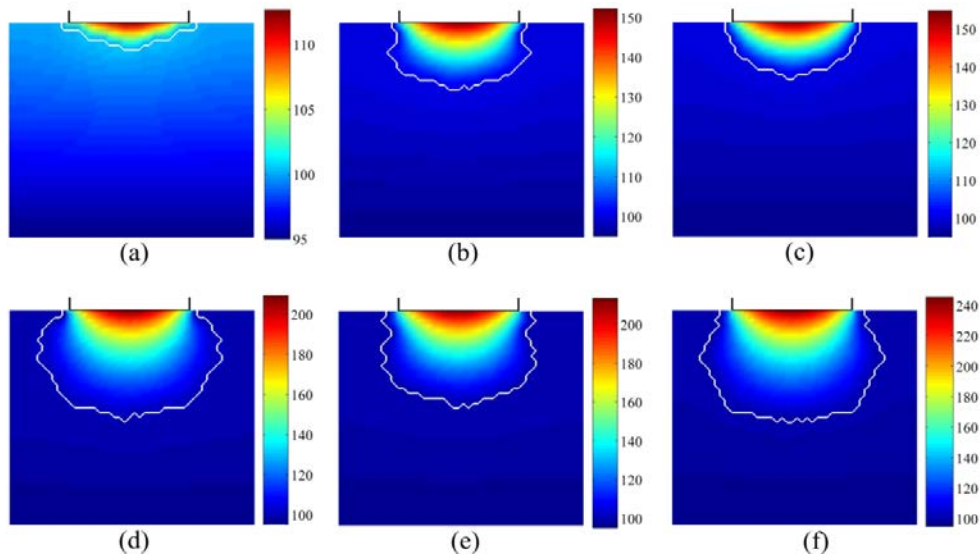


Figure 2.9: Temperature distribution for different values of the heat load: (a) $\dot{q} = 20$ kW/m², (b) $\dot{q} = 60$ kW/m², (c) $\dot{q} = 70$ kW/m², (d) $\dot{q} = 100$ kW/m², (e) $\dot{q} = 110$ kW/m², (f) $\dot{q} = 130$ kW/m² (The color indicates the temperature in °C).

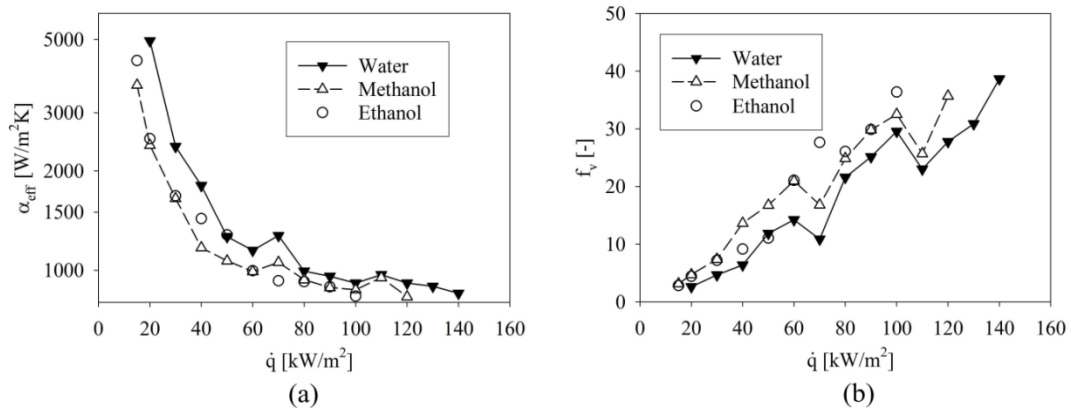


Figure 2.10: The influence of the heat load \dot{q} on the effective heat transfer coefficient α_{eff} and on the area fraction of the vapor region f_v .

The influence of the heat load on the effective heat transfer coefficient is shown in Fig. 2.10a. As the heat load increases, the distance between the heat source (fin) and the liquid-vapor interface inside the porous wick increases first and then fluctuates. Consequently, the thermal resistance between the fin and the evaporation front increases first – due to the lower thermal conductivity in the vapor phase – and then fluctuates. To quantify the evolution of the vapor pocket for increasing heat load more precisely, the area fraction of the vapor region f_v is calculated and shown in Fig. 2.10b. For a given value of the heat load \dot{q} , the area fraction of the vapor region f_v is defined as the vapor area divided by the total area of the porous wick. One can clearly see that as the heat load increases, the area fraction of the vapor region fluctuates due to the inflation/deflation of the vapor pocket described before. The influence of the heat load on the Péclet number and on the viscous dissipation in the case where water is used as a working fluid is presented in detail in Appendix C.

The simulation results obtained from three different types of working fluids are also shown in Fig. 2.10. Considering the vapor area fraction, the inflation/deflation phenomenon is also observed with both methanol and ethanol. Due to a lower evaporation enthalpy of methanol and of ethanol compared to water (the evaporation enthalpies of methanol, ethanol and water at 100°C are 1030 kJ/kg, 927 kJ/kg and 2251 kJ/kg, respectively), the evaporation rate obtained with methanol and ethanol is smaller compared to water. Although the kinematic viscosity of methanol or of ethanol is higher than that of water, the higher evaporation rate and lower surface tension lead to a deeper invasion of vapor phase. As a result, the distance between the fin and the evaporation front increases and the effective heat transfer coefficient decreases. These results are in favor of water as the most effective working fluid at high temperature for LHPs and CPLs [5].

The inflation/deflation phenomenon observed in the simulations may explain the fluctuation of the heat transfer coefficient found in experimental studies [36,42,43]. However, this phenomenon still needs to be confirmed by sophisticated pore-scale experiments. Optical microfluidic models or X-ray microtomography might be used to visualize and quantify this phenomenon in future work.

2.4.4 Influence of the porous structure on the heat transfer efficiency

a) Discrete and continuous unimodal throat radius distributions

To examine the heat transfer efficiency of different porous structures, the situation of a constant throat radius was explored first. Note that water is used as the working fluid throughout the remaining sections. The simulations are performed for throat radii r_t of 50, 60, 70 μm , for a pressure difference of $\Delta p = p_{out} - p_{in} = 400$ Pa. The results are presented in Figs. 2.11 and 2.12.

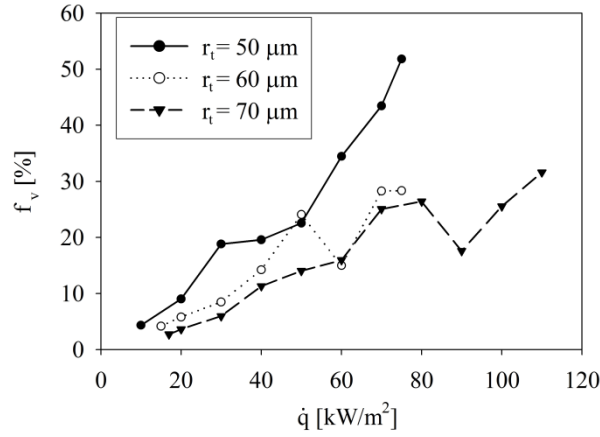


Figure 2.11: The influence of throat radius r_t on the vapor region f_v at $\Delta p = 400$ Pa.

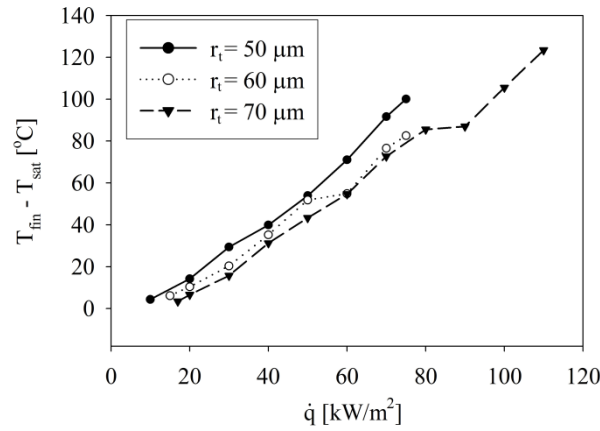


Figure 2.12: The influence of throat radius r_t on the area fraction of the fin superheat value $T_{fin} - T_{out}$ at $\Delta p = 400$ Pa.

As shown in Fig. 2.11, at the same heat load value, the vapor area fraction increases with decreasing throat radius. This implies that the vapor pocket expands with small throat radius compared to larger throat radius. The primary reason for this reduction of the heat transfer efficiency is the influence of throat radius on both capillarity and hydraulic resistance. On one hand, the capillary threshold is inversely proportional to the radius. As a result, a smaller throat size leads to a higher capillary threshold. On the other hand, the pressure drop in both vapor and liquid transport is inversely proportional to 4th power of radius, where the evaporation rate approximately calculated by Eq. 2.23

$$\dot{M}_{evp} = \frac{\dot{q} \cdot A_{fin}}{\Delta h_{evp}}, \quad (2.23)$$

varies only slightly because the temperature at the liquid-vapor interface approximates T_{out} . With the same p_{out} , this implies that the vapor pressure within the network is inversely proportional to 4th power of radius. Combining the two mentioned effects of throat size on capillary pressure and on vapor pressure, for a certain decrease of throat radius, the

increase in vapor pressure (inversely proportional with 4th power) dominates the increase in capillary pressure (directly inversely proportional). Furthermore, the liquid pressure at the liquid-vapor interface also decreases with decreasing throat radius. Consequently, the increase in vapor-liquid pressure difference at the evaporation front dominates the increasing of capillarity. The vapor phase invades further into the wick with smaller throat size. The vapor pocket expansion in vertical direction helps to reduce the flow path of liquid phase, whereas its expansion in horizontal direction helps to increase the dry part of vapor outlet (edges DE and FG). Conclusively, the area fraction of the vapor region generally increases with decreasing throat radius (Fig. 2.11). Meanwhile, the large distance between the fin and the liquid-vapor interface corresponding to network with small throat radius, due to high area fraction of vapor phase, leads to a higher fin superheat value $T_{fin} - T_{out}$ compared to the large throat radius network (c.f. Fig. 2.12).

However, for certain heat load values ($\dot{q} = 50 \text{ kW/m}^2$ and $\dot{q} = 60 \text{ kW/m}^2$ in Fig. 2.11), this general observation is not true. These exceptions can be explained by the inflation/deflation phenomenon described in Sec. 2.4.3. The distance between the hot surface and the evaporation front fluctuates with increasing heat load, which leads to a fluctuation of the fin superheat value.

In reality, porous structures are neither homogeneous nor isotropic. Consequently, a network with uniform throat diameter cannot be representative of a real porous wick. The results obtained for a uniform throat radius are nonetheless useful because they show the benefit of using throats with variable size. In order to understand the pore-scale heat and mass transfer for a more realistic structure, the throat radii are sampled from a normal distribution with mean r_0 , and standard deviation σ_0 in the next example:

$$\frac{dN}{dr_i} = \frac{1}{\sigma_0 \sqrt{2\pi}} e^{-\frac{(r-r_0)^2}{2\sigma_0^2}}. \quad (2.24)$$

The mean throat radius is set to $r_0 = 70 \text{ }\mu\text{m}$, whereas the standard deviation σ_0 varies from $0.02r_0$ to $0.2r_0$. The simulation results for $\dot{q} = 80 \text{ kW/m}^2$ are shown in Fig. 2.13. The morphology of the evaporation front changes significantly with the standard deviation of the throat radius distribution. In comparison to the previous case with constant throat size, the liquid is more easily pumped from the bottom to the evaporation front in small throats (due to the high capillary pressures). Furthermore, large throats are more easily invaded by the vapor phase due to lower capillary thresholds. It should be noted that by keeping the mean throat radius constant, the average permeability of the network does not depend on the throat size distribution. In this case, evaporation area is provided by the large throats, whereas the liquid is pumped through the small throats from the inlet to the evaporation front. This effect is more pronounced for a broader throat radius distribution (higher

standard deviation), such that several capillary-viscous vapor fingers appear at the evaporation front. This (fractal) behavior of the interface, as in a typical invasion process, is determined by the interplay between viscous and capillary forces [49].

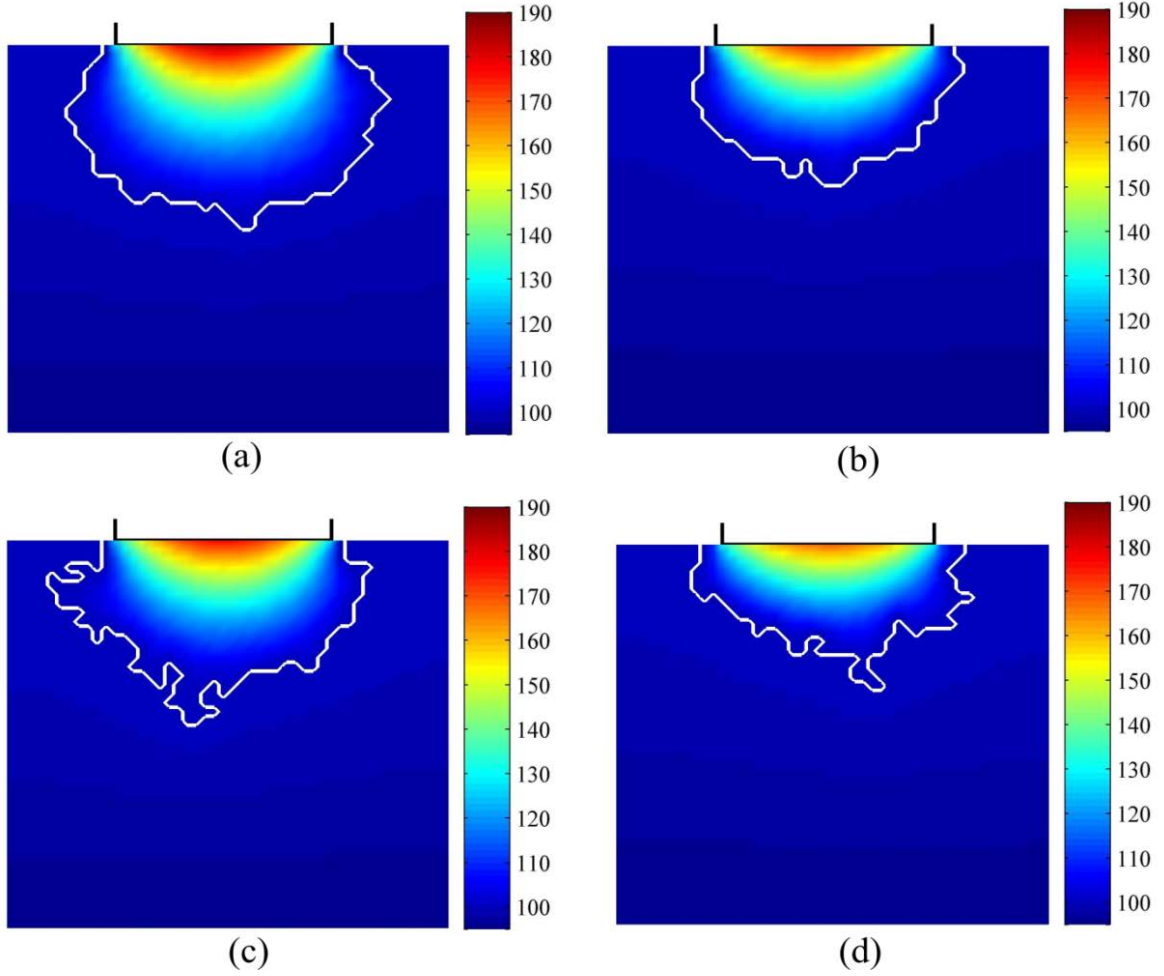


Figure 2.13: Morphology of the liquid-vapor interface and temperature distribution in the porous wick for different values of the standard deviation of the unimodal throat radius distribution (a) $\sigma_0 = 0.02r_0$, (b) $\sigma_0 = 0.05r_0$, (c) $\sigma_0 = 0.1r_0$, and (d) $\sigma_0 = 0.2r_0$ at $\dot{q} = 80$ kW/m² and $\Delta p = 400$ Pa (The color indicates the temperature in °C).

Because small throats near the fin can hardly be invaded by the vapor phase, the area fraction of the vapor region decreases (from 24.81% with $\sigma_0 = 0$ to 14.63% with $\sigma_0 = 0.2r_0$) for increasing standard deviation. Therefore, the fin superheat value decreases from 84.14 °C with $\sigma_0 = 0.02r_0$ to 67.77 °C with $\sigma_0 = 0.2r_0$ (note that the fin superheat value for the uniform throat size $r = 70$ μm is 85.53 °C). This implies that the heat transfer efficiency is enhanced for a non-constant throat size.

b) Continuous bi-modal throat radius distribution

From the simulation results for pore networks with unimodal throat radius distributions, it was conceived that a pore network with a bi-modal throat radius distribution might further enhance the heat and mass transfer in the porous wick. In this section, a pore network with a bi-modal throat radius distribution was generated, containing vertical macro channels (c.f. Fig. 2.14). While the network of small throats provides a high liquid pumping capacity, the network of large throats acts as an evaporative heat exchanger. This idea was shown to work in a bi-porous wick [44,50]; a theoretical explanation is not given in the literature, however.

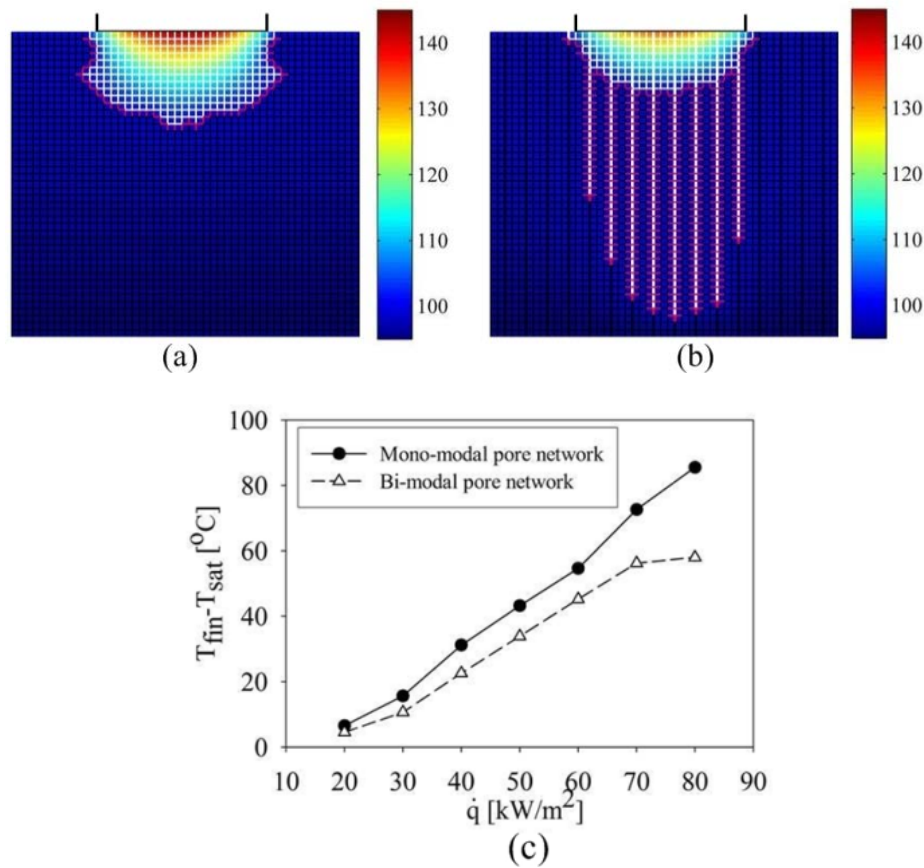


Figure 2.14: Temperature distributions for (a) a unimodal pore network with constant throat size $r = 70 \mu\text{m}$ and (b) a bi-modal pore network at $\dot{q} = 80 \text{ kW/m}^2$ and $\Delta p = 400 \text{ Pa}$ (The color indicates the temperature in °C, black lines: liquid throats, white lines: vapor throats, red lines: partially filled throats). (c) Influence of the heat load \dot{q} on the fin superheat value $T_{fin} - T_{out}$ in unimodal and bi-modal pore networks at $\Delta p = 400 \text{ Pa}$.

The pore network simulations are performed for a network with bi-modal throat radius distributions. Starting with a unimodal pore network with constant throat size $r = 70 \mu\text{m}$ ($\sigma_0 = 0$), macro channels with a radius of $r_{ch} = 1.5r$ are inserted in every third column to

create a bi-modal pore network. The simulation results for a pressure difference of $\Delta p = 400$ Pa are presented in Figs. 2.14a-b. It can be seen that the macro channels are preferentially invaded by the vapor phase due to lower entry capillary thresholds p_c (c.f. Eq. 2.18). Several vapor channels develop in the pore network (Fig. 2.14b) and the vapor pocket is smaller compared to the pore network with a unimodal pore radius distribution (Fig. 2.14a). The liquid and vapor flows are separated: the liquid is transported through the small throats by capillary action, whereas the vapor escapes through the macro channels, as expected. Because the vapor pocket is smaller, the distance between the heat source and the liquid-vapor interface is reduced compared to the network with the unimodal pore radius distribution. Therefore, the fin superheat value is also smaller (Fig. 2.14c).

c) *Bi-layer pore network structures*

Another idea to enhance the heat and mass transfer inside the porous wick is to insert an additional porous layer with large throat radii on top of the current porous wick. Again, the finer porous layer would operate as a capillary pump at the bottom while the coarser porous layer would act as an evaporative heat exchanger at the top. This idea was introduced in the work of Mottet et al. [26]; in the present thesis, the effect of the coarse layer thickness is evaluated and quantified via pore network simulations.

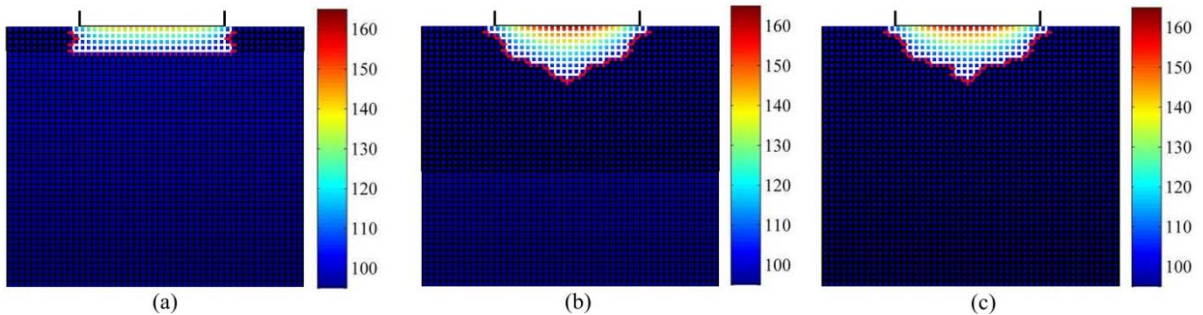


Figure 2.15: Temperature distributions for bi-layer porous wicks with relative coarse layer thickness (a) $e = 9.3\%$, (b) $e = 55.8\%$, and (c) $e = 100\%$ at $\dot{q} = 100$ kW/m² and $\Delta p = 400$ Pa (black lines: liquid throats, white lines: vapor throats, red lines: partially filled throats; the color indicates the temperature in °C).

Starting with the original unimodal pore network with throat radius $r = 70$ μm and standard deviation $\sigma_0 = 0.02r$ (c.f. Sec. 2.4.4a), the radii of several throats near the top of the network were increased by a factor of 1.5. The thickness of the resulting coarse layer is denoted as L_{coarse} , and $e = L_{coarse}/L_y$ denotes the relative coarse layer thickness. Simulations are performed for several values of e ranging from 9.3% to 100%, and the corresponding results are presented in Figs. 2.15 and 2.16. Note that for $e = 0\%$, the pore network is unimodal with only small throats, whereas for $e = 100\%$, the pore network becomes

unimodal with only large throats. It can be seen that for small values of e (Fig. 2.15a), the vapor pocket touches the surface of the fine porous layer below. The high capillary effect of the fine layer at the liquid-vapor interface increases the pumping capacity of the porous wick. Therefore, the liquid is supplied from the bottom up to the macro channels. The depth of the vapor pocket is smaller compared to the unimodal pore network (Fig. 2.13a), which leads to a higher heat and mass transfer efficiency as well as to a significantly smaller fin superheat value (Fig. 2.16).

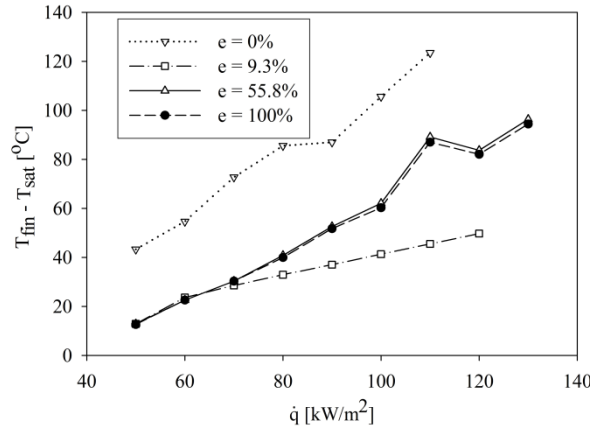


Figure 2.16: Influence of the heat load \dot{q} on the fin superheat value $T_{fin} - T_{out}$ for bi-layer pore networks at $\Delta p = 400$ Pa.

If the thickness of the coarse layer becomes larger ($e = 55.8\%$), the vapor pocket does not touch the fine porous layer anymore (Fig. 2.15b). In this case, the liquid flow is restrained due to a lower permeability and thus the fin superheat value becomes slightly larger compared to the case of $e = 100\%$. However, because the fine layer thickness is small, the liquid pressure at the evaporation front decreases slightly and the heat transfer efficiency obtained with $e = 100\%$ is similar to that at $e = 55.8\%$. With $e = 100\%$ (Fig. 2.15c), a unimodal pore network with macro channels provides a higher heat and mass transfer efficiency than a unimodal pore network with micro channels. This result also matches with the results presented in Sec. 2.4.4a.

2.4.5 Influence of the liquid inlet pressure and of the liquid inlet temperature on heat transfer efficiency

As discussed in the Sec. 2.1, the considered porous wick and its fluid configuration stems from a situation encountered in LHP evaporator which is connected with a condenser through liquid and vapor transport lines to create a closed loop. During LHP operation, the liquid pressure in the reservoir depends on the hydraulic resistance of the transport lines and on the condenser pressure whereas the temperature is controlled by the heat transfer efficiency inside the condenser and along the transport lines. A change in ambient pressure or temperature affects directly the liquid phase at the inlet of the evaporator. In

this section, the influence of the liquid inlet temperature T_{in} and pressure p_{in} (c.f. Fig. 2.1 (right)) on the heat transfer efficiency of the evaporator is discussed.

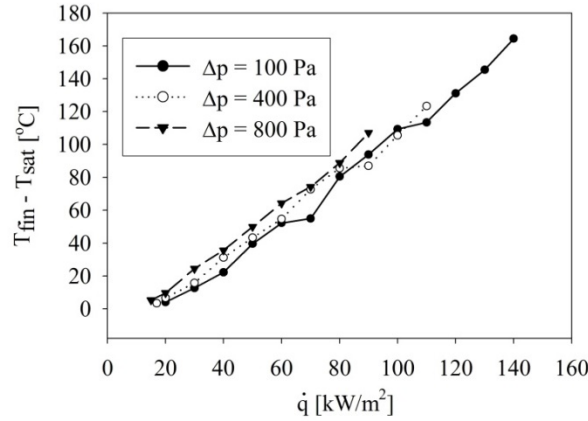


Figure 2.17: Influence of the inlet liquid pressure p_{in} on the fin superheat value $T_{fin} - T_{out}$. Note that an increasing pressure difference Δp corresponds to a decreasing inlet pressure.

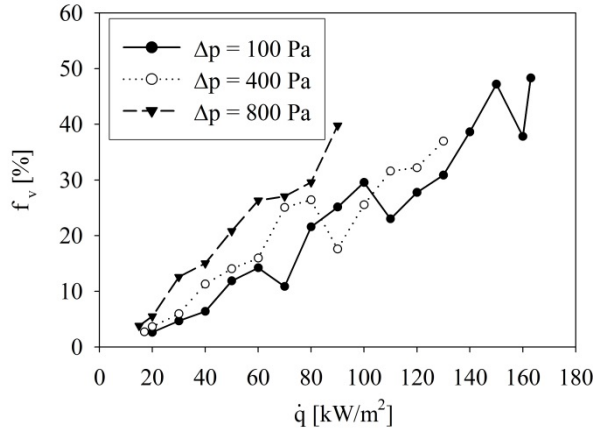


Figure 2.18: Influence of the inlet liquid pressure p_{in} on the area fraction of the vapor region f_v .

Simulations were performed for a unimodal pore network throat radius $r = 70 \mu\text{m}$, standard deviation $\sigma_0 = 0.02r$ (c.f. Sec. 2.4.4a) with varying Δp from 100 Pa to 800 Pa and $T_{in} = 95^\circ\text{C}$ (where, $\Delta p = p_{out} - p_{in}$; p_{out} remained constant at $p_{sat}(T_{out})$). The simulation results are presented in Figs. 2.17 and 2.18. It is observed that both the fin superheat value and the area fraction of the vapor region f_v generally increase with Δp . This is due to the fact that with a lower liquid inlet pressure, the replenishment of liquid at the heated surface becomes more difficult. Thus the vapor pocket expands and the distance between the evaporation front and the fin surface increases. Therefore, the fin superheat value increases for decreasing liquid inlet pressure. However, several exceptions are observed. Because of the inflation/deflation phenomenon described in Sec. 2.4.3, the fraction of the vapor region on the wick surface as well as the distance between the fin and the liquid-vapor interface

fluctuate as the heat load increases. This leads to a fluctuation of the fin superheat value, such that the fin temperature for a larger liquid inlet pressure may be lower than for a smaller liquid inlet pressure (compare the values for $\dot{q} = 90 \text{ kW/m}^2$ in Fig. 2.17, for example).

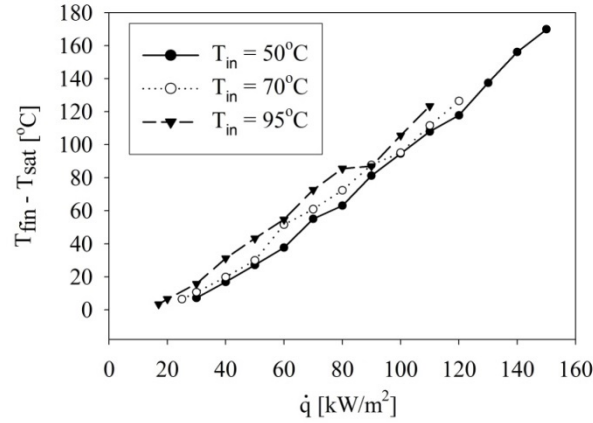


Figure 2.19: Influence of the inlet temperature T_{in} on the fin superheat value $T_{fin} - T_{out}$ at $\Delta p = 400 \text{ Pa}$.

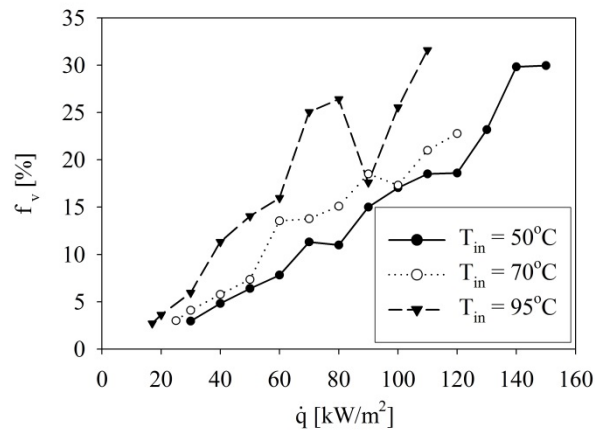


Figure 2.20: Influence of the inlet temperature T_{in} on the area fraction of the vapor region f_v at $\Delta p = 400 \text{ Pa}$.

The effect of the liquid inlet temperature is investigated by varying T_{in} from 50°C to 95°C for a constant $\Delta p = 400 \text{ Pa}$. The results are shown in Figs. 2.19 and 2.20. As the inlet temperature increases, the amount of thermal energy needed to heat up the liquid phase from the inlet temperature to the saturation temperature decreases. Therefore, a lower inlet temperature leads to a smaller vapor pocket, as shown in Fig. 2.20. The smaller distance between the fin surface and the evaporation front enhances the heat transfer efficiency and a lower fin superheat value is obtained (Fig. 2.19). However, for certain values of the heat load (such as for $\dot{q} = 90 \text{ kW/m}^2$), this general tendency is reversed due to the inflation/deflation phenomenon, as explained in the previous paragraph.

2.5 Conclusion

The major conclusions from the pore network simulations described in this chapter are summarized in Table 2.2. The results from this section can claim validity for an individual unsaturated capillary porous wick, such as in porous burners, whereas a coupling between the evaporator and the remaining components of LHPs and CPLs is required to investigate the operation characteristics of a complete closed loop. Recently, Boubaker and Platel [51] showed numerically that the size of the vapor pocket is nearly independent of the applied heat load in a complete loop of heat pipes. This observation still needs to be experimentally confirmed. It may stem from the coupled effects of thermal and hydrodynamic mechanisms involved in the interactions between the evaporator and the rest of the loop. Due to the high computational cost, this coupling was not included in the present work. In future, both experimental and theoretical studies should be carried out to evaluate the heat and mass transfer efficiencies of LHPs and CPLs in a fully coupled system.

Table 2.2: A summary of the pore network simulation results. “↑” indicates an increase, “–” indicates no or only a slight change, and “↓” indicates a reduction.

Pore network	Parameter	$T_{fin} - T_{out}$ and f_v
Unimodal	Mean throat radius, r_0 ↑ (Figs. 2.11, 2.12)	↓
	Standard deviation, σ_0 ↑ (Fig. 2.13)	↓
	Liquid inlet pressure, p_{in} ↑ (Figs. 2.17, 2.18)	↑
	Liquid inlet temperature, T_{in} ↑ (Figs. 2.19, 2.20)	↑
Bi-modal	Compared to unimodal (Fig. 2.14)	↓
Bi-layer	Relative thickness of coarse layer, e ↑ (Figs. 2.15, 2.16)	first ↓ and then ↑

Chapter 3

Pore network simulations of the superheated steam drying process in porous media

This chapter is a modified version of the paper *Discrete pore network modeling of superheated steam drying* published in *Drying Technology* (2017), DOI: 10.1080/07373937.2016.1264414.

3.1 Literature review

To preserve the product quality as well as to reduce the logistics and storage cost, dehydration of porous materials using various drying techniques (such as hot air convective drying, freeze drying, microwave drying) is widely applied. The so-called superheated steam drying (SSD) is a promising drying technique, because of its large potential for saving energy and for improving product quality. In SSD, superheated steam is used as the drying agent. There is no oxygen present, and thus oxidation or combustion does not occur. Therefore, SSD often yields a better product quality than hot air drying [29]. Another benefit of SSD is that the drying rate may be enhanced compared to hot air drying due to the high product temperature and lack of diffusional resistance in the vapor transport – therefore, the drying time can be reduced. Moreover, the moisture evaporated from the drying product is steam at a low specific enthalpy, which means that it can be reused as a drying agent or be exhausted in condensed liquid form after recycling the energy. Hence, a superheated steam dryer can have much higher energy efficiency than a traditional convective dryer. Because of these advantages, SSD has been widely applied in many industrial processes such as in the drying of beet pulps, coal, peat, sludge, lumber, paper and tissues [29,52–54].

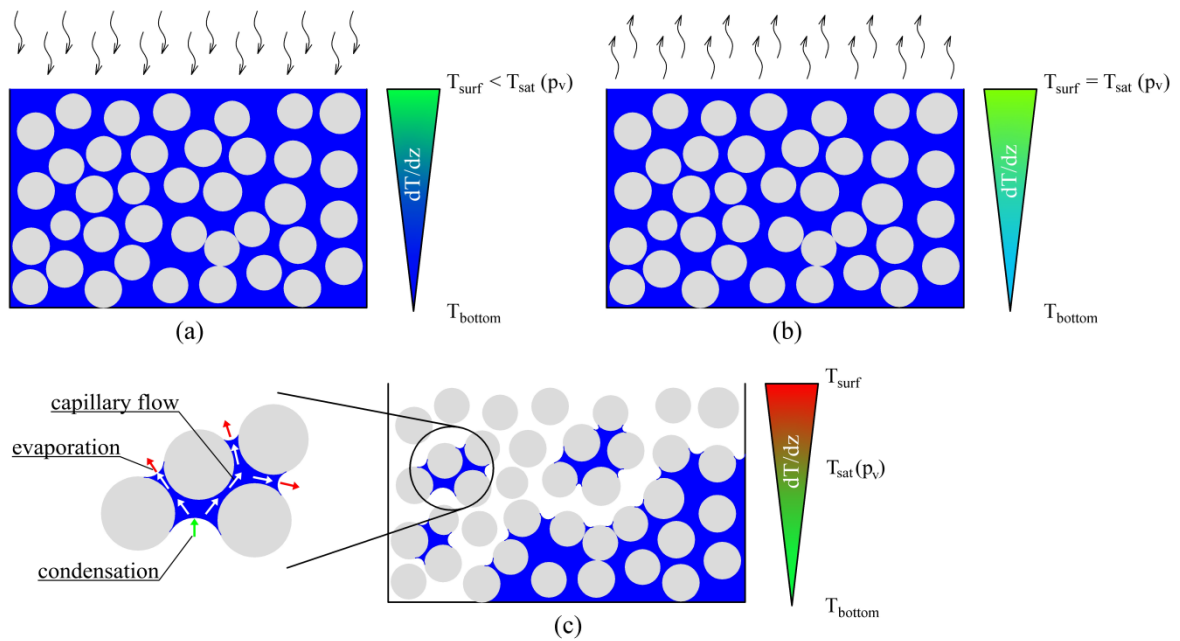


Figure 3.1: Illustration of the three periods of superheated steam drying: (a) initial condensation period, (b) surface evaporation period and (c) main drying period. The color maps represent the vertical temperature distribution. The colored and white arrows indicate the vapor and liquid flows, respectively.

As discussed in the literature [55,56], the SSD of porous media is assumed to comprise three periods during each of which different mechanisms occur (c.f. Fig. 3.1). Firstly, when the surface temperature of the drying product is lower than the steam saturation temperature, water vapor condenses on the product surface. This is the so-called *surface condensation period*. The product is heated by both latent and sensible heat during this period. If the porous medium is fully saturated, a liquid film forms on its surface. Next, the surface temperature reaches the steam saturation temperature and the free surface liquid starts to evaporate. During the *surface evaporation period* the water film generated previously by condensation evaporates. Note that during the surface condensation and evaporation periods, the porous medium remains fully saturated with liquid. During the *main drying period*, the moisture inside the product is removed due to evaporation. The vaporization occurs inside of the porous material, and the generated vapor is transported through the network of interconnected dry pores towards the surface due to a driving pressure difference. In the liquid phase, the free water available in the pores is pumped towards the surface of the medium by capillary action and evaporates first, whereas bound water is trapped inside the pores and evaporates later. Initially, as the medium surface is sufficiently wet, the drying process progresses at a high drying rate. This is called the quasi-constant drying rate (CDR) stage. Once the medium surface dries out and the evaporation front recedes into the medium, the falling drying rate (FDR) stage begins: the drying rate decreases over time due to the added hydraulic resistance for the vapor

transport from the evaporation front to the medium surface. The drying process finishes when the liquid is completely removed from the porous medium.

Several experimental and theoretical studies of the heat and mass transfer inside the porous material during the SSD process have been carried out. Most models were developed based on the receding wet core and dry outer crust formation hypothesis [57,58] or on the phenomenological concept of an effective water diffusivity [55,59–62]. In the frame of receding wet core models [57,58], the liquid is assumed to be stationary and the drying rate as well as the velocity of the evaporation front are computed from the energy balance equation at the wet core-dry crust interface. The surface condensation period is considered in the model proposed by Chen et al. [57]. However, the vapor pressure at the interface, which is required to calculate the drying rate, is given by empirical equations. Therefore, the model proposed by Chen et al. [57] is valid only for certain types of ceramic products and coal, for which these equations have been determined experimentally. Regarding the diffusional models, the effective water diffusion coefficient is an important parameter for the calculation since it governs the moisture transport. In the work of Iyota et al. [55], the value of this parameter determined experimentally for hot air drying is used to perform the simulation for SSD. To estimate the effective water diffusion coefficient for the SSD process, several empirical correlations were proposed for different materials [59–62]. The three-dimensional models presented in the work of Devahastin and his co-authors [61,62] are noteworthy because they can describe the drying behavior of a product which undergoes shrinkage. However, in these models the mass transfer inside the product is governed by liquid diffusion only and the vaporization occurs exclusively at the product surface: hence, the vapor transport inside the porous medium is neglected. Continuum-scale models that take into account both the liquid and the vapor transport resistance were also developed, based on the volume averaging technique, to simulate the SSD process [63–66]. For the SSD process within a packed bed of porous particles, hybrid models were developed [64,66], which combine volume-averaged transport equations for the thermal energy and for the fluid transport in the packed bed with published drying kinetics of single porous particles [63]. The continuum-scale models cited up to this point deal with homogeneous and isotropic porous materials. Despite their strengths, the influence of properties such as the wettability, pore shape, pore size distribution, pore structure, etc. on the drying behavior cannot be investigated through these continuum-scale models since these properties are lumped together in several effective parameters. Therefore, the understanding and interpretation of transport phenomena at the pore-scale during the SSD process, which can provide information and guidance for improving the drying performance, is not possible with these continuum-scale models.

To investigate transport processes related to both single and multiphase flows in porous materials, discrete pore-scale models have been widely used in the literature [67–70].

These discrete models enable the investigation of the heat and mass transfer by solving the transport equations directly at the pore-scale. Fluid flow in a heterogeneous porous material can be better understood in this way. Furthermore, a better macroscopic understanding of the transport processes in porous media can be provided by computing macroscopic transport coefficients such as the relative permeabilities of gas and liquid phases, or the capillary pressure – as functions of the saturation – from pore-scale simulation results [49]. Due to these merits, pore-scale approaches have been widely used for modeling and simulation in the context of various applications such as liquid imbibition [17,71], oil recovery [18], water management in the porous layer of fuel cells [20], and fluid transport in the porous wick of a loop heat pipe [21,72]. Based on the invasion percolation algorithm proposed by Wilkinson and Willemsen [73], several non-isothermal pore network models [74–77] were developed to simulate the hot air drying process. The motivation for the present work stems from the fact that pore condensation is only partly treated in these published pore network models. This means that the liquid generated by condensation in full throats containing a liquid-vapor interface (i.e. meniscus throats) is simply discarded. Although the condensation rate is small compared to the evaporation rate [46,74], the refilling of empty pores/throats, which was neglected in the earlier models, might impact significantly the phase distribution, as will be shown later in the results and discussion section. This chapter describes our attempts to fully treat the condensation and to examine the influence of the condensation fully treated scheme on the drying behavior compared to the condensation partly treated scheme with convective heat transfer boundary condition at the network surface.

In this chapter, a non-isothermal two-dimensional pore network model which incorporates the relevant transport processes is developed to simulate the SSD of porous media. Although the present model is restricted to two space dimensions, the methodology proposed here is also applicable to the simulation of three-dimensional networks. First, the description of the model and the related numerical scheme are detailed. The validity of the model is qualitatively checked against the experimental observations with fair agreement. After that, the striking features of the present model compared to other published models are presented. Finally, several conclusions from this work are drawn.

3.2 Pore network model

In general, a porous medium is composed of a solid matrix and an interconnected void space. The latter comprises of large voids and constrictions. In this model, the complex void space of a porous medium is approximated by a network of cylindrical throats (with circular cross section), representing the constrictions, which are interconnected by spherical pores corresponding to the larger voids (c.f. Fig. 3.2). Each pore in the network is connected to four throats. Based on the amount of water inside a pore/throat, its state can

be either full, partially filled, or empty. A full or partially filled throat which connects two empty pores is referred to as a single liquid throat. The main assumptions made in the development of this pore network model are as follows: The solid phase is non-hygroscopic with a perfectly wetted surface. As mentioned in the work of Whitaker [13], during the drying process of capillary porous media, the convective heat transfer rate in the fluid phase is relatively low compared to the conductive heat transfer rate. There is a small temperature difference between the solid and fluid phases, and therefore, they are assumed to be in local thermal equilibrium. In the same spirit, the heat transfer is assumed to occur by conduction only. In the liquid phase, the capillary forces dominate the viscous and gravity forces. Despite these simplifications, the pore network model is still capable of giving salient features involved during the SSD drying process of a porous medium. In the next sections, the model components are presented in detail.

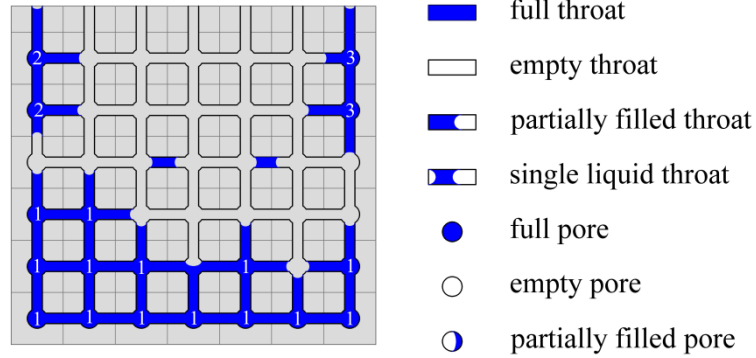


Figure 3.2: Sketch of a partially dried two-dimensional pore network (size of 7×7 pores) with three liquid clusters (including cluster labels) and two single liquid throats. Various possible fill states of pores and throats are illustrated.

3.2.1 Surface condensation and evaporation model

For the surface condensation and evaporation periods, we assume that the network is fully saturated with pure liquid water; therefore, the condensed liquid forms a thin film on the network surface [61]. At the interface between the free liquid water and pure water vapor, the equilibrium transfer rate from the liquid phase to the vapor phase or from the vapor phase to the liquid phase (evaporation or condensation, respectively) is given by the kinetic theory of gases [57]. In SSD, however, the phase change processes are fast and far from equilibrium. Therefore, the evaporation or condensation rates are calculated by the modified Hertz-Knudsen equation at the quasi-steady state,

$$\dot{m}_{con/evp} = \frac{2\delta_{evp}}{2 - \delta_{evp}} \sqrt{\frac{\tilde{M}_v}{2\pi\tilde{R}T_{surf}}} \left[P_{steam} - P_{sat}(T_{surf}) \right], \quad (3.1)$$

where δ_{evp} denotes the evaporation coefficient, which is determined from evaporation experiments. This evaporation coefficient δ_{evp} is a correction factor that accounts for

various effects, such as the reflection of liquid molecules or the replacement of vapor molecules, which lower the evaporation rate compared to that in vacuum [78]. The magnitude of the evaporation coefficient δ_{evp} for several substances is reported in the literature [79,80]. For water, the evaporation coefficient δ_{evp} varies between 0.01 and 1.00 [79] depending on the concentration of molecules on the gas side of the interface. p_{steam} denotes the superheated steam pressure, $p_{sat}(T_{surf})$ denotes the saturated vapor pressure at the surface temperature T_{surf} . \tilde{M}_v and \tilde{R} denote the molar mass of vapor and the universal gas constant, respectively. During the surface condensation period, $\dot{m}_{con/evp}$ has a positive value because the steam pressure is higher than the saturated pressure at the surface, and this implies condensation of vapor. When the surface temperature T_{surf} is higher than the saturation temperature for a given steam pressure, $T_{sat}(p_{steam})$, then $\dot{m}_{con/evp}$ becomes negative. At this point the surface evaporation period starts, during which the film water is removed from the surface.

During the surface condensation and evaporation periods, the network is heated by both sensible and latent heat. The heat transfer process between the superheated steam and the porous medium surface is determined by

$$\lambda_{eff} \frac{\partial T}{\partial z} = \alpha (T_{steam} - T_{surf}) - \dot{m}_{evp/con} \Delta h_{evp}, \quad (3.2)$$

where z denotes the vertical coordinate. The total gas-side heat transfer coefficient α includes both convective and radiative heat transfer

$$\alpha = \alpha_{conv} + \alpha_{rad}. \quad (3.3)$$

The convective heat transfer coefficient is a constant at the given drying conditions. This heat transfer coefficient may be obtained analytically by the boundary layer solution or correlated empirically to [81]

$$Nu = 0.664 Re^{\frac{1}{2}} Pr^{\frac{1}{3}}, \quad (3.4)$$

where $Nu = \frac{\alpha_{conv} L_{network}}{\lambda_v}$, $Re = \frac{u_{steam} L_{network}}{\nu_v}$ and $Pr = \frac{c_{p,v} \mu_v}{\lambda_v}$ are the dimensionless Nusselt,

Reynolds and Prandtl numbers, respectively. $L_{network}$ is the length of the network, and the physical and thermal properties of the vapor are determined from T_{steam} and p_{steam} . The radiative heat transfer coefficient depends on the temperature and it can be described by

$$\alpha_{rad} = \sigma_{rad} \varepsilon \frac{(T_{surf} + T_{steam})^3}{2}, \quad (3.5)$$

where $\sigma_{rad} = 5.67 \times 10^{-8} \text{ W/m}^2\text{K}^4$ denotes the Stefan-Boltzmann constant, and where ε denotes the thermal emissivity of the network, which is approximated by the thermal emissivity of the solid phase. The discretization in space and time for solving the heat transfer problem inside the pore network during these periods is discussed in the next section. The radiative heat transfer cannot be neglected at elevated drying temperature due to its significant contribution to the total heat transfer process. However, this heat transfer mechanism leads to a non-linear boundary condition at the porous medium surface, which can increase the computation time for the pore network simulation. Therefore, in this work the network size is restricted to 40×40 pores.

3.2.2 Network drying model

During the main drying period, the moisture is removed by evaporation that may occur at the network surface as well as inside the network. Since the real porous medium is neither homogeneous nor isotropic, the throat/pore size is not uniform but distributed in a certain size range according to a probability distribution such as the normal or Weibull distributions. Because of this non-uniform throat/pore radius distribution the liquid flows in the network due to capillary action. In the following subsections, we discuss individually the transport mechanisms for vapor, liquid and thermal energy.

a) Phase change rate at the liquid-vapor interface

The phase change rate at the liquid-vapor interface within the network is calculated by the Hertz-Knudsen equation. If the liquid-vapor interface is located inside a liquid throat (c.f. Fig. 3.3a), the evaporation/condensation rate is calculated as follows:

$$\dot{M}_{evp/con,ij} = \pi r_{t,ij}^2 \frac{2\delta_{evp}}{2 - \delta_{evp}} \sqrt{\frac{\tilde{M}_v}{2\pi\tilde{R}T_j}} \left(p_{sat}(T_j) - p_{v,i} \right). \quad (3.6)$$

The liquid temperature in single liquid throats (c.f. Fig. 3.3b) is computed by the average temperature at the two neighboring vapor pores. Evaporation occurs at both ends of the throat with the rate

$$\dot{M}_{evp/con,ij} = \pi r_{t,ij}^2 \frac{2\delta_{evp}}{2 - \delta_{evp}} \sqrt{\frac{\tilde{M}_v}{2\pi\tilde{R} \frac{T_i + T_j}{2}}} \left(p_{sat}\left(\frac{T_i + T_j}{2}\right) - p_{v,i} \right). \quad (3.7)$$

If the evaporation/condensation occurs at partially filled pores (c.f. Fig. 3.3c), the phase change rate is calculated using the maximal cross sectional area of pores:

$$\dot{M}_{evp/con,i} = \pi r_{p,i}^2 \frac{2\delta_{evp}}{2 - \delta_{evp}} \sqrt{\frac{\tilde{M}_v}{2\pi\tilde{R}T_i}} \left(p_{sat}(T_i) - p_{v,i} \right). \quad (3.8)$$

Note that in Eqs. 3.6-3.8, if the liquid temperature is larger than the boiling temperature at vapor pressure, then evaporation occurs and $\dot{M}_{evp/con}$ has a positive sign. Conversely, if the liquid temperature is lower than the boiling temperature at vapor pressure, then condensation takes place and $\dot{M}_{evp/con}$ has a negative value.

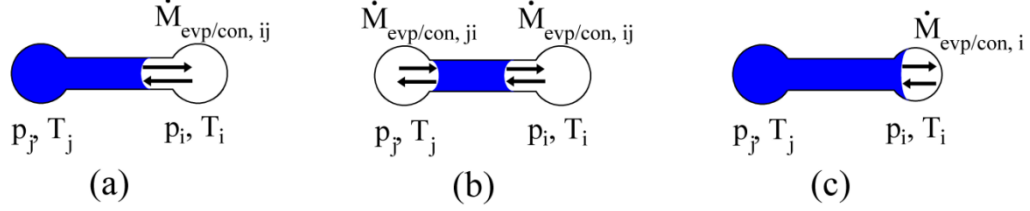


Figure 3.3: Phase change in a partially filled throat (a), in a single liquid throat (b) and in a partially filled pore (c). The arrows indicate the direction of vapor flow.

b) Vapor transport

In pore network models for hot air drying, the vapor transport is often determined from the solution of an auxiliary diffusion equation for the binary mixture of vapor and dry air in the gas phase. For superheated steam drying, however, we assume that there is no air in the drying agent. Thus, the Hagen-Poiseuille law is applied [21]:

$$\dot{M}_{v,ij} = \frac{\pi r_{t,ij}^4}{8\nu_v L_t} (p_i - p_j), \quad (3.9)$$

where $\dot{M}_{v,ij}$ denotes the vapor mass flow rate through the throat connecting the pores i and j , ν_v denotes the vapor kinematic viscosity, and p_i and p_j denote the vapor pressure at pores i and j , respectively. L_t and r_t denote the throat length and radius, respectively.

The mass balance equation for the vapor is written in each empty or partially filled pore as

$$\sum_j \dot{M}_{v,ij} - \sum_j \pi r_{t,ij}^2 \dot{m}_{evp/con,ji} - \pi r_{p,i}^2 \dot{m}_{evp/con,i} = 0. \quad (3.10)$$

c) Liquid transport and pore-scale events

Because of the non-uniform pore size distribution, the liquid flow is driven by capillary action and large pores/throats are preferentially emptied or filled. Hence, the invading vapor phase may separate the liquid phase into several disconnected regions (c.f. Fig. 3.2). The liquid mass balance must be satisfied in the entire network as well as for each liquid region, the so-called liquid clusters. In this drying algorithm, we consider only liquid clusters which are comprised of non-empty throats connected by non-empty pores, and the vapor phase is assumed to be continuous. The liquid hydraulic conductance in the liquid

clusters formed during the drying process provides essential information for the calculation of the liquid transport. The Hoshen–Kopelman algorithm [82,83] is applied for labelling the liquid clusters.

The difference between the liquid pressure p_l and the vapor pressure p_v at the liquid-vapor interface of a partially filled pore/throat (c.f. Fig. 3.3) is described by the Young-Laplace equation

$$p_l = p_v - \frac{2\sigma(T)\cos\theta}{r_{p/t}}, \quad (3.11)$$

where σ and θ denote the surface tension and the equilibrium contact angle, respectively. $r_{p/t}$ denotes the radius of the meniscus pore/throat and the temperature T of each throat is taken as the mean temperature at its two neighboring pores. In this work, the equilibrium contact angle is assumed to be zero (i.e. perfect wetting). An empirical equation is used for the dependence of the surface tension on the temperature – namely Eq. 3.18. The capillary action divides the liquid into clusters in order to minimize the liquid pressure; therefore, in each cluster, the meniscus pore/throat which has the highest liquid pressure according to Eq. 3.11 will be the moving meniscus pore/throat in each time step.

As discussed in Sec. 3.1, in published pore network models for hot air drying, the pore condensation was only partly treated because the condensed liquid is discarded when the meniscus throats are fully filled [46,74–77]. In the present model, several pore-scale events are introduced to remedy this shortcoming. By coupling the available emptying and refilling events with new invasion events of liquid into empty pores/throats, the pore condensation is fully accounted for. These discrete events at the pore-scale are presented in Figs. 3.4 and 3.5.

The time steps for the emptying and refilling events of meniscus pores or throats (Fig. 3.4) are computed by

$$\Delta t_{empty, cn/st, p/t} = \frac{V_{p/t}\rho_l(T)S_{p/t}}{\sum_{cn/st} \dot{M}_{evp/con}}, \quad (3.12)$$

and

$$\Delta t_{refill, cn/st, p/t} = -\frac{V_{p/t}\rho_l(T)(1-S_{p/t})}{\sum_{cn/st} \dot{M}_{evp/con}}, \quad (3.13)$$

where cn and st denote the label of a liquid cluster and the index of a single liquid throat, respectively.

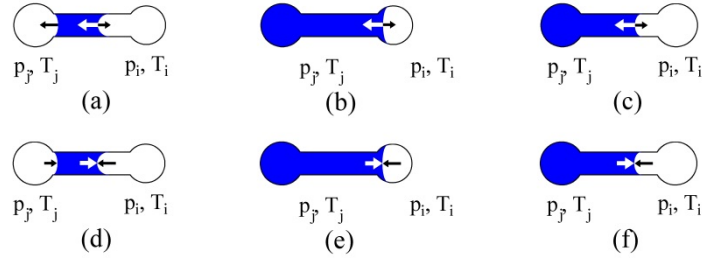


Figure 3.4: Pictorial representation of (a-c) emptying and (d-f) refilling events. The black and white arrows indicate the vapor and liquid flow directions, respectively.

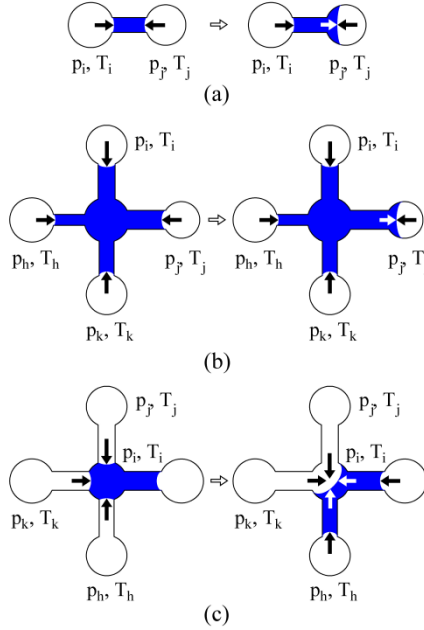


Figure 3.5: Pictorial representation of liquid invasion events. The black and white arrows indicate the vapor and liquid flow, respectively. The figures on the left show the liquid distribution before the invasion, whereas the figures on the right show the liquid distribution after the invasion.

Due to capillary action, the condensed liquid at full meniscus pores/throats may invade their neighboring empty throats/pores. As presented in Fig. 3.5, three liquid invasion rules are formulated in the present model: (i) liquid invasion from a full single liquid throat into its neighboring empty pores (c.f. Fig 3.5a), (ii) liquid invasion from a full liquid throat in a liquid cluster into its neighboring empty pore (c.f. Fig 3.5b), and (iii) liquid invasion from a full pore in a liquid cluster into its neighboring empty throats (capillary re-equilibration event) (c.f. Fig. 3.5c). By comparing the entrance capillary threshold pressures of these neighboring pores/throats, the condensed liquid invades the neighboring empty pores/throats with the lowest liquid pressure, as computed by Eq. 3.11. The time step for the first two liquid invasion events (Fig. 3.5a-b) is calculated by

$$\Delta t_{invasion,cn/st} = -\frac{V_{p/t} \rho_l (T)}{\sum_{cn/st} \dot{M}_{evp/con}}. \quad (3.14)$$

The pore/throat saturations after the capillary re-equilibration event (Fig. 3.5c) are computed by

$$S_{t,ih} = 1 \text{ and } S_{p,h} = \frac{V_{p,h} - V_{t,ih}}{V_{p,h}}. \quad (3.15)$$

d) Implicit time-stepping for dynamic heat transfer

To compute the temperature field during the drying process, a discretization of the thermal energy balance equation is presented in this section. Firstly, the heat flux \dot{Q}_{ij} between two pores is calculated based on Fourier's law

$$\dot{Q}_{ij} = A_{cv,ij} \lambda_{eff,ij} \frac{T_i - T_j}{L}, \quad (3.16)$$

where $A_{cv,ij}$ denotes the heat transfer area and where $\lambda_{eff,ij}$ denotes the effective thermal conductivity between pores i and j . In a 2D Cartesian pore network, the heat transfer area is calculated as $A_{cv,ij} = WL$ (see Fig. 3.6).

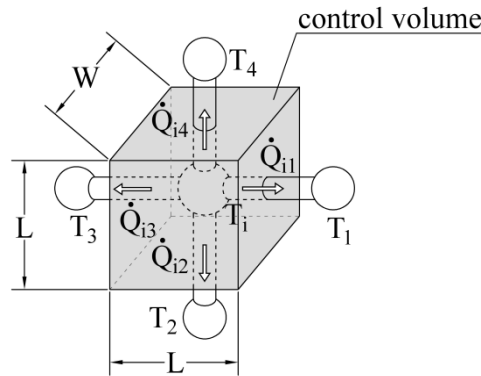


Figure 3.6: Heat balance at vapor pore i . The white arrows indicate the direction of the heat flux through each face of the control volume.

The heat flow rates \dot{Q}_{ij} from neighboring pores j to pore i lead to a change of the enthalpy in the control volume i since they cause an increase in temperature as well as a phase change (evaporation or condensation). The discrete dynamic equation for the thermal energy balance at pore i in time step Δt is given by

$$\frac{\rho_{eff,i} c_{eff,i} V_i}{\Delta t} (T_{i,t+\Delta t} - T_{i,t}) + \Delta h_{evp} \sum_j \dot{M}_{evp/con,ij} = \sum_j -A_{cv,ij} \lambda_{eff,ij} \frac{T_{i,t+\Delta t} - T_{j,t+\Delta t}}{L}, \quad (3.17)$$

where $V_i = WL^2$ is the volume of the control element i . This equation yields an implicit time-stepping scheme for updating the temperature field.

e) Boundary conditions and thermo-physical properties

The effective parameters, mass density $\rho_{eff,i}$, specific heat capacity $c_{eff,i}$ and thermal conductivity $\lambda_{eff,ij}$ required in Eqs. 3.15 and 3.16 are calculated according to the equations presented in Table 3.1.

Table 3.1: The effective thermo-physical properties of the network [74].

Property	Equation
Density	$\rho_{eff,i} = \frac{V_{s,i}\rho_s + V_{l,i}\rho_l + V_{v,i}\rho_v}{V_i}$
Specific heat capacity	$c_{eff,i} = \frac{V_{s,i}\rho_s c_s + V_{l,i}\rho_l c_l + V_{v,i}\rho_v c_v}{\rho_{eff,i} V_i}$
Thermal conductivity	$\lambda_{eff,ij} = \frac{(A_{cv,ij} - \pi r_{i,ij}^2) \lambda_s + \pi r_{i,ij}^2 [S_{ij} \lambda_l + (1 - S_{ij}) \lambda_v]}{A_{cv,ij}}$

Because of the dependence of the liquid and steam thermo-physical properties on temperature and pressure, these properties, which are needed to compute the fluid and energy transport, are temporarily and locally updated for each pore according to the equation of state for pure water [48]. For example, the surface tension of pure water [84] is given as a function of temperature by

$$\sigma = 0.2358 \left[\frac{T_c - T}{T_c + 273.15} \right]^{1.256} \left[1 - 0.625 \left(\frac{T_c - T}{T_c + 273.15} \right) \right], \quad (3.18)$$

where $T_c = 374$ °C is the critical temperature of water.

The heat transfer boundary condition at the surface was given in Eq. 3.2. According to Messai et al. [65] and Hager et al. [63], the mass transfer coefficient at the network surface is extremely large; therefore, the vapor pressure at the surface pores is assumed to be equal to the steam pressure during the main drying period. Perfect thermal insulation is assumed at the bottom of the network. Due to the high computational cost, the simulations presented here are conducted for a small network. To relax this limitation, periodic boundary conditions are imposed on the lateral sides of the network, which allows for more space for the liquid capillary transport.

f) Numerical algorithm

To solve the mass and thermal energy transport problem presented in the previous sections, a numerical methodology is developed as follows (steps 2-4 correspond to the surface condensation and evaporation periods, and steps 5-9 correspond to the main drying period):

Step 1: Generate the data structure; impose initial conditions such as initial temperature and liquid saturation, as well as boundary conditions.

Step 2: Calculate the phase transition rate and the effective heat transfer coefficient at the network surface by Eqs. 3.1 and 3.2.

Step 3: Compute the temperature distribution with the thermal time step Δt_{temp} by solving the system of equations obtained from Eq. 3.17. Although the temperature field solved by an implicit scheme as in Eq. 3.17 is unconditionally stable, a large time step Δt_{temp} may lead to inaccuracies such as local fluctuations of the temperature profile. A numerical test for Δt_{temp} between 10 s and 0.001 s indicated that for a time step smaller than 0.01 s the results do not differ significantly anymore. Therefore, the thermal time step $\Delta t_{temp} = 0.01$ s was chosen for all simulations presented in this study.

Step 4: Compute the mass of condensed liquid at the network surface, $M_{con,surf}$, by

$$M_{con,surf} \Big|_{t+\Delta t_{temp}} = M_{con,surf} \Big|_t + \sum_i LW \dot{m}_{con/evp} \Delta t_{temp}, \quad (3.19)$$

(where i denotes the surface pore) and reiterate from step 2 until $M_{con,surf}$ reaches zero (end of the surface condensation and evaporation periods).

Step 5: Compute the phase transition rate in the meniscus pores/throats by Eqs. 3.6-3.8.

Step 6: Update the vapor pressure field by solving the system of mass balance equations (Eq. 3.10).

Step 7: Check for and carry out the capillary re-equilibration events (Eq. 3.15). Calculate the time steps for emptying, refilling, and other liquid invasion events, Eqs. 3.12-3.14; compare these time steps with the current Δt_{temp} and choose the minimum Δt_{min} as the next time step.

Step 8: Update the temperature field by solving Eq. 3.17 with time step size Δt_{min} .

Step 9: Update the liquid phase distribution and the network saturation with time step size Δt_{min} , and label the liquid clusters. Reiterate from step 5 until the network is completely dried.

This numerical methodology is summarized in Fig. 3.7.

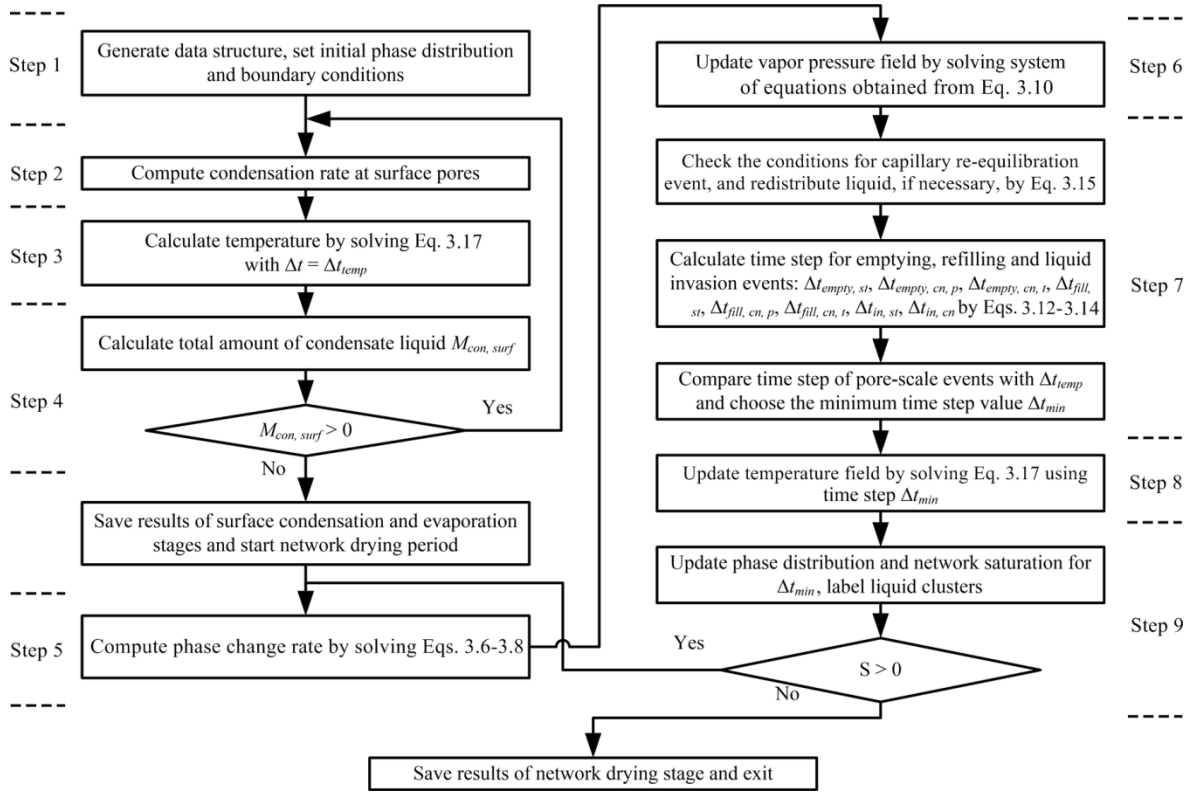


Figure 3.7: The numerical algorithm used to simulate the superheated steam drying process.

3.3 Results and discussion

Simulations were performed for both the “Condensation Partly Treated” (CPT) scheme without liquid invasion rules and for the “Condensation Fully Treated” (CFT) scheme with additional liquid invasion rules (corresponding to Fig. 3.5 and Eqs. 3.14 and 3.15). A 40×40 pore network with uniform throat length $L = 1000 \mu\text{m}$ was used in these simulations. The pore and throat radii were sampled from normal distributions with mean radii of $r_p = 250 \mu\text{m}$ and of $r_t = 100 \mu\text{m}$, respectively, and standard deviations of $\sigma_p = \sigma_t = 10 \mu\text{m}$. Other parameters used in the pore network simulations are presented in Table 3.2. With these input parameters, the simulations are performed by running a Matlab code on a PC with a single CPU (Core i7, 3.4 GHz) and with 16 GB RAM. It takes between 25 and 28 hours to complete one simulation with the CFT scheme.

3.3.1 Qualitative model validation

Due to the complex void structure of a real porous medium and the lack of information about the pore size distribution and throat lengths needed to generate a pore network, the simulated drying characteristics cannot be fully validated by experimental data from the literature. To check the validity of the present model, the simulation results are compared qualitatively with experimental data extracted from Hager et al. [63].

Table 3.2: Parameters used in the simulations.

Parameter	Value
Initial liquid mass $M_{w,0}$	1.46×10^{-4} kg
Thermal conductivity of the solid phase λ_s	13 W/mK
Mass density of the solid phase ρ_s	5060 kg/m ³
Specific heat capacity of solid phase c_s	435 J/kgK
Thermal emissivity of solid phase ε	0.9
Initial network temperature T_0	80 °C
Steam temperature T_{steam}	200 °C, 250 °C
Steam pressure p_{steam}	1 bar
Steam velocity u_{steam}	5 m/s
Evaporation coefficient δ_{evp}	0.01

The experiment described there was conducted with porous ceramic spheres. The normalized drying rate and saturation, respectively, are computed by

$$f = \frac{\dot{M}_{drying}}{\dot{M}_{drying,CDR}} \quad \text{and} \quad S_n = \frac{S - S_{eq}}{S_{cr} - S_{eq}}, \quad (3.20)$$

where $\dot{M}_{drying,CDR}$ denotes the average drying rate during the quasi-constant drying rate (CDR) stage and where S_{cr} denotes the network saturation at the transition point between the CDR and the falling drying rate (FDR) stages.

To eliminate the influence of the random pore sizes on the drying behavior, the simulation results are generated by performing a series of 10 different realizations in a Monte-Carlo approach. Since the surface condensation period is invisible in the experimental data (the moisture content decreases immediately when the drying process starts), the simulations are performed starting at saturation temperature in this section. The qualitative agreement between the numerical and experimental results illustrated in Fig. 3.8 indicates the theoretical predictive ability of the model developed in this study.

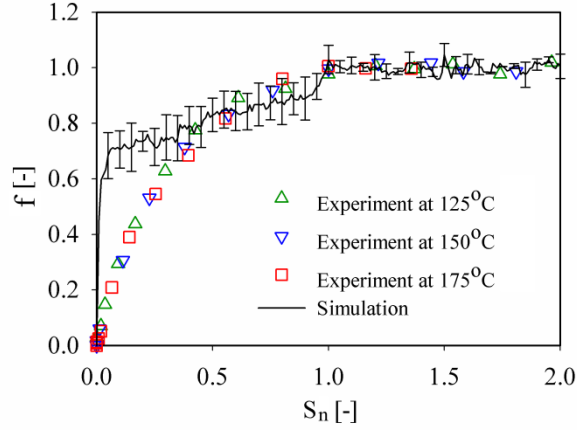


Figure 3.8: Normalized numerical and experimental drying characteristics. The experimental data is extracted from Hager et al. [63].

The difference between the numerical and experimental curves towards the end of the drying process may stem from the assumption of a non-hygroscopic solid phase in this model, from the changing evaporation area or from the difference in porous structure as well. The equilibrium moisture content X_{eq} that remained in the experimental sample was 0.013 kg water/kg dry solid, 0.007 kg water/kg dry solid and 0.006 kg water/kg dry solid at drying temperatures 125°C, 150°C and 175°C [85], respectively. In the numerical results, the equilibrium moisture content X_{eq} equals zero for all drying conditions. Due to the absence of bound water in the simulation, the drying rate towards the end of the process is expected to be higher than in the experiment. Additionally, when the drying front retreats into the ceramic sample; the evaporation area decreases because of the spherical geometry of the ceramic particle. Considering the flat computational medium, the evaporation area may vary but not in a significant range during the network drying period. Furthermore, the difference in pore radius and length distribution, in porosity and in coordination number between real ceramic sample and the pore network configuration may lead to deviations. The sample pore radius was mainly distributed in a range between 1 μm and 1 nm, in which the liquid viscous effect influences the drying behavior. As investigated in [86], the drying rate obtained by introducing the liquid viscous effect is reduced faster than without the liquid viscous effect. The value of effective thermal conductivity $\lambda_{eff,ij}$ obtained from the parallel combination of resistances used in the model (c.f. Table 3.1) also is higher than in reality; the numerical drying process may therefore be faster than the experiment. With the combination of these aforementioned effects, the measured drying rate is expected to drop faster compared to the numerical results.

3.3.2 Impact of liquid invasion events on the temperature and moisture content evolution

Since the position of pores and throats with different radii varies over different realizations, drying characteristics such as the transition point between the CDR stage and the FDR stage vary in a large range (between 0.43 and 0.93 of network saturation in the aforementioned 10 realizations). Therefore, to investigate the influence of pore-scale discrete events on the drying behavior, typical simulation results obtained from realization No. 4 with $T_0 = 80^\circ\text{C}$ will be discussed throughout this section. The evolution of the moisture content and of the average temperature over time for both the CFT and the CPT schemes with $T_{steam} = 200^\circ\text{C}$ are presented in Fig. 3.9.

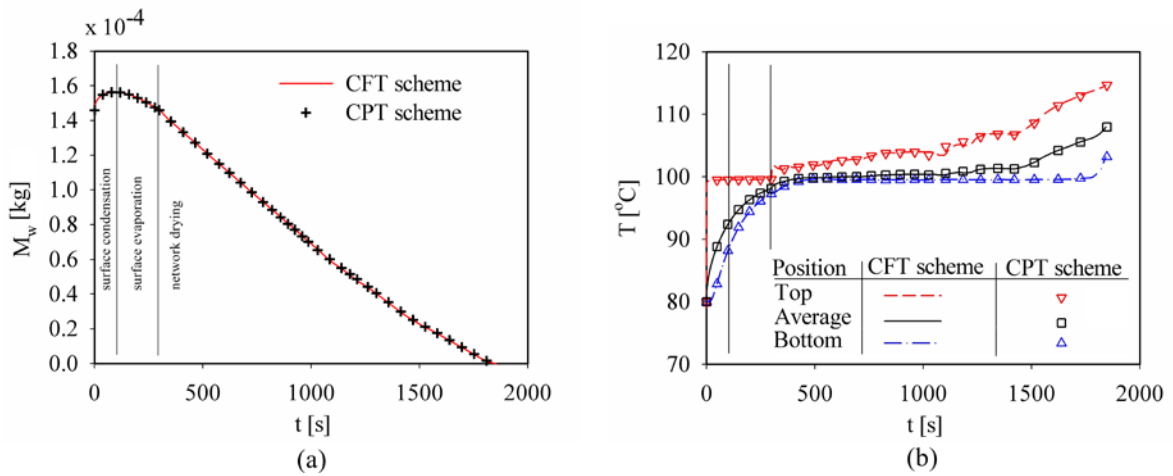


Figure 3.9: The evolution of moisture mass (a) and temperature (b) over time during the drying process obtained by the “Condensation Fully Treated” (CFT) and by the “Condensation Partly Treated” (CPT) schemes. The vertical lines in (b) separate the periods of the drying process as shown in (a).

The surface condensation and evaporation periods are indicated in Fig. 3.9a. During the surface condensation period, the moisture mass M_w in the network increases over time, starting from the initial moisture content $M_{w,0}$, because of vapor condensation. This also heats up the network by releasing latent heat, and therefore, the network surface temperature increases very rapidly in the beginning of the drying process, when the condensation is very strong. The network surface temperature therefore approaches the saturation temperature very quickly. However, when the network surface temperature is close to the saturation temperature, it increases very slowly because of the low condensation rate (c.f. Eq. 3.1) and the large heat flux into the network with a pronounced temperature gradient build-up at the beginning of the drying process.

At 93 s, the network surface temperature has almost reached the saturation temperature (or boiling temperature) $T_{sat}(p_{steam})$ and the surface evaporation period commences. At this

time, the moisture content M_w attains its maximum value, and we find that the mass of additional liquid generated during the condensation period is 1.1×10^{-5} kg (approximately 7% of $M_{w,0}$). It should be noted that in SSD the surface condensation heats the network surface up to the boiling temperature, whereas in hot air drying, the surface is heated up to the wet bulb temperature. The rate of increase of the network surface temperature during the surface evaporation period is lower than during the surface condensation period because the thermal energy supplied to the network is used for both vaporization and sensible heating processes. At $t = 299$ s, the liquid film at the network surface is completely evaporated, and the internal moisture starts to evaporate (beginning of the main drying period). During the first two drying periods, the results obtained from both CPT and CFT are identical, because the network surface remains fully saturated and liquid invasion events do not occur.

During the main drying period, the moisture inside the network is removed. Firstly, the throats near the network surface empty; the impact of the latent heat of evaporation on the heat transfer process (see Eq. 3.2) at the network surface is decreasing simultaneously. Thus, a significant increase of the network surface temperature over time is observed. The network bottom temperature also increases over time, but more slowly than the surface temperature, due to the thermal resistance of the network. Since the temperature at the evaporation front is almost equal to the saturation temperature $T_{sat}(p_{steam})$, the network bottom temperature eventually reaches this saturation temperature and then stays constant. Towards the end of the drying process, when the vapor phase reaches the bottom edge of the network, the limitation by $T_{sat}(p_{steam})$ is no longer valid and the bottom temperature starts to increase again. Overall, the bottom temperature increases from the initial temperature, saturates at the $T_{sat}(p_{steam})$ until the drying process has almost finished, and then approaches the temperature of the drying agent. This evolution of the bottom temperature over time is in agreement with available experimental observations [87]. These characteristics of the drying process were reproduced by simulations in which the condensation was treated either partly or fully. Only small differences in the moisture content and temperature profile (mainly in the surface temperature) are obtained from these two schemes. The drying times obtained with the CFT and CPT schemes are 1853 s and 1858 s, respectively. Though this difference is very small, the slightly longer drying time obtained by the CPT scheme compared to the CFT scheme can be explained by the fact that the liquid invasion events may connect individual small liquid clusters to form bigger liquid clusters. The CFT scheme therefore yields a better hydraulic connectivity within the network, which enhances the capillary pumping effect to deliver liquid towards the network surface. As a result the hydraulic resistance of vapor transport decreases and the drying rate is enhanced at the same time. Note that although the condensed liquid accumulated with the CFT scheme is higher than with the CPT scheme (the difference is

0.31% $M_{w,0}$, see *next section* for details), the drying time obtained with the CFT scheme is shorter due to a better liquid hydraulic connectivity or a longer CDR stage. It is also worth noting that since the liquid invasion rules (Step 7) are not considered in the CPT scheme, the computing time for the CPT scheme (14 to 16 hours) is significantly shorter than for the CFT scheme (25 to 28 hours). Therefore, if only the temperature and moisture content evolutions are considered, then the CPT scheme with lower computational cost may be used to perform the simulations instead of the CFT scheme, since the difference in the results is very small. If, however, other drying characteristics, such as the phase distribution, are of interest, then the more expensive CFT scheme should be used since it can achieve more accurate results, as will be discussed in the following section.

3.3.3 Impact of liquid invasion rules on condensed liquid treatment and phase distribution

Figure 3.10a indicates the actual condensation rate obtained with the CFT scheme as well as the condensation neglected in the CPT scheme. The neglected condensation rate corresponds to the discarded condensing vapor due to the absence of liquid invasion events. The ratio between the neglected condensation and actual condensation rates is presented in Fig. 3.10b. At the beginning of the main drying period the liquid phase is continuous and evaporation dominates condensation. The liquid cluster is evaporating such that only emptying events (c.f. Fig. 3.4a-c) occur. Therefore, the condensation is completely accounted for by both the CFT and the CPT schemes.

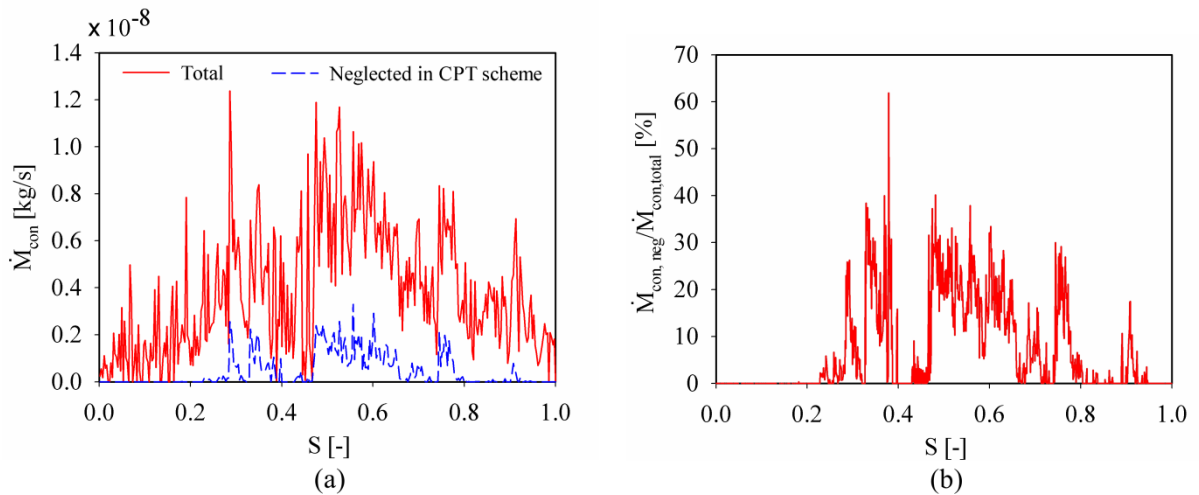


Figure 3.10: The absolute computed condensation rates (a) and their relative ratio in percent (b) vs. the network saturation during the network drying period.

During the course of drying the liquid phase separates into clusters of different sizes, and some of these clusters become condensing clusters, in which both refilling and liquid invasion events occur. Without the liquid invasion rules, once the meniscus pores/throats of condensing clusters are full, any further condensation is neglected if the CPT scheme is

used. As illustrated in Fig. 3.10b, the relative amount of neglected condensation reaches more than 50% at $S = 0.38$. Towards the end of the drying process, when the liquid clusters have been heated long enough, all of them become evaporating clusters. The liquid invasion and refilling events cease to exist, and the neglected condensation rate by the CPT scheme drops to zero.

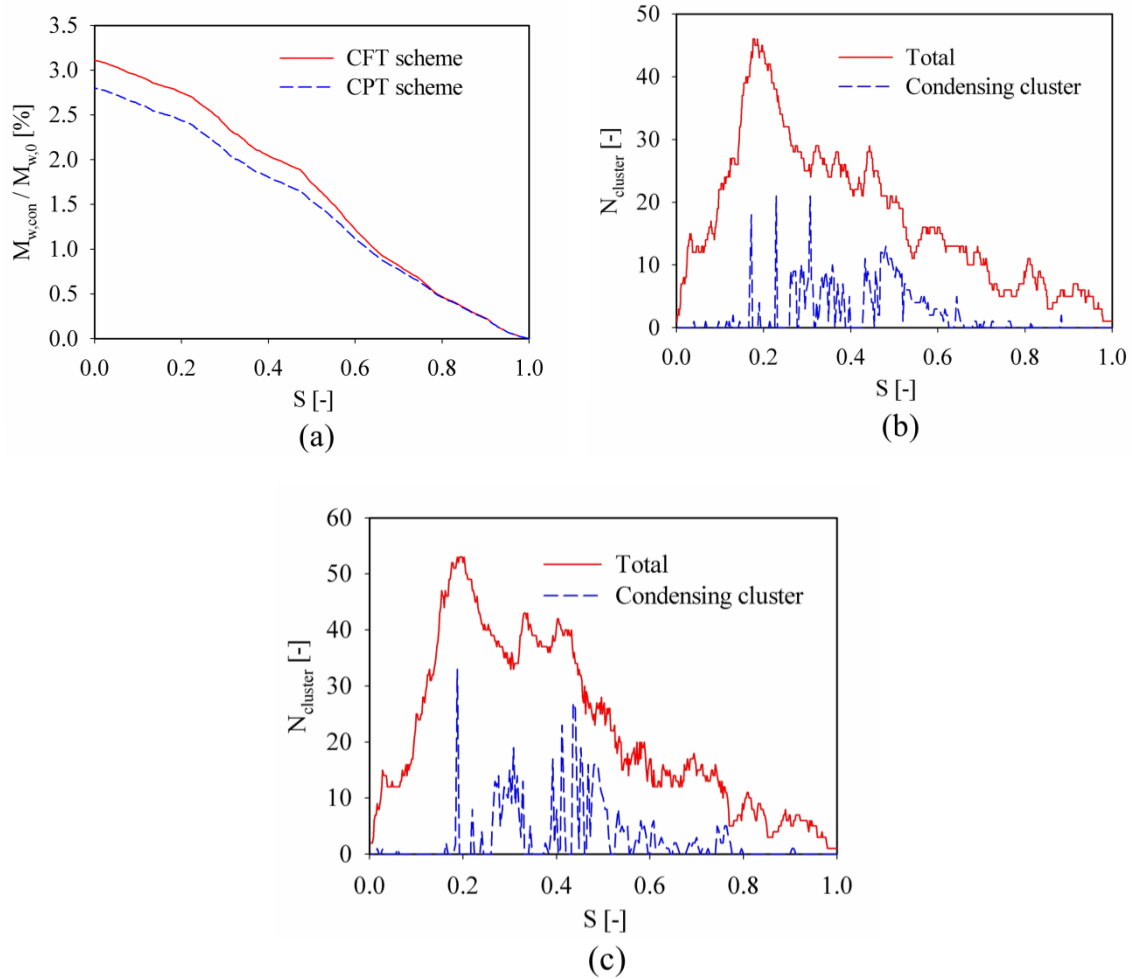


Figure 3.11: Relative amount of condensed water (a) and number of liquid clusters vs. network saturation obtained with the CPT scheme (b) and with the CFT scheme (c) during the network drying period.

The condensed liquid mass $M_{w,con}$ within the network and the number of condensing liquid clusters are presented in Fig. 3.11. It shows that the total condensed liquid mass $M_{w,con}$ treated in the CFT scheme increases during the network drying period and reaches approximately 3.11% of the moisture mass of a fully saturated network, $M_{w,0}$. The amount of condensed liquid $M_{w,con}$ accommodated with the CPT scheme reaches only 2.80% of $M_{w,0}$. In other words, 90% of the condensed liquid mass $M_{w,con}$ are treated by the refilling rules (c.f. Eq. 3.13), whereas 10% of $M_{w,con}$ are accommodated by the liquid invasion rules (c.f. Eqs. 3.14 and 3.15). Although the additional mass of condensed liquid treated by introducing the liquid invasion rules is only about 10% of the total condensed liquid mass,

it helps to satisfy the heat and mass conservation during the drying process. Furthermore, the number of clusters obtained with the CFT and CPT schemes is presented in Fig. 3.11b-c. Due to the liquid invasion rules in the CFT scheme liquid clusters may be created from single liquid throats, and thus the number of clusters is larger than for the CPT scheme. Additionally, Fig. 3.11b-c also shows the number of condensing liquid clusters obtained with these schemes. At several saturation values, the condensing liquid clusters make up more than 50% of all liquid clusters. This implies that the complete modeling of vapor condensation in the CFT scheme helps to improve the accuracy of the liquid transport during the main drying period.

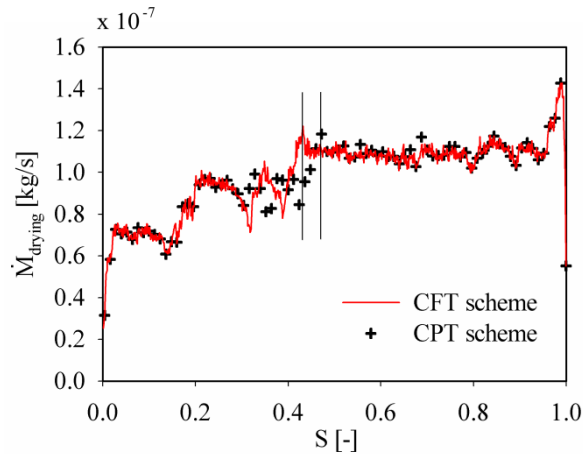


Figure 3.12: Drying rate curve obtained by the CFT and CPT schemes (vertical lines denote the transition points between the CDR and FDR stages for each scheme).

The drying kinetics of the SSD process obtained by both the CPT and the CFT schemes are presented in Fig. 3.12. During the CDR stage, the network saturation decreases almost linearly in time with a high drying rate. Although the evaporation occurs in the liquid meniscus throats at the network surface, the small throats are still full due to their high capillary threshold pressure and the liquid is pumped from the large throats into these small throats to offset the amount of evaporated liquid. These full surface throats keep the network surface sufficiently wet such that the drying rate stabilizes at a high value. Over time, the surface dries out, the evaporation front recedes into the network and the drying process enters the FDR stage. The transition point between the CDR and FDR stages is the saturation at which the network surface is completely dry (c.f. Fig. 3.12 where the transition occurs at $S = 0.43$ and $S = 0.46$ for the CFT and CPT schemes, respectively).

As discussed previously, the reason for the longer duration of the CDR stage obtained with the CFT scheme compared to the CPT scheme stems from a better hydraulic connectivity of the liquid phase due to the liquid invasion rules. The liquid is pumped more easily under the capillary action from the bottom of the network to its surface. Therefore, the network surface remains wet for a longer time if the CFT scheme is used. After the transition point,

the drying rate decreases over time due to an increase of the hydraulic resistance for the vapor transport during the FDR stage. During the CDR and FDR stages, an oscillation of the drying rate is observed. This oscillating behavior is attributed to the disintegration of the liquid phase into discrete liquid clusters of different sizes and to the recession and disappearance of liquid clusters. For instance, if a liquid cluster evaporates completely, then the vapor transport resistance decreases due to an extension of the available transport space, and thus a local increase of the vapor mass flow rate is observed.

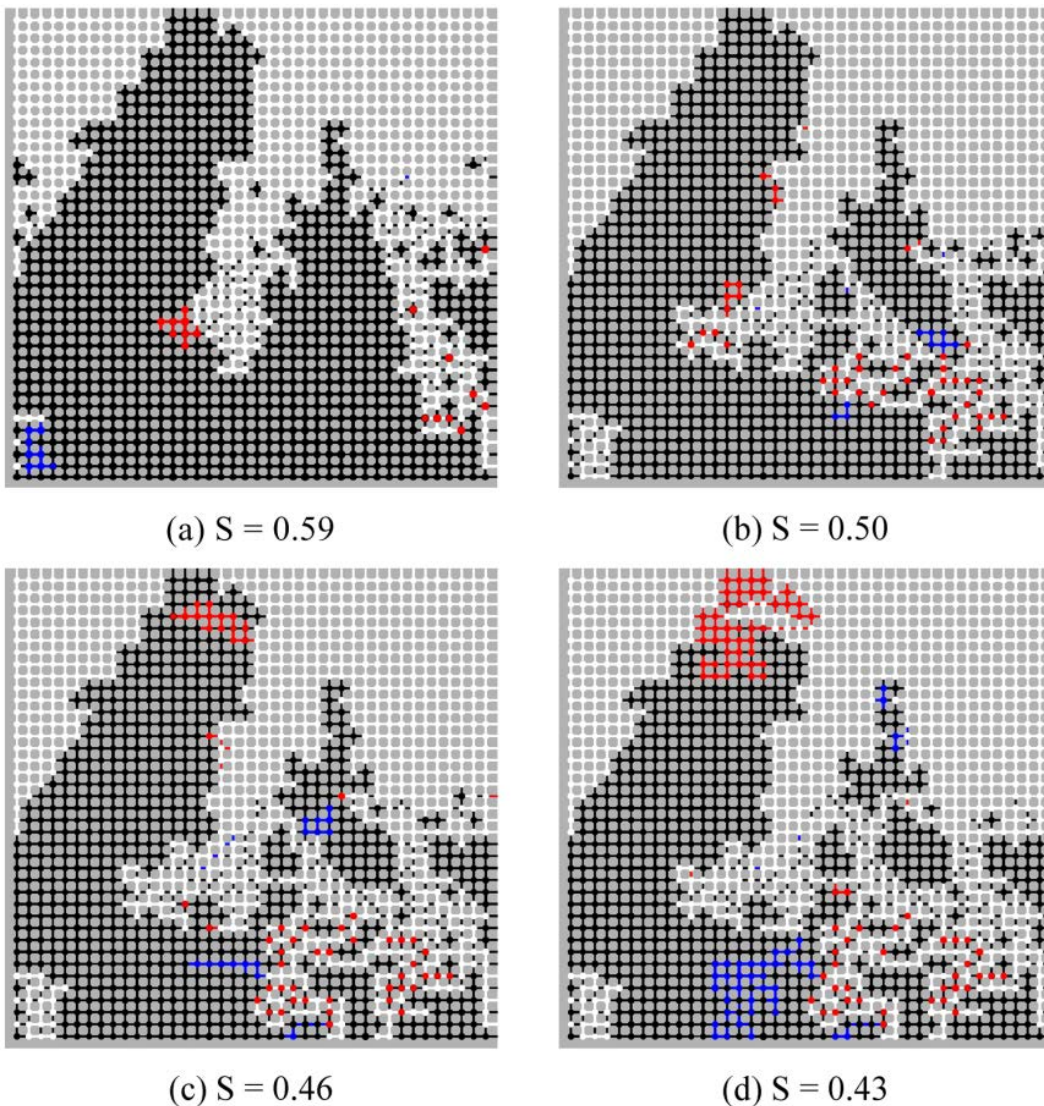


Figure 3.13: Phase distribution during SSD obtained by the condensation fully treated (CFT) and by the condensation partly treated (CPT) schemes. Saturated pores/throats obtained by both the CFT and the CPT schemes (black), only by the CFT scheme (red) and only by the CPT scheme (blue).

The refilling of empty pores/throats by the liquid invasion rules in the CFT scheme leads to a difference in vapor transport paths and in hydraulic connectivity of the liquid phase compared to the CPT scheme. As a result, the liquid distributions obtained by the CPT and

CFT schemes (see Fig. 3.13) are different. For instance, at the network saturation $S = 0.59$ (c.f. Fig. 3.12a), the vapor phase reaches the bottom edge of the network with the CFT scheme (the so-called breakthrough point), whereas this breakthrough point occurs later in the CPT scheme (at $S = 0.57$). This difference stems from the re-saturation of empty pores/throats due to the liquid invasion events in the CFT scheme. These refilled pores/throats block the vapor flow, which leads to a lower flow rate; simultaneously, a more pronounced vapor gradient builds up in the CFT scheme than in the CPT scheme. Regarding Eq. 3.10, a higher liquid pressure is obtained near the bottom of the vapor region in the CFT scheme due to a higher vapor pressure. The meniscus throats/pores located near the network bottom are more favorable to be emptied due to capillary action in the CFT scheme than in the CPT scheme. At a network saturation of $S = 0.46$ (c.f. Fig. 3.13c) the main liquid cluster is disconnected from the network surface in the phase distribution obtained with the CPT scheme, and the drying rate therefore commences to fall (FDR stage). At this same saturation, the drying rate obtained with the CFT scheme is still in the CDR stage, however. At a network saturation of $S = 0.43$ the phase distribution at the transition point between the CDR and FDR stages obtained by the CFT scheme is shown in Fig. 3.13d. Additionally, the phase distribution at the network saturation $S = 0.5$ is shown in Fig. 3.13b. As can be seen, the introduction of liquid invasion rules influences significantly the liquid phase disintegration.

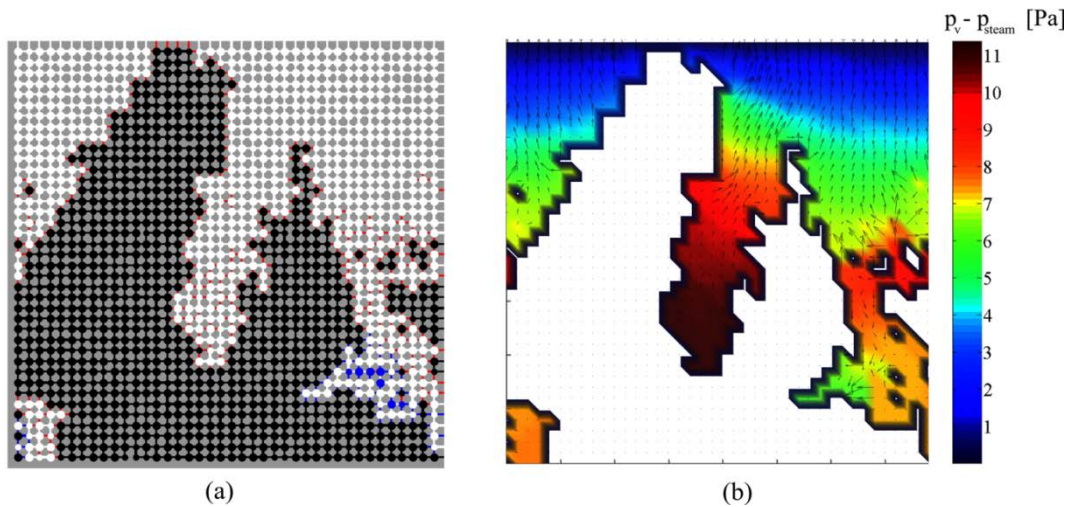


Figure 3.14: Liquid phase distribution (a) and vapor pressure field supplemented with vapor velocity (b) at network saturation $S = 0.60$. The evaporating and condensing throats/pores are shown in red and blue, respectively.

Since the vapor is transported by the convection mechanism, the vapor pressure difference is the driving force of vapor motion. In the present pore network model, with either CFT or CPT scheme, the overpressure of the vapor phase within a heterogeneous pore structure can be reproduced. The vapor pressure field and the phase distribution at network saturation $S = 0.60$ obtained by the CFT scheme are presented in Fig. 3.14.

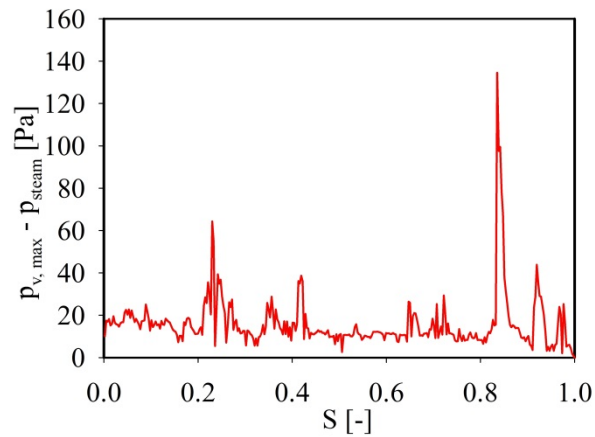


Figure 3.15: Vapor overpressure vs. network saturation during SSD.

Most condensing throats/pores are located below the evaporating throats/pores. This can be explained by a temperature gradient from the surface to the bottom of the network. Under capillary action, several vapor fingers appear at the evaporation front. The temperature at lower meniscus throats/pores may be lower than the saturation temperature, whereas the temperature at the upper meniscus throats is higher. Therefore, evaporation occurs at the upper meniscus throats and condensation occurs deeper inside the network. In other words, the vapor generated at evaporating throats flows into the network and condenses there. According to the vapor pressure distribution, the largest vapor pressure is not located at the lowest position of the vapor phase, which may lead to a local downward vapor flow (c.f. lower right part of Fig. 3.14b). This observation is contrary to the traditional understanding which is based on volume-averaged continuum simulations of the SSD process. These continuum-scale models deal with a homogeneous porous medium; therefore internal condensation cannot be observed. The maximum value of the vapor overpressure during the network drying period is presented in Fig. 3.15. It can be seen that the maximum overpressure is about 130 Pa which is very small compared to the available measured values for the SSD process in the context of wood drying [88]; this is due to the large throat radii and small network size used in the present paper. In the future, liquid viscosity should be introduced into this pore network model to quantify the overpressure within fine-textured porous materials such as wood.

CHAPTER 4

Continuum-scale modeling of the superheated steam drying process in a single wood particle and its reduction to a lump model

This chapter is a modified version of the paper *Superheated steam drying of single wood particles: A characteristic drying curve model deduced from continuum model simulations and assessed by experiments* submitted to *Drying Technology*. In this paper, the experiments were performed by Dr.-Ing. Neli Hampel in the frame of IGF Project No. 18971 BR/1 funded by Forschungs-Gesellschaft Verfahrens-Technik.

4.1 Literature review

Wood can be encountered in both daily life and industrial processes, including that of feedstock, construction material, furniture, paper, etc. The wood preservation by the dehydration process is one important preparation step in wood manufacturing industry which can help to increase the durability and resistance from being destroyed by fungus, to enhance the dimensional stability and to reduce the transportation cost. The wood drying process has been performed traditionally by a conventional kiln dryer with controlled heating, humidity and airflow under atmospheric pressure conditions [89,90]. Recently, with the key advantages in energy saving and low carbon dioxide emission (c.f. Section 3.1), superheated steam drying (SSD) with/without microwave or ultrasound assistance has been proved in many applications to be more appropriate compared to traditional drying techniques [29,91–93]. It has also been proved that the application of SSD can improve the quality of wood products [94]. Additionally, the SSD of different types of wood, such as rubberwood [95], radiata pine [96] and cedar wood [97], shows higher drying rates and lower drying time compared to hot air drying (HAD).

The moisture in wood, as a hygroscopic material, exists in two forms: the free water in the meso and macro pores, and the bound water. The bound water is accumulated in micro pores inside the solid matrix where the equilibrium vapor pressure is much lower than the saturation vapor pressure at the same temperature, which is known as Kelvin effect. This effect describes the dependency of the equilibrium vapor pressure on the radius of curvature of liquid-vapor interface. Since a concave curvature is formed within hygroscopic materials, the equilibrium vapor pressure is reduced as the pore size decreases. Therefore, a large driving force is required to remove the bound water in comparison to the free water. The bound water in cellular plant materials can additionally be detained by the permeable membrane walls.

Several theoretical studies of the heat and mass transfer inside porous media have been carried out to describe the SSD process of hygroscopic porous materials. Most models were developed based on the phenomenological concept of effective water diffusivity. The main assumption used in diffusion models is that the gaseous pressure within the medium is equal to the external pressure, or in other words, the advective vapor flow is negligible [98]. The impact of bound water on the drying characteristics in diffusion models may be reproduced by introducing the moisture pseudo-diffusivity which is moisture-content dependent. The magnitude of this moisture diffusivity should decrease when the drying process progresses further. In this manner, the diffusion models can express the nature of dehydration process of hygroscopic porous materials where the dehydration of the bound water at low moisture content regime becomes more difficult compared to the removal of free water at high moisture content regime [98]. In the frame of diffusion approach, several works were published to determine the moisture diffusivity for different materials subjected to SSD such as wood [99], meat [60–62], rice [100], Asian noodle [101], potato [55,101], soybean [102], etc. Note that with intensive drying processes where the internal evaporation occurs and offers a significant vapor overpressure within the medium, the contribution of advective gaseous flow in mass and energy conservation equations cannot be neglected and the diffusion models are therefore obviously not suitable [98]. In this situation, the SSD process involved in hygroscopic materials should be described by two-variable (moisture content, temperature) continuum models which can be derived using the volume averaging technique [13,98]. In several published continuum-scale models [89,98,103–105], the total water available in a hygroscopic porous medium is separated into free water and bound water. The driving force for transport of the bound water is assumed to be the gradient of superficial averaged bound water density or the gradient of water vapor density in gaseous phase [89,98]. Therefore, the pseudo-diffusivity of the bound water, which is practically a challenge to be measured, is an essential input parameter needed to perform the calculation. Alternatively, the impact of the bound water on the drying characteristics may also be taken into account by using the sorption isotherm

[63,65]. In this way, the bound water transport resistance from the micro to meso and macro pores and the diffusion resistance across the permeable solid layers are lumped by a reduction from saturation vapor pressure to equilibrium vapor pressure which is moisture content dependent. The equilibrium moisture content, which is an important criterion to distinguish hygroscopic materials from non-hygroscopic materials, is also well reproduced by this approach. Furthermore, one of the biggest advantages in using the sorption isotherm is that this property can easily be measured with high accuracy. One should note that the models cited up to here are based on a set of partial differential equations which need to be solved by time-consuming numerical techniques. The implementation of these sophisticated models in computational fluid dynamics (CFD) or in computational fluid dynamics coupled with discrete element method (DEM) simulations to describe the drying behavior of real dryers leads to very high computational cost which may be difficult to cover with the available computational resources (CPU and RAM). Due to high complexity of the mathematical description of heat, mass and momentum transfer between the phases, there is a very strong need for simpler drying models for particles in the CFD/CFD-DEM simulations. Alternatively, several semi-empirical approaches, such as the characteristic drying curve approach and the reaction engineering approach, can be employed to describe the SSD kinetics of single particles. These approaches have already been integrated in CFD simulations of spray drying towers as compromises between the computational demand and the accuracy in frame of the HAD process [106,107]. Additionally, a wide industrial application of the SSD process leads to a strong demand for accurate CFD or CFD-DEM simulations that may eventually help to optimize the design and operation of a dryer. Due to these facts, an accurate semi-empirical model for describing the heat and mass transfer between discrete phase (particles) and continuous phase (vapor) is strongly required.

Recently, Woo et al. [85] proposed a semi-empirical approach, the so-called master curve approach, for the SSD process of a small porous particle. In this model, the increment in surface temperature is calculated from the boiling temperature by introducing a multiplier term, whereas the reduction of drying rate over time is considered by a retardation coefficient which is moisture-content dependent. These unknown parameters, namely multiplier term and drying rate retardation coefficient, were correlated from the measured normalized temperature and normalized moisture content of ceramic particles [63]. In spite of an accurate prediction of the moisture content and temperature, the parameters used in the master curve model were established in a small range of laboratory operating conditions, thereby the validity of this master curve model can be questionable when it is applied under operating conditions prevalent in real SSD.

In this work, we propose a new methodology to determine the parameters of a semi-empirical model for the SSD process of a single wood particle (c.f. Fig. 4.1). Indeed, the

model parameters can be estimated directly from the experimental data performed in a wide range of operating conditions. However, the realization of experiments under severe operating conditions (i.e. very high temperature and/or velocity) and with a very small/large sample is rather difficult. Therefore, a sensitivity analysis that is conducted with a validated sophisticated model can help to overcome these limitations of experimental apparatus. One should note that the validation of the sophisticated model can also be done by using the experimental data available in literature without performing new measurements.

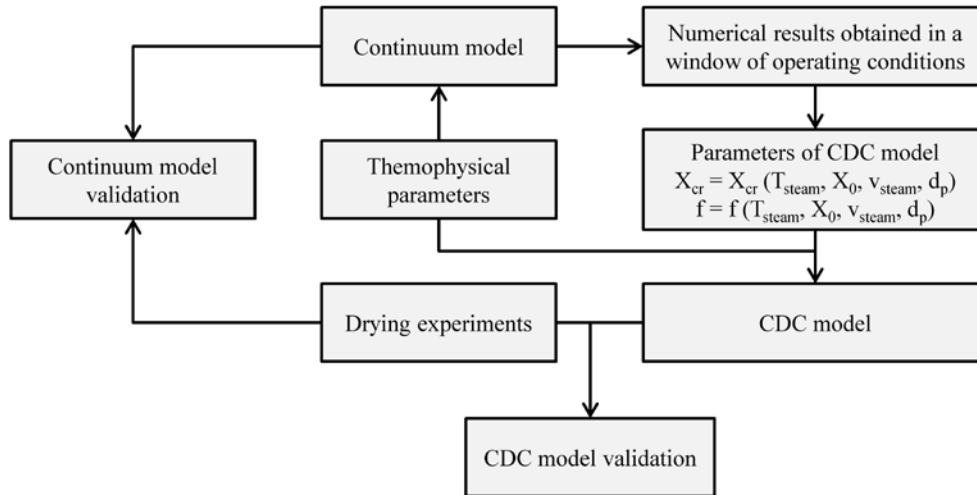


Figure 4.1: The strategy followed to determine characteristic drying curve (CDC) model parameters required to describe superheated steam drying of a single wood particle.

Following this introduction, a continuum-scale modeling of heat and mass transfer processes during superheated steam drying of a hygroscopic porous medium is briefly introduced. A set of thermophysical properties of wood particles, which serves as the drying product, are determined experimentally. The simulation results are validated against experimental data measured for single wood particles by using a magnetic suspension balance. Next, results of the continuum model simulations are used to establish correlations for the parameters needed in the characteristic drying curve model. The simulation results obtained from the reduced model are tested against both the experimental data and the results of the continuum model. Finally, conclusions of this work are drawn.

4.2 Continuum-scale model

As discussed in Sec. 3.1, if the initial product temperature is lower than the boiling temperature (or the saturation temperature) at a given pressure, the SSD process is comprised of three periods during each of which different heat and mass transfer mechanisms occur [108]. Firstly, the steam condenses on the sample surface, whereby the generated liquid may be accumulated as a film on the surface or it may penetrate into the

sample. The liquid film of condensate is removed during the surface evaporation period when the surface temperature reaches the saturation temperature. Then, the main drying period commences during which the internal moisture is removed. In this work, since we assume that the drying product is preheated up to the boiling temperature prior to drying, the surface condensation and evaporation periods are not accounted for.

4.2.1 Mass and energy conservation equations

The fluid transport in a porous wood sample, which is anatomically complex and heterogeneous, is structure dependent and thus anisotropic. The description of transport processes at the pore scale may provide understanding and interpretation of fluid flow and energy transfer under the impact of porous structure [108]; however it is sample specific and associated with high computational cost because of a large domain consisting of millions/billions pores. On the other hand, transport phenomena can be described by physics-based macroscopic models which are valid at the relevant level of description. These model equations can rigorously be derived from microscopic conservation equations by means of the volume averaging technique, which was proposed by Slattery [109] in the 1960s and thereafter extended to drying of porous materials by Whitaker [13]. The underlying idea behind the volume averaging technique is that the properties of fluid and solid phases such as velocity, density, pressure are averaged in a representative elementary volume (REV). A REV should be large enough to avoid the fluctuation due to micro heterogeneity of the morphological properties and small enough to neglect the variation of these morphological properties at the macro scale. Then, the macroscopic equations are derived from the conservation laws applied for each phase. In the following, the macroscopic fluid and thermal energy transport equations are briefly recalled.

The mass conservation of liquid is written as

$$\frac{\partial}{\partial t}(\rho_l \varepsilon_l) + \nabla \cdot (\rho_l v_l) + \dot{m}_v = 0, \quad (4.1)$$

where $\varepsilon_l = \frac{V_l}{V}$ denotes the volume fraction of liquid, ρ_l (kg/m³) and v_l (m/s) are the liquid density and the superficial liquid velocity, respectively. \dot{m}_v (kg/m³s) is the volumetric evaporation flux in the void space which serves as liquid sink in Eq. 4.1.

Similarly, the mass conservation of water vapor is described by

$$\frac{\partial}{\partial t}(\rho_l \varepsilon_l) + \nabla \cdot (\rho_l v_l) + \dot{m}_v = 0, \quad (4.2)$$

where $\varepsilon_v = \frac{V_v}{V}$ denotes the volume fraction of vapor, ρ_v (kg/m³) and v_v (m/s) are vapor density and superficial vapor velocity, respectively. The volumetric evaporation flux \dot{m}_v indicates a vapor source in Eq. 4.2.

Combining Eqs. 4.1 and 4.2 yields the water conservation equation expressed by

$$\frac{\partial}{\partial t}(\rho_l \varepsilon_l + \rho_v \varepsilon_v) + \nabla \cdot (\rho_l v_l + \rho_v v_v) = 0. \quad (4.3)$$

The energy conservation equation that accounts for the convective and conductive heat transfer as well as the latent heat due to the phase transition is written as

$$\frac{\partial}{\partial t}[\varepsilon_s \rho_s h_s + \varepsilon_l \rho_l h_l + \varepsilon_v \rho_v h_v] + \nabla \cdot (v_l \rho_l h_l + v_v \rho_v h_v) - \nabla \cdot (\lambda_{eff} \nabla T) = 0, \quad (4.4)$$

where h_s , h_l and h_v (J/kg) denote the specific enthalpy of solid, liquid and vapor phases, respectively. $\varepsilon_s = \frac{V_s}{V}$ denotes the volume fraction of the solid phase, whereas λ_{eff} (W/mK) is the effective thermal conductivity of the solid, liquid and vapor mixture.

4.2.2 Closure relations

The vapor and liquid velocity is given by the generalized Darcy's law

$$v_l = \frac{KK_{r,l}}{\mu_l} \nabla p_l, \quad (4.5)$$

$$v_v = \frac{KK_{r,v}}{\mu_v} \nabla p_v, \quad (4.6)$$

where K (m²) is the absolute permeability of the porous medium. $K_{r,l}$ and $K_{r,v}$ are the relative permeabilities of the liquid and gas phases, which are respectively calculated [65,110] as

$$K_{r,l} = \left(\frac{\varepsilon_l}{\psi} \right)^2 \text{ and } K_{r,v} = \left(1 - \frac{\varepsilon_l}{\psi} \right)^2. \quad (4.7)$$

Here, ψ denotes the porosity of the medium. The relationship between vapor and liquid pressure is described by Young-Laplace equation

$$p_v - p_l = p_c, \quad (4.8)$$

where p_c (Pa) is the capillary pressure. The vapor pressure p_v (Pa) is computed from the saturation vapor pressure $p_{v,sat}(T)$ and the sorption isotherm of the medium $\varphi(X,T)$ which is determined experimentally, as

$$p_v = \varphi(X,T) \times p_{v,sat}(T). \quad (4.9)$$

The saturation vapor pressure $p_{v,sat}(T)$ is given by the Antoine equation [111].

In the energy conservation equation (Eq. 4.4), the conductive heat flux through the medium is calculated by using the effective thermal conductivity λ_{eff} , which is assumed to be contributed by the liquid, vapor and solid phases. This effective thermal conductivity can be calculated theoretically [47] or can empirically be correlated as a function of moisture content and temperature.

4.2.3 Initial and boundary conditions

A wet porous particle of radius r_p , which is initially at uniform temperature T_0 and moisture content X_0 (kg water/kg dry solid), is subjected to convective drying by superheated steam at temperature T_{steam} and pressure p_{steam} . The heat transfer boundary condition at the particle surface ($r = r_p$) is written as

$$\frac{\partial}{\partial \bar{n}} \left[\lambda_{eff} \frac{\partial T}{\partial z} + \Delta h_{evp} \rho_l v_l + h_v (\rho_l v_l + \rho_v v_v) \right] = \alpha (T_{steam} - T), \quad (4.10)$$

where α is the effective heat transfer coefficient at the particle surface, which can be calculated by a modified Ranz–Marshal correlation that accounts for convective heat transfer only [63]; the radiative heat transfer would then be neglected. However, Komatsu et al. [112] proved recently that the contribution of radiation to the effective heat transfer coefficient is significant (approximately 50% for steam temperature 110-170 °C and particle diameter 5-10 mm). Therefore, in this work, the heat transfer coefficient α includes both convective and radiative heat transfer

$$\alpha = \alpha_{conv} + \alpha_{rad}. \quad (4.11)$$

The convective heat transfer coefficient α_{conv} is obtained by using an empirical correlation [63]

$$Nu = 2 + 0.616 Re^{0.52} Pr^{\frac{1}{3}}, \quad (4.12)$$

where $Nu = \frac{\alpha_{conv} d_p}{\lambda_v}$, $Re = \frac{v_{steam} d_p}{\nu_v}$ and $Pr = \frac{c_{p,v} \mu_v}{\lambda_v}$ are the dimensionless Nusselt, Reynolds and Prandtl numbers, respectively. d_p (m) is the particle diameter, and the physical and thermal properties of the vapor are determined at T_{steam} and p_{steam} . The temperature dependent radiative heat transfer coefficient is calculated by

$$\alpha_{rad} = \sigma_{rad} \varepsilon \frac{(T_{surf} + T_{steam})^3}{2}, \quad (4.13)$$

where $\sigma_{rad} = 5.67 \times 10^{-8} \text{ W/m}^2\text{K}^4$ denotes the Stefan-Boltzmann constant, and where ε denotes the thermal emissivity of the drying sample.

The mass transfer coefficient at the open surface is extremely large due to the absence of other gas molecules in the gas phase [63,65], therefore the vapor pressure at the particle surface remains constant at steam pressure $p_v = p_{steam}$.

The system of conservation equations (Eqs. 4.3 and 4.4) is formulated in a partial differential equation form which is suitable to be solved numerically by the finite element control volume method [98,110]. The implicit scheme is used to discretize the governing equations and the resulting discrete equations are solved iteratively.

4.3 Characteristic drying curve model

4.3.1 Mass and energy conservation equations

To describe the SSD process by means of a characteristic drying curve model, we assume that the moisture content and temperature are distributed uniformly within a particle. The main drying process is comprised of two periods: the constant drying rate (CDR) and the falling drying rate (FDR) period. During the CDR period, the particle acts as a pure water droplet and evaporation occurs at the saturation temperature without the effect of solid phase. Thus, the mass and heat transfer equations can respectively be written as

$$\left. \frac{dM_p}{dt} \right|_{CDR} = - \frac{\alpha A_p}{\Delta h_{evp}} (T_{steam} - T_{sat}(p_{steam})), \quad (4.14)$$

$$\left. \frac{dT}{dt} \right|_{CDR} = 0. \quad (4.15)$$

When the free water has evaporated entirely, the bound water starts being removed and the FDR period commences. The moisture content at which the CDR ceases and the FDR starts is referred to as critical moisture content X_{cr} (kg water/kg dry solid). The drying rate decreases during the FDR period as the resistance for bound water removal increases. The

reduction of drying rate during the FDR period compared to the CDR period is reflected by the drying rate retardation coefficient f , which is defined as

$$f = \frac{\left. \frac{dM_p}{dt} \right|_{FDR}}{\left. \frac{dM_p}{dt} \right|_{CDR}}. \quad (4.16)$$

Thus, the drying rate during the FDR period is calculated by

$$\left. \frac{dM_p}{dt} \right|_{FDR} = -\frac{f \alpha A_p}{\Delta h_{evp}} (T_{steam} - T_{sat}(p_{steam})). \quad (4.17)$$

The heat transfer equation during the FDR period is derived as

$$c_p M_p \left. \frac{dT}{dt} \right|_{FDR} = \alpha A_p (T_{steam} - T) - f \alpha A_p (T_{steam} - T_{sat}(p_{steam})). \quad (4.18)$$

The heat and mass conservation equations (Eqs. 4.14 and 4.15 during the CDR period or Eqs. 4.17 and 4.18 during the FDR period) of the CDC model are thus formulated in form of ordinary differential equations, which are then solved simultaneously in a computationally inexpensive manner.

4.3.2 Drying rate retardation coefficient and critical moisture content

Two unknown parameters of the CDC model are the drying rate retardation coefficient f and the critical moisture content X_{cr} . In literature, these parameters are experimentally established [113]. X_{cr} is often simply assumed as a constant value, whereas f is expressed as a function of normalized moisture content, which is defined as

$$X_n = \frac{X - X_{eq}}{X_{cr} - X_{eq}}, \quad (4.19)$$

where X_{eq} (kg water/kg dry solid) is the equilibrium moisture content. Despite its ability to describe experimental results, the extrapolative validity of the CDC model can be questionable when it is applied in a large range of operating conditions, which are essentially beyond the experimental conditions used to establish its parameters.

4.4 Material properties and drying experiment

4.4.1 Particle size distribution

In this study, beechwood particles were provided by Holz-Allerlei GmbH, Germany. The wood particles are consistent in shape and neither drilled nor waxed. The size distribution of the beechwood particles was measured offline by using an optical measurement device

(CAMSIZER, Retsch Technology GmbH, Germany). The particle size distribution varies between 6.0 mm and 6.5 mm with a mean diameter of 6.2 mm (see Fig. 2). The sphericity of the particles was also determined by using the CAMSIZER; the averaged value is about 0.95 (see inset in Fig. 2). Due to a narrow size distribution and a high value of sphericity, for numerical simulations a single wood particle is considered as a perfect sphere with diameter $d_p = 6.2$ mm.

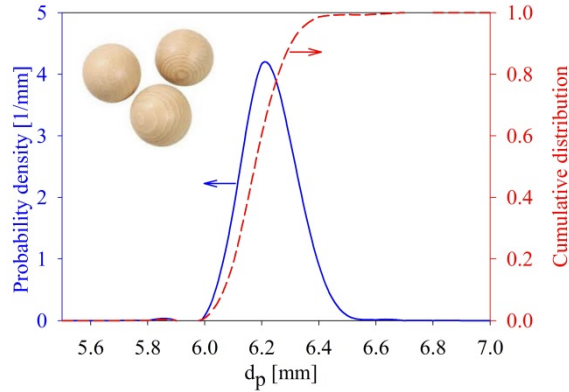


Figure 4.2: Size distribution of beechwood particles.

4.4.2 Sorption isotherm

The equilibrium vapor pressure at liquid-vapor interfaces (Eq. 4.8) in a partially saturated porous particle can be readily determined from the sorption isotherm of the particle. The sorption isotherm curve was measured by means of the sorption spectroscopy technique (Porotec GmbH, Germany). The relative humidity of the air was varied in a range of 0-95%, whereas air temperature remained constant at 20 °C. Note that the sorption isotherm of wood materials depends only marginally on temperature, for example, see Krupińska et al. [114] and Redman et al. [89] The measured sorption isotherm of the wood particles was then approximated as function of temperature and moisture content given by

$$\frac{p_v}{p_{v,sat}(T)} = \begin{cases} 1 & \text{with } X > X_{irr} \\ \frac{X}{X_{irr}} \left(2 - \frac{X}{X_{irr}} \right) & \text{with } X \leq X_{irr} \end{cases}, \quad (4.20)$$

where $X_{irr} = 0.256$ (kg water/kg dried solid) is the irreducible moisture content fitted from the experimental data. The equilibrium moisture content calculated by Eq. 4.20 together with the experimental data is shown in Fig. 4.3. It can be seen that the correlated sorption isotherm function approximates fairly well the experimental observations with a multiple regression coefficient of $R^2 = 0.98$.

If the moisture content X is higher than the irreducible moisture content X_{irr} , the equilibrium vapor pressure is at the saturation vapor pressure (according to Eq. 4.20) and

the moisture is comprised of free water, $X - X_{irr}$, and bound water, X_{irr} . Contrarily, if the moisture content is lower than X_{irr} , all moisture is considered as bound water. Bear in mind that only the free water can be transported via the advective liquid flow, whereas the bound water should be transformed into vapor by evaporation and then it can be advected towards the particle surface [89,98,110]. Therefore, when the moisture content reaches X_{irr} , the contribution of advective liquid flow in the heat and mass conservation equations (Eqs. 4.3 and 4.4) is disregarded. This means the liquid velocity v_l and pressure p_l are not accounted for in the computational procedure of the continuum model in the bound water regime.

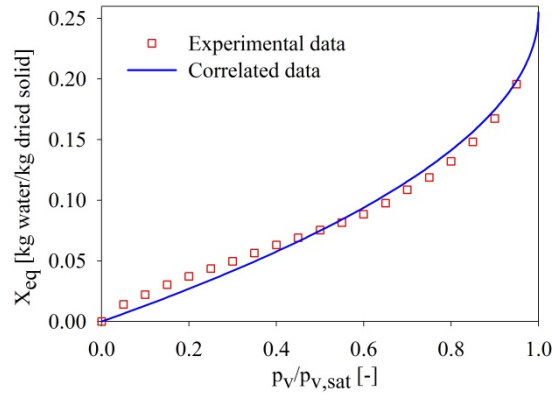


Figure 4.3: The measured and approximated sorption isotherms of a single wood particle.

4.4.3 Effective thermal conductivity

The conductive heat transfer is assumed to be contributed only by liquid and solid phases since the thermal conductivity of vapor is comparably small. The effective thermal conductivity of a wet porous medium can be calculated by using Ohmic combinations in parallel configuration as [47]

$$\lambda_{eff} = \lambda_s \varepsilon_s + \lambda_l \varepsilon_l. \quad (4.21)$$

In this way, the thermal conductivity of a dry porous medium can simply be expressed as $\lambda_{eff,dry} = \lambda_s \varepsilon_s$. A transient measurement was used to determine the thermal conductivity of dry wood particles by mean of the Hot Disk TPS Thermal Conductivity Instrument 2500 S (Thermtest Inc., Canada). In this device, both thermal conductivity and heat capacity can be calculated from the temperature during a transient heating process. The material properties are averaged over the sensor surface. It was obtained $\lambda_{eff,dry} = 0.138 \pm 0.001$ W/mK. The effective thermal conductivity of a wet porous particle is then computed by

$$\lambda_{eff} = \lambda_{eff,dry} + \varepsilon_l \lambda_l. \quad (4.22)$$

4.4.4 Specific heat capacity

In addition to the conductive heat transfer mechanism, convective heat transfer is involved in the thermal energy transport. The convective heat transfer mechanism is manifested as the energy flow due to the liquid and vapor transport, which is expressed as enthalpy flow. The enthalpies of solid h_s , liquid h_l and vapor h_v phases are computed based on the assumption of constant specific heat capacity, c_p , as

$$h_s = c_{p,s} (T - T_{ref}), h_l = c_{p,l} (T - T_{ref}) \text{ and } h_v = \Delta h_{evp} (T_{ref}) + c_{p,v} (T - T_{ref}), \quad (4.23)$$

where $T_{ref} = 0 \text{ }^\circ\text{C}$ is the reference temperature. In this work, the solid specific heat capacity is approximated by the specific heat capacity of the dry particle. The solid specific heat capacity $c_{p,s} = 770 \pm 36 \text{ J/kgK}$ was measured by the Hot Disk TPS Thermal Conductivity Instrument 2500 S.

4.4.5 Particle density and porosity

The solid mass density of the dry wood particles was measured by means of a Gas Pycnometer device manufactured by Micromeritics Instrument Corporation, USA. This device measures the actual solid density which excludes the pores. The measurements performed at room conditions for 1 kg of wood particles resulted in an averaged solid density of $\rho_s = 1326 \text{ kg/m}^3$.

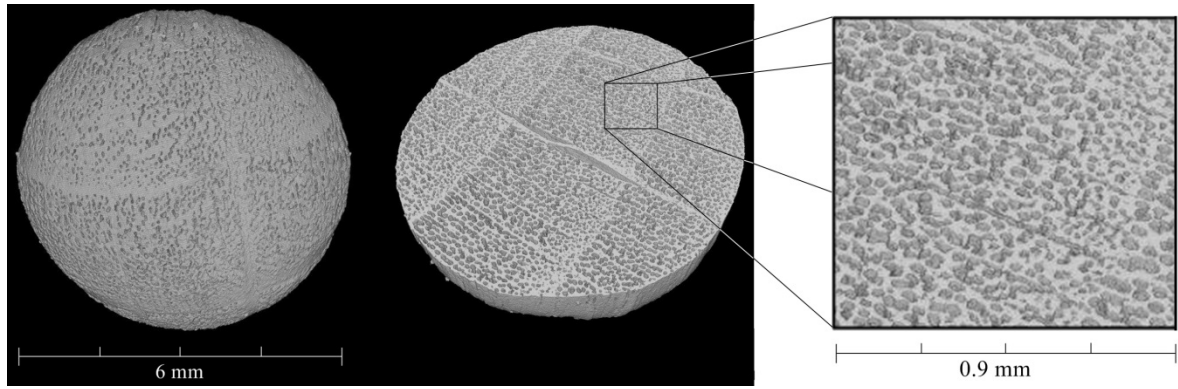


Figure 4.4: Surface texture and inner morphology of a single wood particle obtained from the X-ray μ -computed tomographic images.

The particle porosity was measured by two methods: density based method and X-ray μ -computed tomography technique. In the former method, the porosity is calculated from the apparent bulk density ρ_b and the actual solid density ρ_s of the particle, as $\psi = 1 - \frac{\rho_b}{\rho_s}$.

For 1 kg of wood particles the averaged particle apparent density of $\rho_b = 743 \text{ kg/m}^3$ was obtained (by using the Geo Pycnometer, Micromeritics Instrument Corporation, USA), yielding an averaged particle porosity of $\psi = 0.44$. In the latter method, the inner

morphology of a wood particle can be investigated based on the tomographic reconstruction (CT Procon alpha 2000, manufactured by ProCon X-ray GmbH, Germany). The unique feature of this technique is that the measurements can be repeated on a single particle [115,116]. The morphology of the wood particle is shown in Fig. 4.4. The beechwood particle can be considered as a porous medium made of an interconnected network of pores. The wood porosity deduced from X-ray μ -computed tomographic images is about $\psi = 0.39$. The difference in porosity values obtained by using the two methods is not remarkable. One reason for the moderate discrepancy may be due to the resolution of X-ray images, i.e. the voxel edge length of $2.2 \mu\text{m}$ was set for scanning measurements, which cannot resolve pores smaller than this voxel edge length (see Fig. 4.5a). The particle porosity of $\psi = 0.44$ is used for numerical simulations presented in this work.

4.4.6 Pore size distribution and equilibrium capillary pressure curve

The pore size distribution of a particle was measured by using a Mercury Porosimeter fabricated by Micromeritics Instrument Corporation, USA. Figure 4.5a presents the effective pore diameter over the intruded volume of mercury for wood particles. It should be noted that during the intrusion process within the mercury porosimetry, the non-wetting phase mercury serves as intruding phase which gradually occupies the medium originally filled by the wetting phase, in this case air. Similarly, non-wetting phase (vapor) invades the medium saturated by the wetting phase (liquid water) during the drying process. Therefore, it can be assumed that the invasion order of the pore space by non-wetting phase in intrusion process and the drying process is similar. It should be noted that the capillary pressure p_c (Pa) which is a function of wetting phase saturation is calculated from the pore diameter by using the Young-Laplace equation

$$p_c(S) = \frac{4\sigma(T)}{d_{pore}}, \quad (4.24)$$

where $\sigma(T [^\circ\text{C}]) = 10^{-3} \times (77.5 - 0.158T)$ (N/m) is the surface tension of liquid water. The saturation of the wetting phase is calculated by

$$S = 1 - \frac{V_{intr}}{V_{void}}. \quad (4.25)$$

For a given saturation of the wetting phase, the capillary pressure can be computed from the effective pore diameter (c.f. Eq. 4.24), which is obtained from the pore size distribution (c.f. Fig. 4.5a) at the intrusion volume fraction value calculated by Eq. 4.25. In this work, the capillary pressure curve is approximated with a multiple regression coefficient of $R^2 = 0.96$ as

$$p_c(S) = \frac{4\sigma(T)}{d_{pore}} \approx 2.147 \times 10^6 \sigma(T) \exp(5.461 \times 10^{-1.011 S}). \quad (4.26)$$

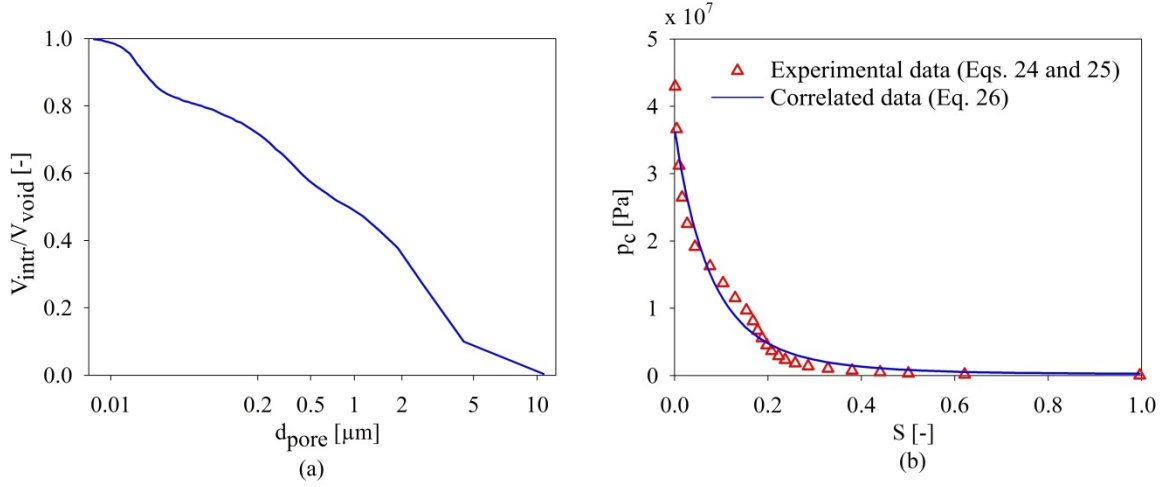


Figure 4.5: Pore diameter vs. intrusion volume obtained from mercury porosimetry (a) and capillary pressure vs. liquid saturation at 20 °C (b).

Table 4.1: Properties of the beechwood particle used for drying simulations.

Property	Value
Particle diameter d_p , mm	6.2 ± 0.3
Porosity ψ , -	0.44
Apparent solid density ρ_b , kg/m ³	743
Actual solid density ρ_s , kg/m ³	1326
Sorption isotherm $p_v/p_{v,sat}$, -	$\frac{p_v}{p_{v,sat}}(T) = \begin{cases} 1 & \text{with } X > X_{irr} \\ \frac{X}{X_{irr}} \left(2 - \frac{X}{X_{irr}} \right) & \text{with } X \leq X_{irr} \end{cases}$ $X_{irr} = 0.256 \text{ kg water/kg dry solid}$
Thermal conductivity of dry solid λ_{dry} , W/mK	0.138 ± 0.001
Specific heat capacity of dry solid $c_{p,s}$, J/kgK	770 ± 3.6
Capillary pressure curve p_c , Pa	$2.147 \times 10^6 \sigma(T) \exp(5.461 \times 10^{-1.011 S})$
Thermal emissivity ε , -	0.90
Absolute permeability K , m ²	55.5×10^{-15}

Figure 4.5b shows the capillary pressure computed by Eq. 4.24 and approximated by Eq. 4.26. Note that the contact angle is assumed zero in the Young-Laplace equation (Eqs. 4.24

and 4.26), leading to maximal values of the computed capillary pressure. Measurement of contact angle at the pore scale may in future result in further improvement of the accuracy of the model. The other properties of the wood medium such as absolute permeability $K = 55.5 \times 10^{-15} \text{ m}^2$ and thermal emissivity $\varepsilon = 0.90$ are referred to literature [89]. All aforementioned properties of the beechwood particle used in the continuum simulations are summarized in Table 4.1, whereas the thermophysical properties of liquid and vapor water are given in Appendix A.

4.4.7 Experimental setup for drying of a single wood particle

The superheated steam drying experiments of the single wood particles are performed in an apparatus shown in Fig. 4.6. This drying system is comprised of three main components: a micro-evaporator, a drying chamber and a magnetic suspension balance. The liquid is injected into the micro-evaporator, where the liquid is heated up and evaporates, and the generated vapor is superheated. By using a controllable micro-pump and a temperature controller, the mass flow rate and temperature of drying agent flowing into the drying chamber can be adjusted. The drying chamber with 26 mm diameter and 300 mm height is made of copper. An electrical heater and an insulation layer covering the external surface of the drying chamber maintain uniform temperature inside the chamber and prevent heat leakage to the environment. The steam enters at the bottom side, receives the water vapor evaporated from the drying sample and finally exhausts at the top of the drying chamber.

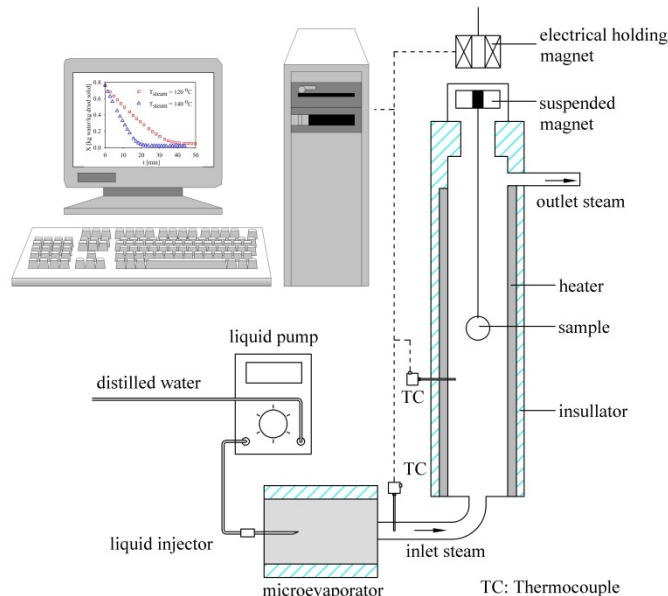


Figure 4.6: Schematic of the experimental setup used for drying of single wood particles.

The evolution of the sample mass over time is recorded by using a magnetic suspension balance (Rubotherm GmbH, Germany) that consists of a suspended permanent magnet, an electromagnet, a position sensor and a control system. The drying sample is hanged on a suspended permanent magnet. This permanent magnet is levitated by magnetic force

provided from the electromagnet outside the drying chamber under atmospheric conditions. Thus, the unique feature of this magnetic balance system is that the drying chamber can be isolated from the environment. The mass measurements can be performed in a large range of pressures and temperatures, but without interference from process pressure or temperature. Due to these aforementioned benefits, the magnetic suspension balance was successfully employed to investigate the drying kinetics of particles as reviewed in [117–119]. The balance operates in a mass range up to 10 g with a measurement resolution of $\pm 1 \mu\text{g}$. The sample mass measurements are recorded by the Rubotherm system control software (RSCS), whereas temperature and pressure of the drying chamber are logged by using a data acquisition system (Omega, USA).

The SSD process of wood particles was performed at four different temperatures of 120 °C, 140 °C, 160 °C and 180 °C, at a constant superheated stream velocity of 0.015 m/s. Before starting a drying experiment, the wood particles are moistened by soaking in liquid water at temperature 20 °C for 16 hours. This has led to an average initial moisture content of about 0.752 ± 0.023 (kg water/kg dried solid). The process conditions of the experiments are shown in Table 4.2. The raw experimental data is presented in Appendix E.

Table 4.2: Steam conditions and particle initial moisture contents used for drying experiments.

Steam temperature T_{steam} , °C	Steam velocity v_{steam} , m/s	Particle initial moisture content X_0 , kg water/kg dry solid
120	0.015	0.758
140	0.015	0.765
160	0.015	0.729
180	0.015	0.756

4.5 Results and discussion

4.5.1 Continuum model assessment

The continuum-scale simulations are carried out for wood particles with thermophysical and dimensional properties as presented in Tables 4.1 and Appendix A, under initial and boundary conditions as shown in Table 4.2. The evolution of the moisture content over time as well as the corresponding drying rate curves obtained from simulations and measurements at four different drying temperatures are shown in Fig. 4.7.

It can be seen that the simulation results agree well with the experimental data, especially at drying temperatures of 160 °C and 180 °C (c.f. Fig. 4.7a). At drying temperatures of 120 °C and 140 °C, the simulated moisture content is slightly overestimated compared to the

measured data. Furthermore, the drying process is comprised of constant drying rate (CDR) and falling drying rate (FDR) periods (c.f. Fig. 4.7b). During the CDR period, the particle surface remains sufficiently wet due to capillary action and the thermal energy supplied by convection is used for evaporation only. The presence of free water on the particle surface during the CDR keeps the equilibrium vapor pressure at saturation vapor pressure. Therefore, the particle surface temperature stays at saturation temperature (boiling temperature) under ambient pressure. When the transport of free water to the external surface of the particle can no longer keep up with the rate of evaporation over the entire surface, some surface regions become dry and the FDR period commences. The thermal energy is then used for both sensible heating and phase transition. When the surface area of the dry regions increases, removal of the (bound) moisture becomes more difficult since the sorption effect is stronger, viz. a smaller $p_v/p_{v,sat}$. The reduction in moisture content also leads to a reduction of the effective thermal conductivity (Eq. 4.22). Under the combination of these effects, the drying rate decreases during the FDR.

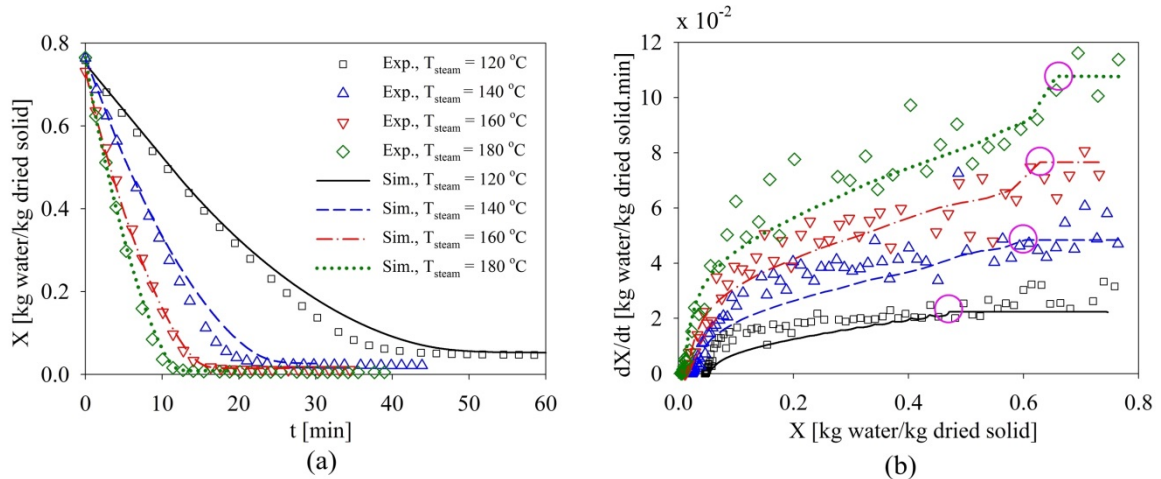


Figure 4.7: Continuum model predictions (lines) vs. experimental data (symbols): (a) evolution of moisture content over time, (b) drying rate curves. The legend of data in (b) is the same as in (a).

A good agreement between numerical and experimental results, for both moisture content and drying rate evolution, illustrates the predictive power of the present model to describe the SSD process of wood particles, at least for the type of wood considered in this study. The results also substantiate the hypothesis that the SSD process is comprised of both CDR and FDR periods [63,65,108].

The evolutions of moisture content, temperature and vapor pressure during drying of the particle are presented in Fig. 4.8. The simulation is performed at $T_{steam} = 120$ °C, $X_0 = 0.75$ kg water/kg dry solid, $v_{steam} = 0.015$ m/s and $d_p = 6.2$ mm. These drying conditions result in a critical moisture content of $X_{cr} = 0.47$ kg water/kg dry solid. Several selected moisture content, temperature and vapor pressure profiles in CDR period, i.e. at $X_{mean} = 0.6$ kg

water/kg dry solid (80% of X_0), transition point, i.e. $X_{mean} = X_{cr}$, and in FDR period, i.e. $X_{mean} = 0.3$ kg water/kg dry solid (40% of X_0), are presented in Fig. 4.9. The results show that the moisture content increases smoothly from the surface to the center of the particle. During the CDR period, the temperature and vapor pressure are uniformly distributed at the saturation temperature and the ambient pressure, respectively, in the entire domain.

When the surface moisture content reaches the irreducible moisture content X_{irr} , the FDR period commences. During this period, the temperature decreases smoothly from the surface to the center of the particle. Simultaneously, the internal vapor pressure increases due to an increase of saturation pressure of water with temperature. A drying front can be seen in moisture content, temperature and vapor pressure profiles (c.f. Fig. 4.9 at $X_{mean} = 0.4 X_0$). Due to the additional bounding force manifested by the decrease in equilibrium vapor pressure, the reduction of moisture content in the FDR period over time is lower compared to the CDR period that results in a front in the moisture content profile. The reduction of vapor pressure in the bound water regime leads to a sharp drop of vapor pressure in the vapor pressure profile; whereas the sensible heating in this bound water regime gives rise to a significant increase of the temperature near the surface.

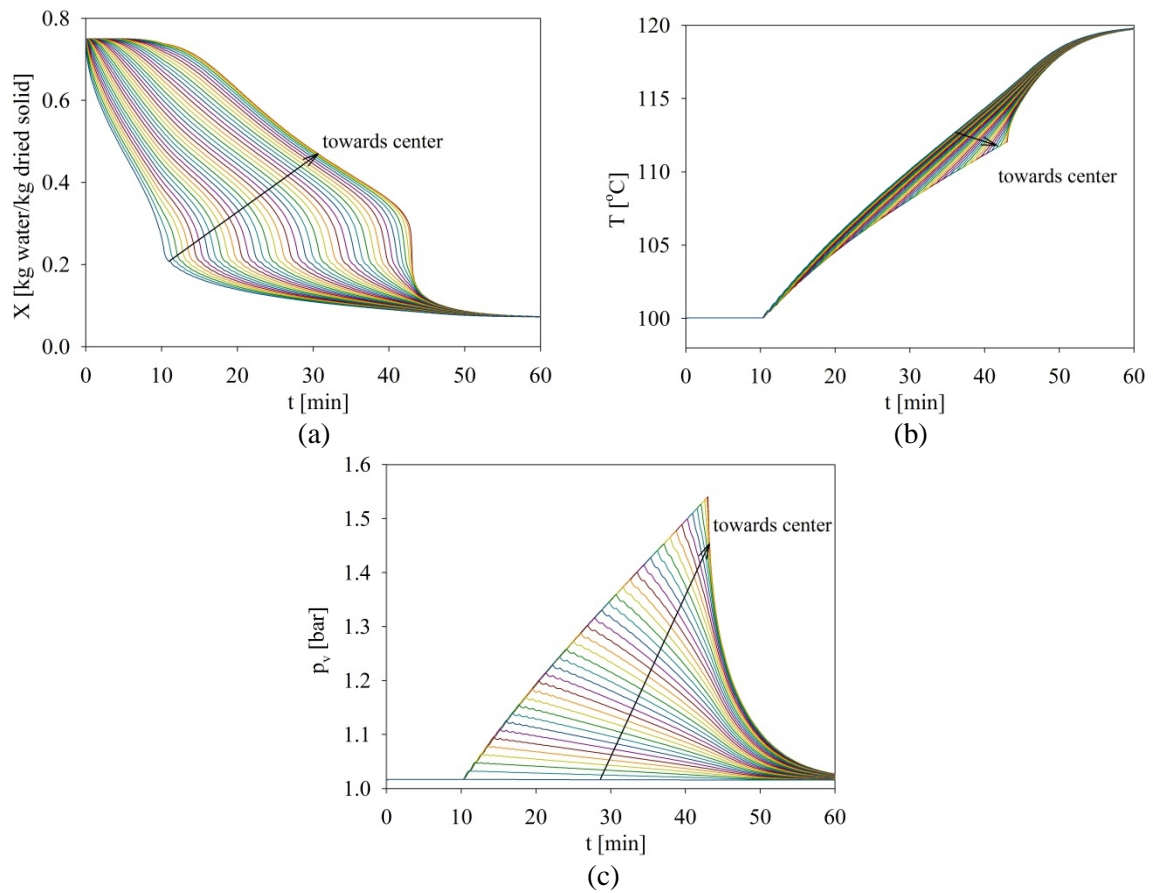


Figure 4.8: Evolution of moisture content, temperature and vapor pressure during drying of single wood particle.

The continuum model developed in this work appears to be a powerful simulation tool for SSD drying of a single wood particle. However, it entails high computational cost, because the partial differential equations (Eqs. 4.3 and 4.4) need to be solved in time and space using the finite volume method. Application of this numerical procedure, for instance in CFD/CFD-DEM simulations of a superheated steam fluidized bed dryer, can markedly increase computation time since thousands of particles need be tracked simultaneously. On the other hand, the implementation of this numerical procedure in such simulations to track the distribution of intraparticle moisture content and temperature is rather unnecessary. This is because the CFD solver requires only the heat and mass fluxes between the particles and the vapor phase. As an alternative, the continuum model can be reduced to a temporally resolved characteristic drying curve model. As discussed in the description of the CDC model, the critical moisture content and the retardation coefficient need to be correlated based on the results obtained from the drying measurements. However, it is practically a challenge and a highly time-consuming task to perform drying experiments at extreme operating conditions such as high steam velocities or with small particles. Therefore, in this work the parameters of the CDC model are numerically established by performing simulations with the continuum model according to the strategy proposed in Fig. 4.1. These simulations are carried out for a range of operating conditions and of particle initial moisture contents and sizes that may appear in reality.

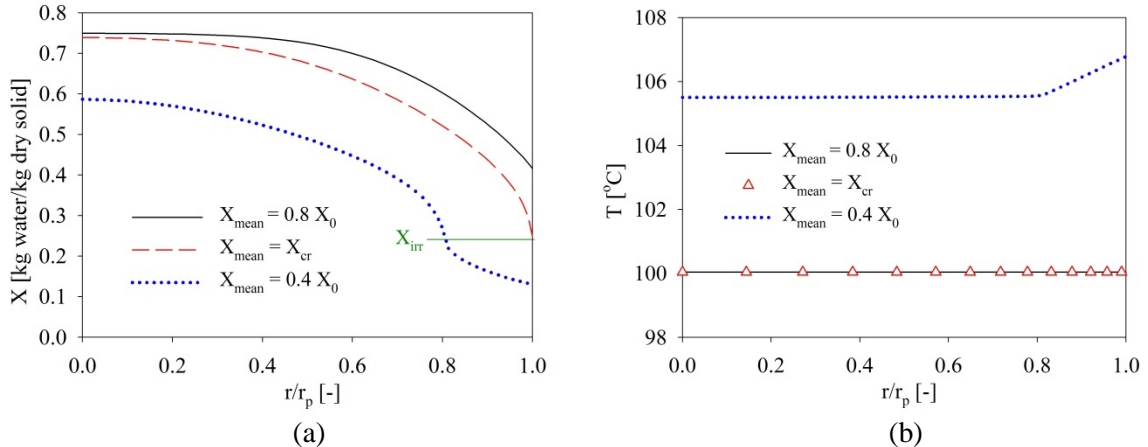


Figure 4.9: Profiles of moisture content (a), temperature (b) and vapor pressure (c) for the CDR period, for the transition point and for the FDR period.

4.5.2 Critical moisture content

The critical moisture content is the point at which the drying rate drops significantly, as marked by circles in Fig. 4.7b. In the framework of the continuum model, when the particle surface moisture content reaches the irreducible moisture content X_{irr} , then the average particle moisture content becomes X_{cr} . From this point on, the vapor pressure at the particle surface decreases due to the effect of bound water (c.f. Eq. 4.20). The continuum model simulations are carried out under various initial and boundary conditions, presented in Table 4.3. Based on the numerical results the following correlation for the critical moisture content has been deduced (units as is Table 4.3):

$$X_{cr} = -0.631 + 0.320T_{steam}^{0.277} - \frac{0.222}{X_0^{0.752}} + 0.020 \log(v_{steam}) + 0.614d_p^{0.152} \quad \text{with } R^2 = 0.96. \quad (4.27)$$

Table 4.3: Parameters and associated values used in the model reduction procedure.

Parameter	Value
Initial moisture content of particle X_0 , kg water/kg dry solid	0.30 - 0.75
Steam temperature T_{steam} , °C	120 - 180
Steam velocity v_{steam} , m/s	0.001 - 10
Particle diameter d_p , mm	0.2 - 20

Figure 4.10 delineates the moisture content profiles obtained from numerical simulations for four different sets of drying conditions at the respective critical moisture content. Compared to the reference simulation (Sim. 1), the other simulations (Sim. 2, Sim. 3 and Sim. 4) have been performed respectively at a higher steam velocity ($v_{steam} = 1$ m/s), a lower initial moisture content of particle ($X_0 = 0.3$ kg water/kg dry solid), and a larger particle diameter ($d_p = 20$ mm); the other model parameters remained unchanged. It can be seen from the correlation (Eq. 27) that a higher steam velocity leads to a higher critical moisture content. This is because the heat flux from the external steam towards the particle surface is enhanced at high steam velocity. The effect of the drying conditions on the critical moisture content of a non-deformable porous medium was also observed experimentally in literature [63,120].

A low level of heat flux abates the evaporation rate and thus the intraparticle moisture transport towards the external surface is prolonged. This is reflected in a reduction in the slope of the gradient in the moisture content, as can be seen in Fig. 4.10 (Sim. 1 vs. Sim.

2). In other words, the mean value of the particle moisture content (or the critical moisture content X_{cr}) at the transition point is larger at higher external heat flux.

In addition to the concept of the irreducible moisture content, the influence of the external heat flux on the critical moisture content can be explained by the contradictory roles of capillary action and viscous hydraulic resistance on the liquid displacement inside the particle. On one hand, the liquid is pumped by capillary action towards the external surface of the particle and the capillary pressure depends on the saturation and temperature, but not on the evaporation rate (c.f. Eq. 4.26). On the other hand, the hydraulic viscous resistance restrains the capillary pumping effect, and the pressure drop due to the viscous hydraulic resistance is linearly proportional to the liquid flow rate (c.f. Eq. 4.5). At low evaporation rate, corresponding to a low external heat flux, because of a small liquid pressure drop the capillary action is sufficiently powerful to keep the medium surface (at least partially) wet for a long time resulting in a low critical moisture content. The high evaporation rate suppresses capillary forces at the liquid-gas interfaces inside the particle, resulting in a very short, or even no CDR period. Equation 4.27 also indicates that a higher initial moisture content of the particle results in a higher critical moisture content. This comes from the fact that the reduction rates of the surface moisture content obtained with high and low initial moisture contents are seemingly similar if the external heat fluxes are identical. Thus, when the surface moisture content reaches the irreducible moisture content, higher intraparticle moisture content is obtained as shown in Fig. 4.10 (Sim. 1 vs. Sim. 3). In the same spirit, the mean moisture content at the transition point (or at the critical moisture content) increases monotonically with increasing initial moisture content.

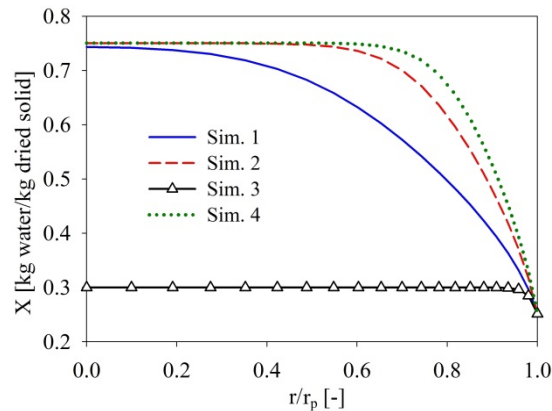


Figure 4.10: Moisture profiles at the transition point between the CDR and FDR periods, i.e. at the critical moisture content, obtained from numerical simulations for four different conditions: (Sim. 1) $T_{steam} = 120$ °C, $X_0 = 0.75$ kg water/kg dry solid, $v_{steam} = 0.015$ m/s, $d_p = 6.2$ mm; (Sim. 2) $T_{steam} = 120$ °C, $X_0 = 0.75$ kg water/kg dry solid, $v_{steam} = 1$ m/s, $d_p = 6.2$ mm; (Sim. 3) $T_{steam} = 120$ °C, $X_0 = 0.3$ kg water/kg dry solid, $v_{steam} = 0.015$ m/s, $d_p = 6.2$ mm; (Sim. 4) $T_{steam} = 120$ °C, $X_0 = 0.75$ kg water/kg dry solid, $v_{steam} = 1$ m/s, $d_p = 6.2$ mm.

mm; (Sim. 4) $T_{steam} = 120\text{ }^{\circ}\text{C}$, $X_0 = 0.75\text{ kg water/kg dry solid}$, $v_{steam} = 0.015\text{ m/s}$, $d_p = 20\text{ mm}$.

For drying of a smaller particle, the distance for the intraparticle moisture transport is shorter and the viscous pressure drop is smaller. Hence, the slope of the moisture content profile at the transition point is small, yielding a lower critical moisture content (Sim. 1 vs. Sim. 4 in Fig. 4.10). If the particle is sufficiently small, the critical moisture content will approximate the irreducible moisture content value.

4.5.3 Drying rate retardation coefficient

The drying rate retardation coefficient, f , and the normalized moisture content, X_n , are calculated based on the drying rate, dX/dt , and on the critical moisture content, X_{cr} , by using Eqs. 4.16 and 4.19, respectively. The impact of the drying conditions on the normalized drying curve is shown in Fig. 4.11.

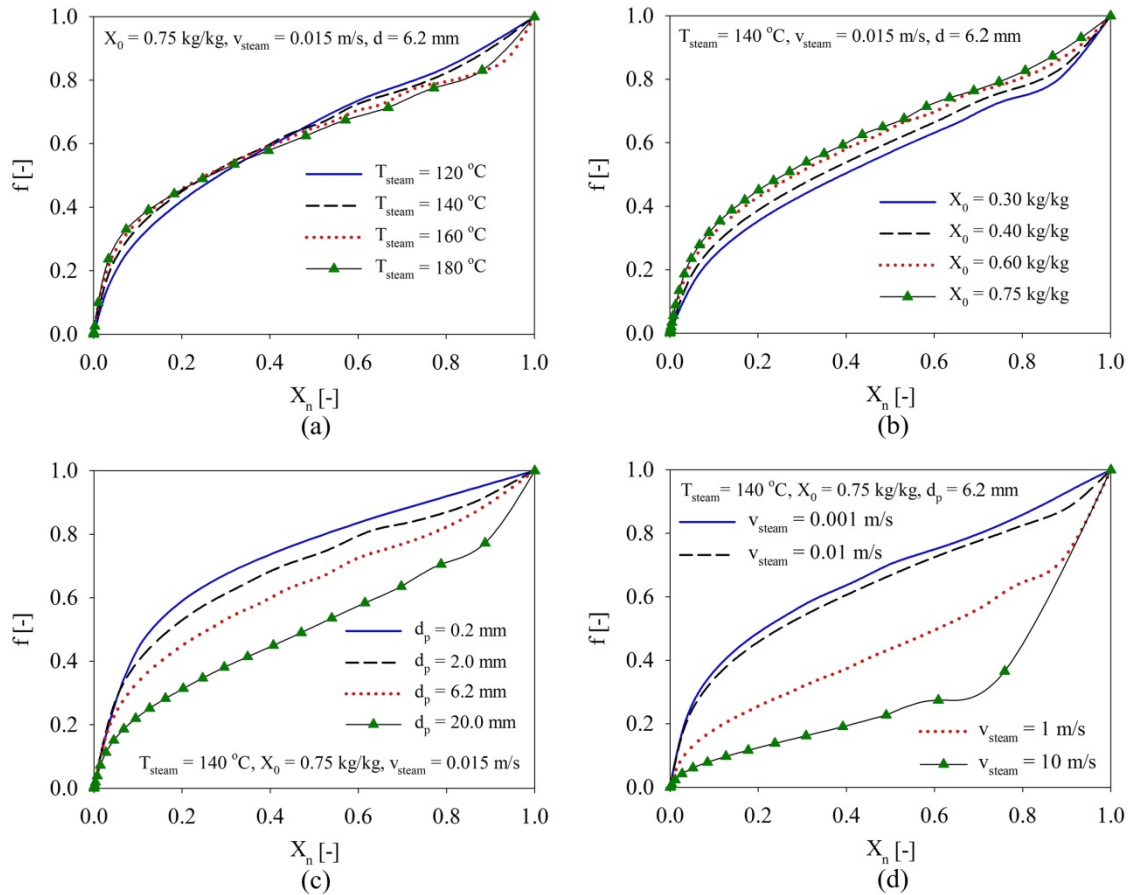


Figure 4.11: Influence of steam temperature (a), initial moisture content of particle (b), particle diameter (c) and steam velocity (d) on the normalized drying rate curve.

Generally, f can be expressed as $f = X_n^k$, where k is a constant exponent. However, the shape of the normalized drying curve in the FDR period varies significantly with the drying conditions (c.f. Fig. 4.11). Therefore, the power function is modified into a more

complex form where the constant k is replaced by a linear function of the normalized particle water content as

$$f = X_n^{aX_n+b}. \quad (4.28)$$

Here, the fitting coefficients a and b are obtained as functions of drying conditions, T_{steam} (°C) and v_{steam} (m/s), initial moisture content of the particle, X_0 (kg water/kg dry solid), and particle diameter, d_p (m),

$$a = 0.281 + 0.094T_{steam}^{0.61} - 0.956X_0^{0.61} + 0.180v_{steam}^{1.028} + 0.173 \log(v_{steam}) - \frac{0.107}{d_p^{0.264}} \text{ with } R^2 = 0.93, \quad (4.29)$$

$$b = 4.033 - 2.111T_{steam}^{0.1026} + \frac{0.017}{X_0^{1.632}} + 0.027 \log(v_{steam}) + 2.313d_p^{0.741} \text{ with } R^2 = 0.94. \quad (4.30)$$

The accuracy of the CDC model developed here is assessed by comparing the results obtained from this model with the continuum model predictions at steam temperatures of 140 °C and 160 °C, a particle diameter of 6.2 mm and an initial moisture content of 0.765 kg water/kg dry solid and 0.729 kg water/kg dry solid (Fig. 4.12).

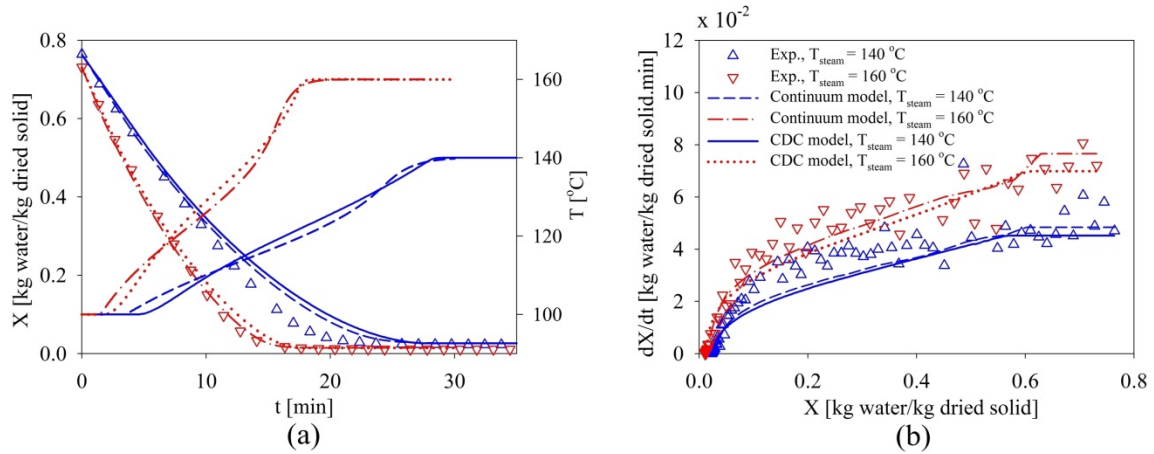


Figure 4.12: Evolution of the particle moisture content and of the temperature over time obtained from simulations and experiments (a), drying rate curves (b). The legend for data in (a) can be found in (b).

As can be seen, the reduced model reflects the moisture content and temperature evolutions over time well, and also the drying kinetic curves obtained from both the continuum model and from the experiments. This implies that parameter estimation from the continuum model simulations is reliable and can thus be applied to describe the drying process. This result may bring us to the conclusion that if the spatially lumped CDC model is implemented in future CFD simulations of dryers, it will provide a good compromise between computational demand and model accuracy.

Chapter 5

Continuum-scale modeling of superheated steam drying of cellular plant porous media

This chapter is a modified version of the paper *Continuum-scale modeling of superheated steam drying of cellular plant porous media* submitted to *International Journal of Heat and Mass Transfer* (2017).

5.1 Literature review

Drying plays a crucial role in the processing of plant porous materials with delicate cellular structures (i.e. fruits and vegetables). Because the quality preservation of these biological materials in drying is of essential importance, it should not be handled in an empirical way of trial and error. As an alternative, rigorous mathematical models based on the fundamental physical laws governing porous material drying have been developed to explore and assess the influence of both process conditions and material properties on the final quality of dried products.

Microscopic anatomy has revealed that the skeleton of fresh plant tissues generally has a reticulated character with individual cells. These cells are enclosed with semi-permeable walls. As stated in the literature, e.g. [121,122], in a fresh plant such as potato, eggplant, or cucumber, more than 90% of the total moisture exists inside the cell matrix, the so-called intracellular moist; only 5-10% of the total moisture is accumulated in the intercellular void space, named the extracellular moist. A common understanding is that during the drying process the intracellular moisture is transported outwards through the cell walls into the intercellular openings which are large enough to transport the fluid towards the external surface of the tissue structure [123]. Based on this understanding several mathematical

models accounting for various physical effects have already been formulated to predict the drying characteristics of biological materials.

Most of these models were developed based on Fick's second law of diffusion and the concept of an effective moisture diffusion coefficient [62,93,99,100,102,124], which is a phenomenological point of view. In these models, the moisture flow is not subdivided into liquid and gas mixture flow; it is, instead, treated as a one-phase flow and the effective moisture diffusion coefficient is fitted from the evolution of moisture content over time. Despite the ability of the cited kind of models to predict the evolution of moisture content over time, a detailed understanding of the fluid flow and evaporation processes in a cellular plant porous medium cannot be gained due to the aforementioned simplification where the transport resistance of the liquid-vapor flow created in both intercellular void space and cell membrane are lumped together in the effective diffusivity, a fitting parameter. Several continuous models [88,105,125] that take into account both liquid and vapor transport based on the volume averaging technique were also developed to simulate the plant drying process. In these models, the cellular plant tissue is considered as a rigid porous medium. The intracellular water is considered to be bound water and the membrane resistance for water transport is lumped in the sorption isotherm.

In the context of hot air convective drying (HAD), the most rigorous continuous models developed for the isothermal process of cellular plant porous media take into account both the diffusion of intracellular moisture across the cell membrane and the two-phase fluid flow in the intercellular void space [126–128]. However, there exists no equivalent model in the literature that describes the superheated steam drying process of cellular plant porous media. Therefore, our major motivation in this work is to couple the diffusive water flow across the cell membranes with the thermal effect in order to provide a better understanding of non-isothermal fluid flow involved in a cellular plant porous medium. The model-based studies performed in this work can also pave the way to optimize both the process energy consumption and the product quality.

In this chapter, a continuous model based on first principles is developed that accounts for the conjugate heat and mass transfer in a cellular plant porous medium during superheated steam drying at atmospheric pressure. In this model, the advective fluid flow within the intercellular void space is coupled with the diffusive flow across the cell membrane under the thermal effects. The model description including the constitutive relations required to close the set of conservation equations is presented. Numerical simulations are performed for a potato sample serving as the drying product. The simulation results are qualitatively validated by comparing against experimental data measured by a magnetic suspension balance. Next, a model-based sensitivity analysis is performed to delineate the influences

of cell membrane water conductivity and sample thickness on the drying behavior of the potato sample. Finally, conclusions of this work are drawn.

5.2 Model description

Cellular plant porous material is comprised of several types of cells such as parenchyma, collenchyma, and solute-conducting cells [129]. In this work, we consider the drying process in a tissue structured by parenchyma cells which are a primary component of plant porous materials [123]. As schematically shown in Fig. 5.1, the moisture within a fresh cellular plant porous medium is located in both the intercellular void space and the cell matrix. During the drying process, the intracellular water migrates outwards into the intercellular void space across the cell membrane. Since the intercellular void space can be occupied by liquid or vapor, the water diffusion from the cell matrix to this void space occurs in two ways: The water flux $j_{w,1}$ from the vacuole to the extracellular liquid and the liquid water/water vapor flux $j_{w,2}$ from the cell to the extracellular vapor which are visualized by red and violet arrows, respectively (see Fig. 5.1). These fluxes $j_{w,1}$ and $j_{w,2}$ are coupled with closure relations via the mass and energy conservation equations for the advective liquid and vapor flows.

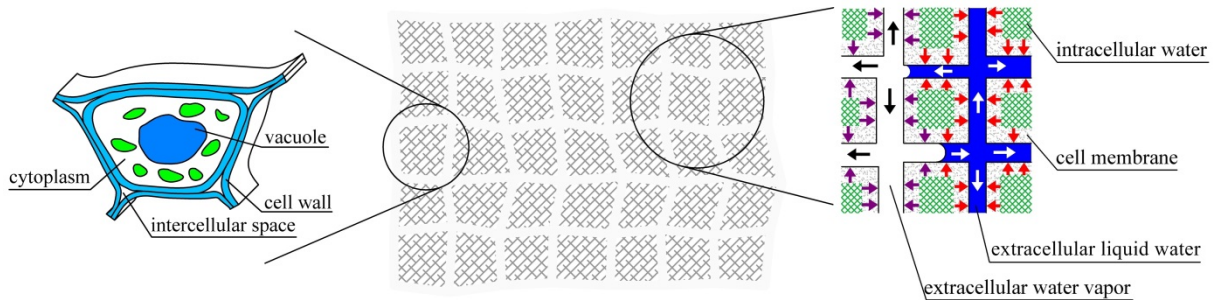


Figure 5.1: Pictorial representation of plant cell structure (left) and of fluid flow within cellular medium exposed to drying (right). The white and black arrows present the extracellular liquid and vapor flows, respectively. The red and violet arrows indicate the diffusive water flows across the cell membrane.

The main assumptions made in the development of our model are as follows: The gas and liquid phases are pure water vapor and liquid, respectively. As mentioned in the work of Whitaker [13], in capillary porous medium drying, the convective heat transfer in the fluid phase is relatively low compared to the conductive heat transfer. In other words, since there is a small temperature difference between the phases, the solid and fluid phases are assumed to be in a local thermal equilibrium. Only water molecules can get through the cell membrane, whereas the solute inside the cell is stationary. Fluid diffusion between neighboring cells is neglected. Cellular plant porous materials often tend to shrink during the drying process, especially at severe drying conditions. Shrinkage during drying can

rigorously be modeled by taking it into account in the heat and mass balance equations [124]. However, in this work, the volumetric shrinkage of a drying sample is simulated by correlating the evaporation surface area of the sample with the total moisture content. In the future, an advanced version of our model shall be developed to better account for this key aspect of cellular plant material drying.

As discussed in Sec. 3.1, the SSD of porous media might be comprised of three periods during each of which different heat and mass transfer mechanisms occur: condensation, surface evaporation, and main drying periods. Since the fresh cellular plant porous medium is almost fully saturated, liquid penetration during the surface condensation period is negligible and thus the surface condensation and evaporation periods are considered as a heating period. During this period the drying sample heats up from its initial temperature to the steam saturation temperature whereas the moisture content distribution remains unchanged. In this work, the initial temperature of the medium is assumed to be steam saturation temperature and, therefore, the surface condensation and evaporation periods are not considered. Despite these simplifications, the developed model is still capable of providing prominent features involved during the SSD process of a cellular plant porous medium. In this section, the components of this model are presented in detail.

5.2.1 Mass conservation for water in intercellular void space

To derive mass conservation equations for the liquid and vapor phases in the intercellular void space, a control volume is considered. The variation in the amount of extracellular liquid water in the control volume during the drying process is attributed to the (incompressible) advective liquid flux, the liquid water lost due to evaporation and the diffusive water flux across the cell walls. The latter two terms serve, respectively, as sink and source terms in the mass conservation equation

$$\rho_l \frac{\partial \varepsilon_{l,ext}}{\partial t} + \rho_l \nabla \cdot (v_{l,ext}) = -\dot{m}_v + j_{w,1} A_v \frac{\varepsilon_{l,ext}}{\varepsilon_{l,ext} + \varepsilon_{v,ext}}. \quad (5.1)$$

Here, $\varepsilon_{l,ext} = \frac{V_{l,ext}}{V}$, $\varepsilon_{v,ext} = \frac{V_{v,ext}}{V}$ denote the volume fractions of extracellular liquid water and water vapor, respectively; \dot{m}_v (kg/m³s) denotes the volumetric evaporation flux and $j_{w,1}$ (kg/m²s) the diffusive water flux; $v_{l,ext}$ (m/s) the superficial liquid velocity in the intercellular void space and ρ_l (kg/m³) the liquid mass density; A_v (m²/m³) denotes the volumetric specific area, which is the cell surface area within a unit volume. The term $A_v \frac{\varepsilon_{l,ext}}{\varepsilon_{l,ext} + \varepsilon_{v,ext}}$ refers to the cell surface area wetted by the liquid, where $\psi = \varepsilon_{l,ext} + \varepsilon_{v,ext}$ denotes the intercellular porosity of the medium.

As for the water vapor transport, the change in the amount of extracellular vapor in the control volume is caused by the (compressible) advective vapor flux. The vapor generated by evaporation \dot{m}_v (kg/m³s) and the diffusive water flux through the cell walls $j_{w,2}$ (kg/m²s) serve as vapor sources. The mass conservation equation for the extracellular water vapor can thus be written as

$$\frac{\partial(\rho_v \varepsilon_{v,ext})}{\partial t} + \nabla \cdot (\rho_v v_{v,ext}) = \dot{m}_v + j_{w,2} A_v \frac{\varepsilon_{v,ext}}{\varepsilon_{l,ext} + \varepsilon_{v,ext}}, \quad (5.2)$$

where $v_{v,ext}$ (m/s) denotes the superficial vapor velocity in the intercellular void space and ρ_v (kg/m³) the vapor mass density. By combining Eqs. 5.1 and 5.2, the mass conservation equation for the water in both liquid and gas phases in the intercellular void space reads

$$\begin{aligned} \rho_l \frac{\partial \varepsilon_{l,ext}}{\partial t} + \rho_l \nabla \cdot (v_{l,ext}) + \frac{\partial(\rho_v \varepsilon_{v,ext})}{\partial t} + \nabla \cdot (\rho_v v_{v,ext}) \\ - j_{w,1} A_v \frac{\varepsilon_{l,ext}}{\varepsilon_{l,ext} + \varepsilon_{v,ext}} - j_{w,2} A_v \frac{\varepsilon_{v,ext}}{\varepsilon_{l,ext} + \varepsilon_{v,ext}} = 0. \end{aligned} \quad (5.3)$$

As discussed before, there is only one mass transfer mechanism by which the liquid is removed from the cell matrix, i.e. the water diffusion through the cell membrane. Thus, the mass conservation equation for liquid water inside the cell matrix follows

$$\rho_l \frac{\partial \varepsilon_{l,int}}{\partial t} + j_{w,1} A_v \frac{\varepsilon_{l,ext}}{\varepsilon_{l,ext} + \varepsilon_{v,ext}} + j_{w,2} A_v \frac{\varepsilon_{v,ext}}{\varepsilon_{l,ext} + \varepsilon_{v,ext}} = 0, \quad (5.4)$$

where $\varepsilon_{l,int} = \frac{V_{l,int}}{V}$ denotes the volume fraction of cell water.

5.2.2 Energy conservation equation

Thermal energy is transported into the control volume by both conductive and convective heat transfer mechanisms. This energy is used for evaporation and heating up the porous medium. Invoking the local thermal equilibrium assumption, the energy conservation equation reads

$$\begin{aligned} \langle \rho c_p \rangle \frac{\partial T}{\partial t} + (c_{p,l} \rho_l v_{l,ext} + c_{p,v} \rho_v v_{v,ext}) \nabla \cdot T \\ = \nabla \cdot (\lambda_{eff} \nabla T) - \Delta h_{evp} \left(\dot{m}_v + j_{w,2} A_v \frac{\varepsilon_{v,ext}}{\varepsilon_{l,ext} + \varepsilon_{v,ext}} \right), \end{aligned} \quad (5.5)$$

where the heat capacity at constant pressure $\langle \rho c_p \rangle$ (J/m³) is calculated by

$$\langle \rho c_p \rangle = \varepsilon_s \rho_s c_{p,s} + (\varepsilon_{l,ext} + \varepsilon_{l,int}) \rho_l c_{p,l} + \varepsilon_{v,ext} \rho_v c_{p,v}. \quad (5.6)$$

5.2.3 Constitutive relationships

The generalized Darcy's law is used to calculate the superficial velocity of liquid and vapor in the intercellular void space. For the liquid phase, it reads as

$$v_{l,ext} = -\frac{KK_{r,l}}{\mu_l} \nabla p_{l,ext}, \quad (5.7)$$

and for the gas phase

$$v_{v,ext} = -\frac{KK_{r,v}}{\mu_v} \nabla p_{v,ext}, \quad (5.8)$$

where K (m^2) is the absolute permeability of the porous medium. $K_{r,l}$ and $K_{r,v}$ are the relative permeabilities of the liquid and the gas phase. The relative permeabilities can be obtained via measurement or computed from pore-scale simulations. In this work, these relative permeabilities are theoretically estimated as [65,110]

$$K_{r,l} = \left(\frac{\varepsilon_{l,ext}}{\psi} \right)^2 \text{ and } K_{r,v} = \left(1 - \frac{\varepsilon_{l,ext}}{\psi} \right)^2. \quad (5.9)$$

The relationship between the vapor and liquid pressures is described by the Young-Laplace equation

$$p_{v,ext} - p_{l,ext} = p_c(\varepsilon_{l,ext}), \quad (5.10)$$

where $p_c(\varepsilon_{l,ext}) = \frac{4\sigma(T)}{d_{pore}}$ denotes the capillary pressure which is traditionally considered

as a function of solely the liquid volume fraction $\varepsilon_{l,ext}$. The contact angle is assumed zero leading to maximal values of the computed capillary pressure. Measurement of contact angle at the pore scale may in future result in further improvement of the accuracy of the model. The vapor pressure $p_{v,ext}$ is computed from the saturation vapor pressure $p_{v,sat}(T)$ and the sorption isotherm of the medium $\varphi(X_{ext}, T)$, which can be determined experimentally, as

$$p_{v,ext} = \varphi(X_{ext}, T) \times p_{v,sat}(T), \quad (5.11)$$

where $X_{ext} = \frac{\varepsilon_{l,ext} \rho_l}{\varepsilon_s \rho_s}$ is the extracellular moisture content of the porous sample.

The saturation vapor pressure $p_{v,sat}(T)$ is given by the Antoine equation [130]

$$p_{v,sat}(T[^\circ\text{C}]) = \exp\left(23.462 - \frac{3978.205}{233.349 + T[^\circ\text{C}]}\right). \quad (5.12)$$

In the absence of other gas molecules, the saturation temperature (boiling temperature) of water depends only on the pressure, meaning that the vapor pressure level of the process can be set or changed by the temperature and moisture content as in Eq. 5.11.

In the energy conservation equation (Eq. 5.6), the conductive heat flux through the cellular medium is calculated by using the effective thermal conductivity λ_{eff} , which is assumed to be contributed by the liquid and solid phases only, since the thermal conductivity of the gas phase is relatively small. Thus, λ_{eff} is computed by using the Ohmic combination of resistances in parallel [47]

$$\lambda_{eff} = \varepsilon_s \lambda_s + \varepsilon_l \lambda_l. \quad (5.13)$$

The diffusive water fluxes through the cell membrane, i.e. $j_{w,1}$ and $j_{w,2}$, need to be known. These fluxes are calculated by using the definition of the water potential ϕ (Pa) as

$$j_{w,1} = -\rho_l L_p (\phi_{w,int} - \phi_{l,ext}), \quad (5.14)$$

$$j_{w,2} = -\rho_l L_p (\phi_{w,int} - \phi_{v,ext}), \quad (5.15)$$

where L_p (m^3/Ns) denotes the water conductivity of the cell membrane. Due to rupture of the cell membrane at high temperature, the water conductivity of the cell wall increases dramatically and thus water can easily be transported across the destroyed cell membrane. By means of BIA (Bio-electrical Impedance Analysis), Halder et al. [121] showed that cell membranes commence to be ruptured when the temperature is above 52 °C. At temperatures higher than 90 °C, cell membrane water conductance L_p was at least three orders of magnitude higher than at low temperature. However, due to the lack of precise data at high temperature, the water conductivity of the cell wall at 20 °C is used here as a reference, i.e. $L_p(20\text{ }^\circ\text{C}) = 1.8 \times 10^{-15} \text{ m}^3/\text{Ns}$ [127], and the cell membrane water conductance $L_p = 1000 L_p(20\text{ }^\circ\text{C})$ is used in the calculation. The impact of the water conductivity of the cell wall on drying characteristics is delineated through numerical simulations in Sec. 5.4.2.

The water potential ϕ of a system is defined as the difference of the total energy of water molecules and the liquid water molecule energy at the liquid-gas interface under atmospheric pressure in the volume of a unit mass. The water potential inside the cell $\phi_{w,int}$ consists of the gravity potential, pressure potential, matrix potential, and osmotic potential.

In this work, the water potential function in the cell $\phi_{w,int}$, which was empirically determined in [123] as a function of the moisture content, reads as $\phi_{w,int} = f\left(\frac{X_{int}}{X_{int,0}}\right)$,

where $X_{int} = \frac{\varepsilon_{l,int}\rho_l}{\varepsilon_s\rho_s}$ and $X_{int,0} = \frac{\varepsilon_{l,int,0}\rho_l}{\varepsilon_s\rho_s}$ (kg water/kg dry solid) denote the temporal and initial intracellular moisture content, respectively. Note that $X = X_{int} + X_{ext}$ denotes the total temporal moisture content of the sample. Particularly, the gravimetric experiment performed with potato at 50 °C resulted in a linear function as [123]

$$\phi_{w,int} = 10^6 \left(7.8 \frac{X_{int}}{X_{int,0}} - 7.8003 \right). \quad (5.16)$$

Admittedly, the relationship between water potential in the cell $\phi_{w,int}$ and moisture content ratio $\frac{X_{int}}{X_{int,0}}$ may be influenced significantly by the temperature. In the future, gravimetric experiments need to be performed at various temperatures to delineate the extent of the thermal effect on the water potential in the cell $\phi_{w,int}$. The water potential in the intercellular void space $\phi_{l,ext}$ is the capillary potential [129], i.e., $\phi_{l,ext} = -p_c$. Based on the kinetic theory of gases, the water vapor potential in the intercellular void space $\phi_{v,ext}$ is calculated from the difference of the Gibbs free energy of vapor molecules at given conditions compared to the Gibbs free energy of vapor molecules at the liquid-vapor interface at equilibrium conditions with the same temperature [129]

$$\phi_{v,ext} = \frac{\tilde{R}T\rho_l}{\tilde{M}_w} \ln \frac{p_{v,ext}}{p_{v,sat}}. \quad (5.17)$$

Here, \tilde{R} (J/mol K) denotes the universal gas constant and \tilde{M}_w (kg/mol) the molar mass of water.

5.2.4 Surface shrinkage

Assuming that the sample surface area shrinks linearly with the total moisture content X , the temporal surface area can be calculated as

$$A_{surf} = \frac{(A_{surf,0} - A_{surf,eq})(X - X_{eq})}{X_0 - X_{eq}} + A_{surf,eq}, \quad (5.18)$$

where $A_{surf,0}$, A_{surf} and $A_{surf,eq}$ are the initial, temporal and equilibrium surface area, respectively. Note that the volumetric shrinkage of the samples was about 80% in [124], which corresponds to surface area shrinkage of about 65.8%. Also, assuming that the

drying rate dX/dt is directly proportional to the evaporative surface area, the drying rate can be corrected as

$$\left(\frac{dX}{dt}\right)_{sh} = \frac{dX}{dt} \frac{A_{surf}}{A_{surf,0}}. \quad (5.19)$$

Dealing with this assumption, the moisture content evolution accounting for the surface shrinkage can be computed as

$$X_{sh} = X_0 - \int_0^t \left(\frac{dX}{dt}\right)_{sh} dt. \quad (5.20)$$

The subscript sh in Eqs. 5.19 and 5.20 refers to the properties after considering the sample shrinkage.

5.2.5 Initial and boundary conditions

The drying sample is a slab with thickness $2L$, which is initially at uniform temperature T_0 and moisture content X_0 (Fig. 5.2). The sample is subjected to convection from both sides to an environment at temperature T_{steam} and pressure p_{steam} . Due to symmetry, we consider only a half of the plane as computational domain.

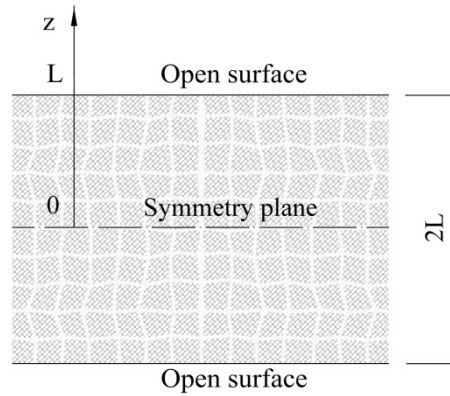


Figure 5.2: Schematic of a drying sample and its coordinate system.

At the open surface of the plane $z = L$ (c.f. Fig. 5.2), the heat transfer boundary condition is used

$$\left[\lambda_{eff} \frac{\partial T}{\partial z} + \Delta h_{evp} \rho_l v_{l,ex} + h_v (\rho_l v_{l,ex} + \rho_v v_{v,ex}) \right] = \alpha (T_{steam} - T_{surf}) \quad (5.21)$$

is used, where z denotes the vertical coordinate of the plane. The total gas-side heat transfer coefficient α ($\text{W}/\text{m}^2\text{K}$) includes both convective and radiative heat transfer

$$\alpha = \alpha_{conv} + \alpha_{rad}. \quad (5.22)$$

The convective heat transfer coefficient α_{conv} is constant at a given drying condition. It can be obtained analytically by the boundary layer solution or correlated empirically to [130]

$$Nu = 2 + 0.664 Re^{\frac{1}{2}} Pr^{\frac{1}{3}}, \quad (5.23)$$

where $Nu = \frac{\alpha_{conv} d_s}{\lambda_v}$, $Re = \frac{v_{steam} d_s}{\nu_v}$ and $Pr = \frac{c_{p,v} \mu_v}{\lambda_v}$ denote the dimensionless Nusselt, Reynolds and Prandtl numbers, respectively; d_s is the characteristic length of the sample.

The physical and thermal properties of the vapor are determined at T_{steam} and p_{steam} . The temperature-dependent radiative heat transfer coefficient is approximately calculated by [28]

$$\alpha_{rad} = \sigma_{rad} \delta (T_{surf} + T_{steam}) (T_{surf}^2 + T_{steam}^2) \approx \sigma_{rad} \delta \frac{(T_{surf} + T_{steam})^3}{2}, \quad (5.24)$$

where $\sigma_{rad} = 5.67 \times 10^{-8} \text{ W/m}^2\text{K}^4$ denotes the Stefan-Boltzmann constant and δ the thermal emissivity of the drying sample. The temperatures used in Eq. 5.24 are given in Kelvin.

Since the mass transfer coefficient at the open surface is extremely large due to the absence of other gas molecules in the gas phase [63,65], the vapor pressure at the open surface is assumed to be equal to the steam pressure during the drying process

$$p_v \Big|_{z=L} = p_{steam}. \quad (5.25)$$

Symmetric heat and mass transfer boundary conditions are imposed at $z = 0$:

$$\frac{\partial T}{\partial z} \Big|_{z=0} = 0, \quad (5.26)$$

$$\frac{\partial v_{v/l,ex}}{\partial z} \Big|_{z=0} = 0. \quad (5.27)$$

The continuous model developed in this work is solved by using the control volume finite element method. This numerical method was implemented here because it ensures the conservation of variables both in a control volume and in the whole computational domain. The discretization procedure is well described in the handbook of Patankar [131]. A Matlab code was developed to solve iteratively the discrete equations by using a built-in function *fsolve*.

5.3 Material and experimental setup

In this study, potato was chosen as the drying product due to its commercial value and highly cellular structure. An additional reason was that the thermophysical and structural properties of potato have been extensively measured in literature. A fresh potato (Miranda, early harvested) with minimum dimension larger than 30 mm was sliced at the middle into thin flat plates with thicknesses varying between 1.8 mm and 2.2 mm. Afterwards, discs were cut from each potato slice by using a hollow cylinder with an internal diameter of 9 mm. The samples were stored in a glass bottle inside a refrigerator to avoid water loss and used for the experiments in the same day. Though storage time can influence the initial total moisture content X_0 and the initial intracellular moisture content $X_{in,0}$, we assume an identical value of $X_{in,0}/X_0 = 0.96$ for all samples [121]. The morphological and hydraulic parameters of potato such as porosity, specific surface area per unit volume or absolute permeability of intercellular void space were obtained from the pore network approximation presented in [123]. The thermophysical properties of potato and of water vapor and liquid water are listed in Tables 5.1 and Appendix A, respectively.

The SSD system presented in Chapter 4 (Sec. 4.4.7) was reemployed to perform the drying experiment for the potato samples. In the present chapter, this experiment setup is re-illustrated in Fig. 5.3 together with the flow configuration over the drying sample. Before performing SSD experiments, a precise balance was used to determine the initial mass of the samples, which was 0.159 ± 0.008 g. The drying measurements were commenced when the superheated steam temperature had reached the desired stationary value with an error of ± 0.5 °C. The drying temperature was varied between 160 °C and 200 °C, whereas the steam mass flow rate remained constant at 0.25 g/min. The experiments were performed three times for each drying temperature to ensure the reproducibility of measured results. The total moisture content of the sample after drying is assumed to be equal to the equilibrium moisture content calculated based on the sorption isotherm (c.f. Table 5.1). From the equilibrium moisture content, the mass of dry solid and the initial moisture content are determined. The drying conditions are summarized in Table 5.2.

During these experiments, the sample is hanged vertically to ensure the flow configuration presented in Fig. 5.3. Thus, the characteristic diameter d_s used in the calculation of convective heat transfer coefficient α_{conv} (c.f. Eq. 5.23) is obtained by the ratio of surface area over the perimeter of projection perpendicularly to the steam flow, as [130]

$$d_s = \frac{2\pi dL + \frac{\pi d^2}{2}}{4L + 2d} \approx 8.35 \text{ mm.} \quad (5.28)$$

Using this characteristic diameter, the heat transfer coefficients are calculated (see Table 5.3). It can be seen that the contribution of radiative heat transfer mechanism is approximately 50% of the total heat transfer coefficient. This result is in agreement with the calculation made in [112].

Table 5.1: Thermophysical properties of the potato sample.

Parameter	Value/Equation
Absolute permeability of intercellular void space, K [123]	$4.168 \times 10^{-12} \text{ m}^2$
Specific cell surface area per unit volume, A_v [123]	$10885.62 \text{ m}^2/\text{m}^3$ with the effective cell size of $100 \text{ }\mu\text{m}$
Porosity, ψ [123]	0.0389
Pore size distribution [123]	$f = -1.313 \times 10^{-6} d^4 + 1.172 \times 10^{-4} d^3 - 3.371 \times 10^{-3} d^2 + 3.29 \times 10^{-2} d - 2.546 \times 10^{-2}$ <p>with $d_{min} = 2.9 \text{ }\mu\text{m}$ and $d_{max} = 29.49 \text{ }\mu\text{m}$</p>
Capillary pressure	$p_c(\varepsilon_{l,ex}) = \frac{4\sigma(T)}{d} \text{ where } \varepsilon_{l,ex} = \psi \frac{\int_{d_{min}}^d \frac{\pi d^2}{4} fd(d)}{\int_{d_{min}}^{d_{max}} \frac{\pi d^2}{4} fd(d)}$
Sorption isotherm [29]	$X = \frac{b_0 b_1 b_2 \varphi}{(1 - b_1 \varphi)(1 - b_1 \varphi + b_1 b_2 \varphi)}$ $b_1 = b_{10} \exp\left(\frac{b_{11}}{\tilde{R}T[\text{K}]}\right) \text{ and } b_2 = b_{20} \exp\left(\frac{b_{21}}{\tilde{R}T[\text{K}]}\right)$ <p>$b_0 = 8.7$, $b_{10} = 1.86 \times 10^{-5}$, $b_{11} = 34.1$ $b_{20} = 5.86$ and $b_{21} = 6.75$</p>
Density of solid, ρ_s [132]	143 kg/m^3
Specific heat capacity of solid, $c_{p,s}$ [132]	$1699 + 6.1T \text{ [}^\circ\text{C]} \text{ J/kgK}$
Thermal conductivity of solid, λ_s [133]	0.327 W/mK

Thermal emissivity, δ [134]

0.89

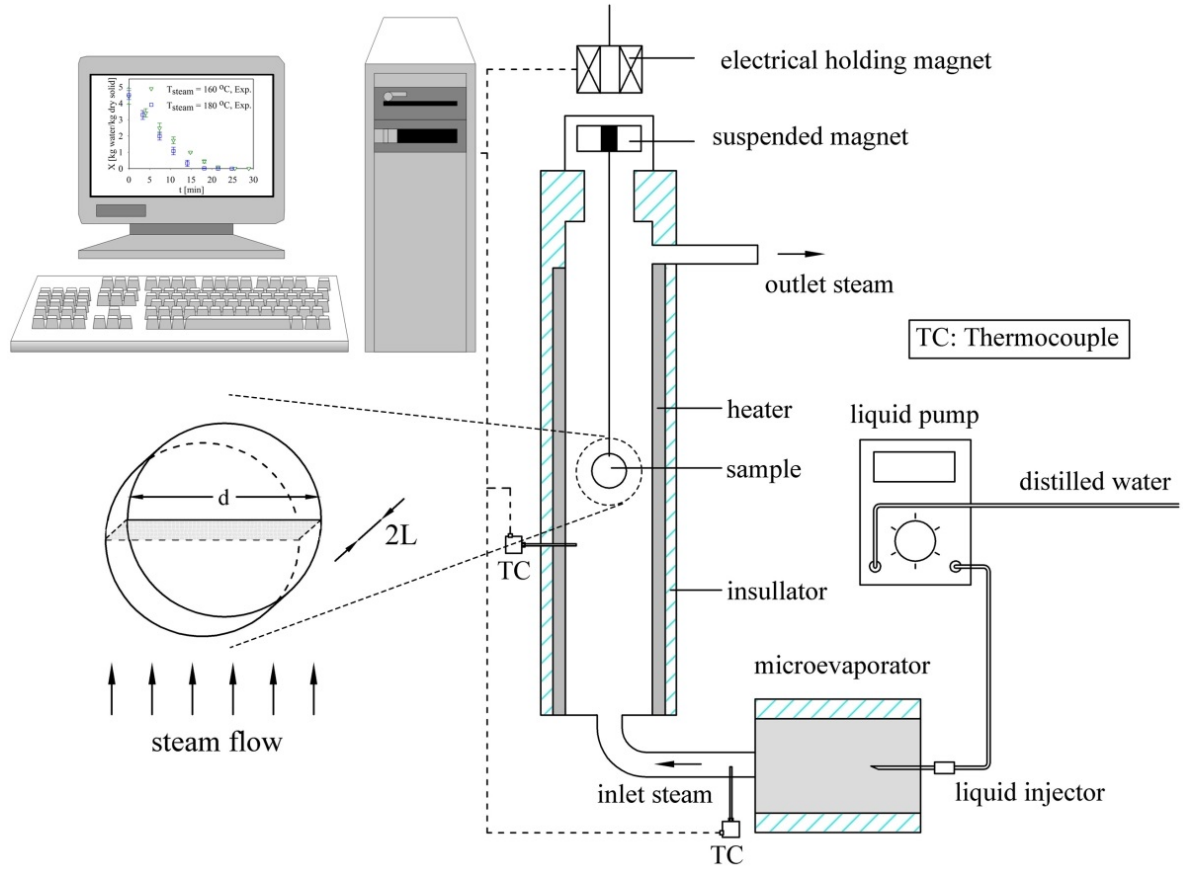


Figure 5.3: Schematic of the superheated steam drying system.

Table 5.2: Drying conditions and drying sample dimensions.

Parameter	Value
Ratio of initial intracellular moisture to initial total moisture content, $X_{in,0}/X_0$ [121]	0.96
Initial sample temperature, T_0	100 °C
Steam pressure, p_{steam}	1.015 bar ($p_{steam} = p_{v,sat}(100\text{ °C})$)
Steam mass flow rate, \dot{M}_{steam}	0.25 g/min
Sample thickness, $2L$	2.0 mm
Sample diameter, d	9 mm

Table 5.3: Heat transfer coefficients computed at three different steam temperatures.

T_{steam}	ρ_{steam}	v_{steam}	α_{conv}	α_{rad} computed at $T_{surf} = 100\text{ }^{\circ}\text{C}$
160 °C	0.52 kg/m ³	0.015 m/s	14.25 W/m ² K	13.22 W/m ² K
180 °C	0.49 kg/m ³	0.016 m/s	14.92 W/m ² K	14.23 W/m ² K
200 °C	0.47 kg/m ³	0.017 m/s	15.62 W/m ² K	15.29 W/m ² K

5.4 Results and discussion

5.4.1 Model validation

A comparison between the simulated and measured moisture content evolution over time and drying rate curves at three different drying temperatures is shown in Fig. 5.4. The error bars in Fig. 5.4a correspond to the deviation of three repetitions, whereas in the drying rate curves all repetitions are plotted together, resulting in data point swarms (c.f. Fig. 5.4b).

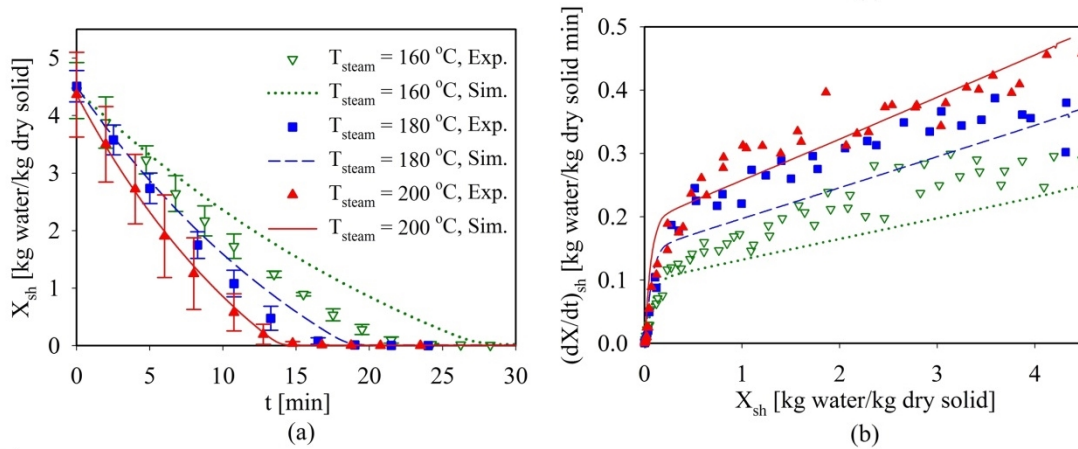


Figure 5.4: Evolution of moisture content over time (a) and the corresponding drying rate curve (b) obtained from simulations (Sim.) incorporating the surface area reduction and experiments (Exp.) The legend for (b) is identical to (a).

Overall, these simulation results and measurement data indicate features similar to those commonly observed for drying cellular plant porous materials [101,135]. Essentially one cannot expect a perfect match, because the initial moisture contents and the exchange surface areas of the samples are not identical. At drying temperatures of 180 °C and 160 °C, the model tends to underestimate the change in the moisture content of the sample compared to the corresponding measured data. This discrepancy could be due to the identical values of surface shrinkage and cell membrane water conductance, which were

used in the simulations for different temperatures. Nevertheless, qualitative agreement between experimental and simulated data, especially in the evolution of drying rate, implies the potential of the present model in predicting the drying behavior of potato samples.

5.4.2 Impact of cell membrane water conductivity on drying behavior

At high drying temperatures moisture migration pathways can be created in a cellular porous medium by the rupture of its cell membranes [121]. As a result of this structural alteration, it is estimated that the difference between the water transport resistance at high and low temperatures is three orders of magnitude. In this section, the impact of cell membrane water conductivity L_p on the drying characteristics is studied by performing numerical simulations for three different values of L_p , varying by several orders of magnitude between $L_p(20\text{ }^\circ\text{C}) = 1.8 \times 10^{-15} \text{ m}^3/\text{Ns}$ and $10^3 \times L_p(20\text{ }^\circ\text{C}) \text{ m}^3/\text{Ns}$. The simulation results are presented in Figs. 5.5-5.8. Note that the surface shrinkage effect is disregarded from the simulation results presented in this and in subsequent sections.

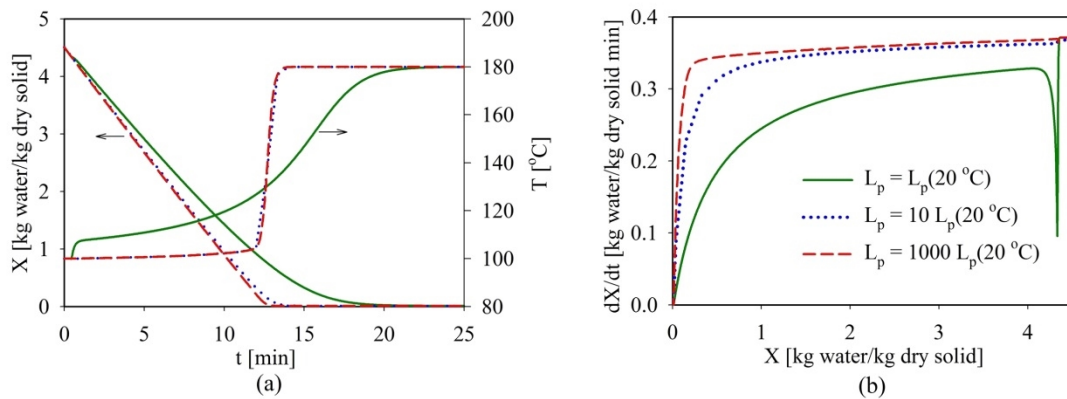


Figure 5.5: Temporal evolution of total moisture content and average temperature (a) as well as of drying rate (b) of the porous medium for three different values of cell membrane water conductivity. The steam temperature, steam mass flow rate and initial moisture content of potato are 180 °C, 0.25 g/min and 4.5 kg water/kg dry solid, respectively.

As can be seen in Fig. 5.5, the drying process in the porous medium with high L_p is markedly enhanced due to a low hydraulic resistance to water diffusion across the cell membrane. The thermal energy supplied to the medium surface by convection is primarily used to evaporate liquid water and hence the average temperature of the medium remains nearly at the saturation temperature during a significant period of the drying process. With further evaporation the medium temperature increases drastically because the thermal energy is then mostly used for sensible heating of the medium. On the other hand, the thermal energy supplied to the porous medium surface with low L_p is partly used for sensible heating, yielding an early increase in the average temperature of the medium. The moisture content decays monotonically irrespectively of the value of L_p . It is in fact a

challenge to determine the value of L_p directly from experiments [121]. Use of the present model to derive the value of L_p for a given cellular sample by comparison of simulated and measured drying data seems to be an attractive alternative.

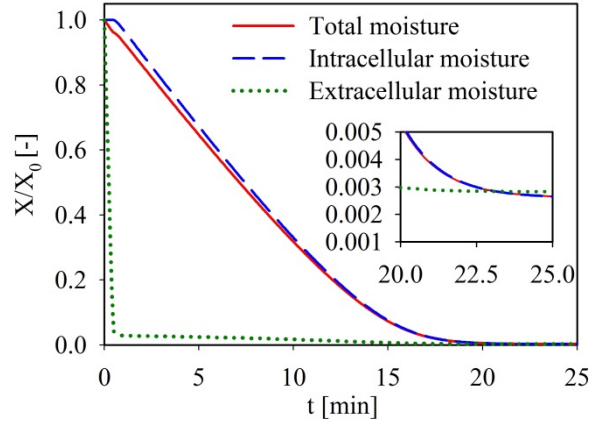


Figure 5.6: Evolution of the normalized total, intracellular and extracellular moisture content over time obtained from simulations. Parameters used in simulations are: $T_{steam} = 180\text{ }^\circ\text{C}$, $\dot{M}_{steam} = 0.25\text{ g/min}$ and $X_0 = 4.5\text{ kg water/kg dry solid}$ and $L_p = L_p(20\text{ }^\circ\text{C})$.

One noticeable discrepancy among the drying rate curves is the deflation-inflation behavior in the beginning of the drying rate curve for low L_p . This anomalous behavior may be due to the coupling of a high external heat flux with a low water conductance of cell membrane. In order to gain insight into this abrupt change in the rate of moisture removal, the time evolution of the total, intracellular and extracellular moisture content of the sample with $L_p = L_p(20\text{ }^\circ\text{C})$ are shown in Fig. 5.6. As can be seen, while the extracellular water is removed the intracellular water seemingly remains unchanged. The normalized extracellular water drops sharply in this period since the thermal energy supplied to the sample is completely used for extracellular water evaporation. With further evaporation, vapor pressure in the intercellular void space starts to decrease due to the sorption isotherm, therefore the drying rate drops. Note that the wetted area of the

extracellular void space $A_v \frac{\varepsilon_{l,ext}}{\varepsilon_{l,ext} + \varepsilon_{v,ext}}$ is small, therefore the contribution of the water

diffusive flux $j_{w,1}$ to mass conservation is marginal. With further evaporation, the diffusion of intracellular water across the cell membrane to the vapor phase controls the drying process. As mentioned earlier (c.f. Eq. 5.15), the diffusion flow $j_{w,2}$ depends on the water conductivity of the cell membrane L_p as well as on the potential of intracellular water $\phi_{w,int}$ and of extracellular vapor $\phi_{v,ext}$. Since the value of L_p and the correlation for $\phi_{w,int}$ (c.f. Eq. 5.16) are given at low temperature, the drying rate is expected to be low. This reduction of the drying rate implies that most of the thermal energy supplied at the surface by

convection is used to heat up the medium and thus its temperature increases. With increasing medium temperature, $p_{v,sat}(T)$ increases but $\phi_{v,ext}$ in the intercellular void space decreases (c.f. Eq. 5.17). Hence both the diffusion flow $j_{w,2}$ and the drying rate increase again. Note that this anomalous behavior occurs in a very small range of moisture content (for instance, 4.21 - 4.10 kg water/kg dry solid at steam temperature $T_{steam} = 180$ °C); therefore, its impact on the moisture content evolution is insignificant. With high water conductance of cell membrane, i.e. $L_p = 1000L_p(20\text{ °C})$, despite of a small difference $\phi_{w,int} - \phi_{v,ext}$, the water diffusive flux $j_{w,2}$ is sufficiently high to avoid this anomalous behavior.

A natural question arises now as to whether the distribution of moisture content and temperature within a sample during the drying process relies on the value of L_p . To this purpose, the evolution of moisture content X and temperature T profiles along the z coordinate over time t obtained from simulations for three different values of L_p are presented in Figs. 5.7 and 5.8, respectively. As can be seen in Fig. 5.7a, the moisture content distribution in a porous medium with low L_p is essentially uniform in space (i.e. almost independent of the z coordinate) during the drying process. This can be understood from the fact that in this porous medium the resistance for moisture transport across its cell membranes is high and the water diffusion flux $j_{w,2}$ is thus impeded. On the other hand, the thermal energy transferred convectively from the drying agent penetrates deep into the medium thereby heating it uniformly. The distribution of the water vapor potential in the intercellular void space $\phi_{v,ext}$ and thus the water diffusion flux $j_{w,2}$ along z direction becomes homogeneous, resulting in a uniform moisture distribution. In contrast, in a porous medium with high L_p the diffusion of intracellular water is more pronounced. The moisture removal from the medium surface is thereby favored as most of thermal energy is used for the evaporation of the surface moisture (c.f. Fig. 5.7c).

Moreover, the evolution of specimen temperature during the drying process is affected by the value of L_p . In a medium with low L_p , since the dehydration of intracellular water is restrained due to high water transport resistance, the latent heating happens simultaneously throughout the medium thickness. The average temperature of the medium with low L_p increases fast compared to the sample with high L_p (c.f. Fig. 5.8). Indeed, the slow dehydration process leads to a more pronounced sensible heating and thus a faster temperature rise. Contrary, the surface of the sample with high L_p is heated sensibly late in the process, after the moisture has been removed (at times $t = 8$ min and 10 min). Then, however, the surface temperature increases fast whereas the temperature at the medium center remains at saturation, resulting in a large difference between surface and center temperature of the sample. For instance, the values of $\Delta T = T|_{z=L} - T|_{z=0}$ at $t = 10$ min

obtained for L_p (20 °C) and $1000 L_p$ (20 °C) are 1.89 °C and 4.25 °C, respectively, as can be seen in Fig. 5.8.

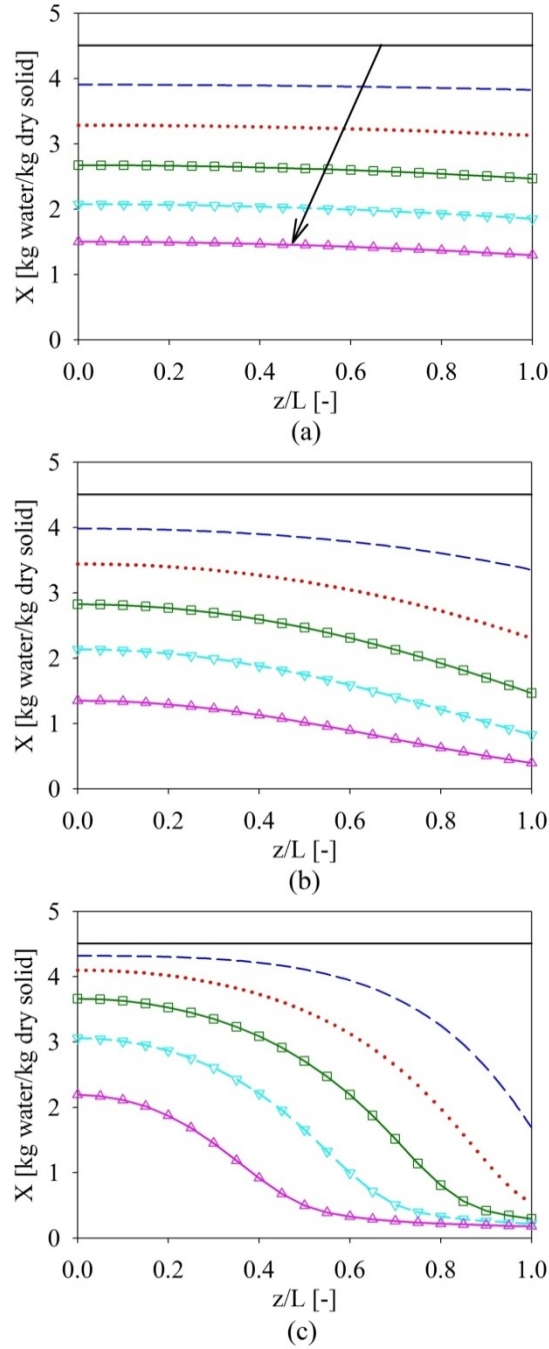


Figure 5.7: Moisture content profiles of the porous medium for three different values of cell membrane water conductivity: (a) $L_p = L_p$ (20 °C), (b) $L_p = 10 L_p$ (20 °C) and (c) $L_p = 1000 L_p$ (20 °C). The evaporative surface of the medium is located at $z/L = 1$. The profiles are plotted for a time period of $t = 10$ min with an interval of 2 min. Other parameters used in simulations are: $T_{steam} = 180$ °C, $\dot{M}_{steam} = 0.25$ g/min and $X_0 = 4.5$ kg water/kg dry solid.

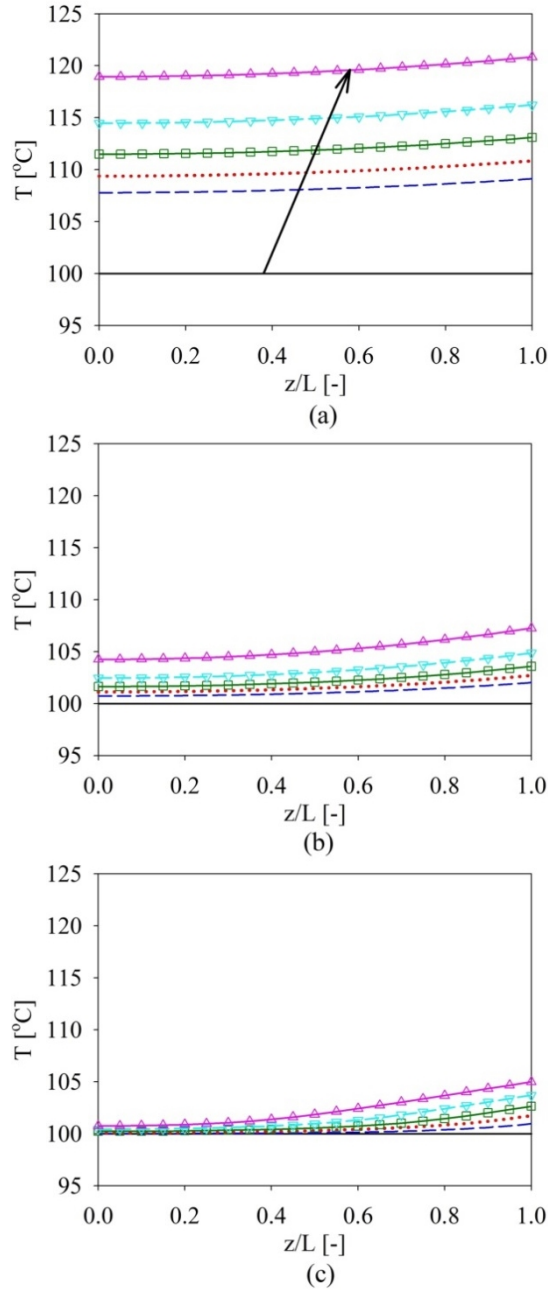


Figure 5.8: Temperature profiles of the porous medium for three different values of cell membrane water conductivity: (a) $L_p = L_p$ (20 °C), (b) $L_p = 10 L_p$ (20 °C) and (c) $L_p = 1000 L_p$ (20 °C). The evaporative surface of the medium is located at $z/L = 1$. The profiles are plotted for a time period of $t = 10$ min with an interval of 2 min. Other parameters used in simulations are: $T_{steam} = 180$ °C, $\dot{M}_{steam} = 0.25$ g/min and $X_0 = 4.5$ kg water/kg dry solid.

5.4.3 Impact of sample thickness on drying behavior

In this section, the influence of sample thickness on the drying behavior is investigated numerically by varying the sample thickness between 1 mm and 2 mm, whereas other parameters remain unchanged. The simulation results are presented in Figs. 5.9-5.12.

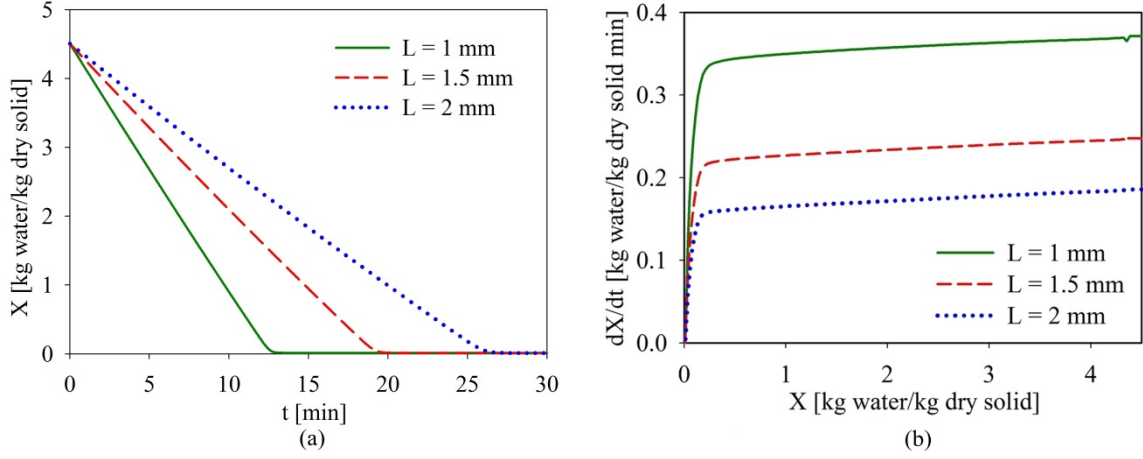


Figure 5.9: Evolution of moisture content over time (a) and the drying rate curve dX/dt vs X (b) for different values of sample thickness. Other parameters used in simulations: $T_{steam} = 180\text{ }^{\circ}\text{C}$, $\dot{M}_{steam} = 0.25\text{ g/min}$, $X_0 = 4.5\text{ kg water/kg dry solid}$ and $L_p = 1000 L_p(20\text{ }^{\circ}\text{C})$.

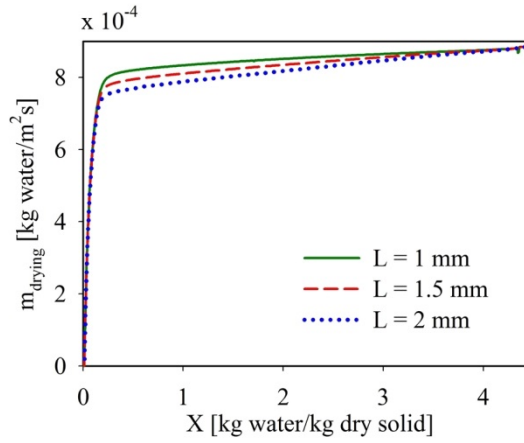


Figure 5.10: Drying flux curve \dot{m}_{drying} vs X for different values of sample thickness. Other parameters used in simulations: $T_{steam} = 180\text{ }^{\circ}\text{C}$, $\dot{M}_{steam} = 0.25\text{ g/min}$, $X_0 = 4.5\text{ kg water/kg dry solid}$ and $L_p = 1000 L_p(20\text{ }^{\circ}\text{C})$.

The evolution of moisture content over time X vs. t and the drying rate curve dX/dt vs. X are presented in Fig. 5.9. Naturally, with an identical initial moisture content, a thick sample results in a longer drying time compared to a thin sample. Since the drying rate dX/dt depends on both drying flux \dot{m}_{drying} and solid mass M_s , i.e. $\frac{dX}{dt} = \frac{\dot{m}_{drying}}{M_s}$, the drying rate dX/dt vs. X obtained for the thick sample which has a higher solid mass is lower compared to the thin sample (c.f. Fig. 5.9b). Therefore, the evolution of drying flux \dot{m}_{drying} over moisture content X obtained with different sample thicknesses is additionally

presented in Fig. 5.10. As can be seen, a lower drying flux is obtained with the thicker sample compared to the thinner one.

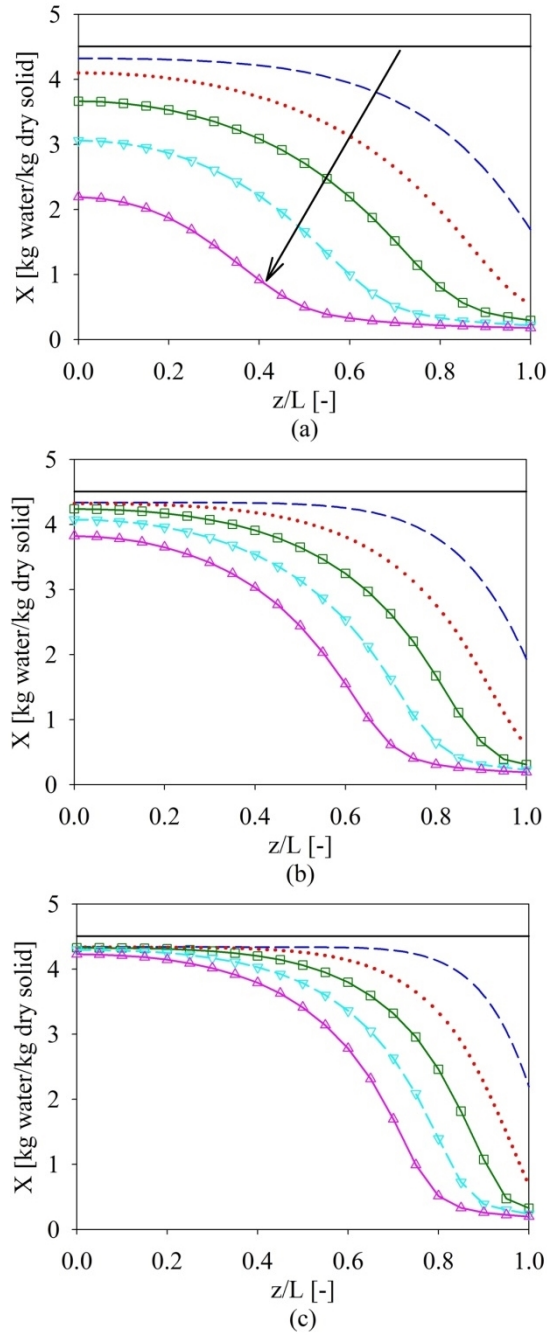


Figure 5.11: Moisture content profiles of the porous medium for different values of sample thickness: (a) $L = 1$ mm, (b) $L = 1.5$ mm and (c) $L = 2$ mm. The evaporative surface of the medium is located at $z/L = 1$. The profiles are plotted for a time period of $t = 10$ min with an interval of 2 min. Other parameters used in simulations are: $T_{steam} = 180$ °C, $\dot{M}_{steam} = 0.25$ g/min, $X_0 = 4.5$ kg water/kg dry solid and $L_p = 1000L_p (20$ °C).

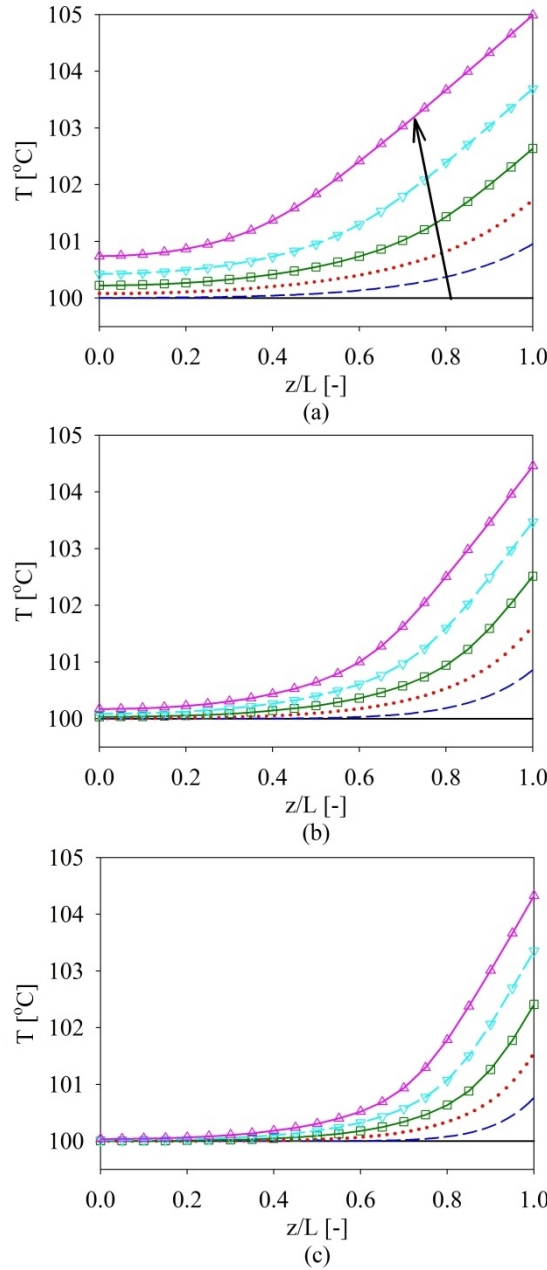


Figure 5.12: Temperature profiles of the porous medium for different values of sample thickness: (a) $L = 1$ mm, (b) $L = 1.5$ mm and (c) $L = 2$ mm. The evaporative surface of the medium is located at $z/L = 1$. The profiles are plotted for a time period of $t = 10$ min with an interval of 2 min. Other parameters used in simulations are: $T_{steam} = 180$ °C, $\dot{M}_{steam} = 0.25$ g/min, $X_0 = 4.5$ kg water/kg dry solid and $L_p = 1000 L_p(20$ °C).

The reason of this lower drying rate is that the moisture at the center of the thick sample is more difficult to be removed since the hydraulic resistance of the vapor and liquid transport in the void space increases with a longer transport distance. This fact results in a sharper temporal moisture content distribution obtained with the thick sample compared to the thin one (c.f. Fig. 5.11). Likewise, less heat conduction is obtained by the dried zone

that appears in the thick sample (c.f. Fig. 5.11c). This low thermal conductivity zone restrains the penetration of thermal energy. It results in a shaper evolution of temporal moisture profiles compared to the thin sample (c.f. Fig. 5.12).

Chapter 6

Conclusions and outlook

6.1 Conclusions

As stated in Chapter 1, this thesis focuses on the liquid-vapor flow in porous media in the presence of thermal effect. Respective transport phenomena may occur in numerous industrial processes but the scope of this work is limited to two cases: evaporation process taking place in a capillary porous wick (a steady-state process) and superheated steam drying of porous media (a transient process). Both discrete pore-scale and continuum approaches are successfully applied to explore the characteristics of these processes. In this chapter, conclusions obtained from the simulation results are drawn.

Considering the evaporation within the capillary porous wick (Chapter 2), a pore network model was developed to simulate the heat and mass transfer in the unsaturated capillary porous wick and to predict the location of the liquid-vapor interface as well as the effective heat transfer coefficient in the dry-out operating regime. The dependence of the thermal properties of the working fluid on both temperature and pressure is taken into account in this model. The model was verified against measurement data available in the literature. Deflation/inflation of the vapor pocket and a fluctuation of the heat transfer coefficient with increasing heat load, which cannot be obtained from continuum simulations, were observed in pore networks with unimodal throat radius distributions. By evaluating Péclet number and the temperature gradient due to viscous heating, both heat transfer by conduction mechanism and viscous dissipation are found to be negligible for the present network configurations. A brief comparative assessment of the effective heat transfer coefficient of porous wicks operating with different types of working fluid was also conducted. The results are in favor of water as the most effective working fluid which

provides higher heat transfer performance compared to methanol or ethanol at high operating temperature. An enhancement of the heat and mass transfer efficiencies of the porous wick can be provided by bi-modal throat radius distribution (by creating vertical macro channels) or by layered structure (fabricated with a thin coarser porous layer above of a finer porous layer). However, if the relative thickness of the coarse layer is too large, then the heat transfer efficiency is reduced again.

Regarding the superheated steam drying process, firstly (Chapter 3), a two-dimensional pore network model was developed to simulate the superheated steam drying (SSD) of a capillary porous medium. Compared to the available literature on non-isothermal pore network models, the internal vapor condensation was fully accounted for by introducing new liquid invasion rules. The tendencies in the evolution of the moisture content and of the temperature over time were found to be in qualitative agreement with earlier experimental and simulation results. The simulated drying kinetics was also verified qualitatively by comparing with experimental data. The surface condensation and evaporation periods of the SSD process are clearly visible in the pore network simulation results. The results favor the wet surface hypothesis [136], which states that the transition point between the CDR and FDR stages is determined by the surface saturation of the porous medium. The numerical results evidence that the implementation of liquid invasion rules into the present model improves the accuracy in the prediction of liquid disintegration. Additionally, the constant drying rate stage obtained by the “condensation fully treated” scheme is typically longer than the one obtained by the “condensation partly treated” scheme. This is due to the better hydraulic connectivity of the liquid phase within the network. However, the difference between the two schemes is insignificant with the present pore network configuration with convective heat transfer, since the condensation rate is very small compared to the drying rate. With other configurations, such as a conductive heat transfer boundary condition at the bottom edge [46] or an imposed positive temperature gradient $dT/dz > 0$ [137], where the condensation rate contributes more significantly, the difference might be more pronounced. Furthermore, the overpressure of the vapor phase within a heterogeneous pore structure, which is the driving force for the vapor flow, is reproduced by the present pore network model. The gas phase pressure and temperature fields indicate that most of the condensing throats/pores are located below the evaporating throats/pores.

In Chapter 4, we proposed a new methodology to determine parameters of the characteristic drying curve (CDC) model for the superheated steam drying (SSD) of a single wood particle. This methodology features an extrapolative prediction of parameter correlations outside of the experimentally accessible range. To generate an accurate set of correlations in a large range of operating conditions, only a limited number of experiments is required, or available experimental data from literature can be used. This methodology

operates as follows: A continuum model that accounts for the spatio-temporal distribution of intraparticle moisture content and of temperature is used. The thermophysical properties such as porosity, thermal conductivity, and specific heat capacity of the wood (or any other) particle, which are essential input parameters of the continuum model, are directly measured. The continuum model is assessed by comparing simulation results with experimental data obtained for single particles by means of, e.g., a magnetic suspension balance. Then, simulations based on the continuum model are performed for a broader range of drying conditions, as they may be encountered in practice. The numerical data obtained from the continuum model is used to establish correlations for parameters appearing in the CDC (or other reduced) model. The results obtained for wood particles indicated that the impact of drying conditions on the critical moisture content X_{cr} and on the drying rate retardation coefficient f was significant. An intensive drying process leads to a high critical moisture content or a short constant drying rate period due to the enhanced external heat flux. The drying rate retardation coefficient f was modeled by a power function of the normalized moisture content X_n with an exponential factor that depends linearly on X_n . Finally, the numerical results obtained from the CDC model were verified by comparing to, in this case available, experimental data as well as to numerical data obtained from the continuum model.

Based on our own continuum-scale model developed for non-deforming porous medium constructed of impermeable solid phase presented in Chapter 4, a non-isothermal continuum-scale model for the superheated steam drying process of a cellular plant material has been developed in Chapter 5. This model accounts for both the fluid transport in the intercellular void space and for the diffusive water flow across the cell walls. To validate the model, superheated steam drying experiments with potato samples were carried out using the magnetic suspension balance. A fairly good agreement between experimental observations and numerical results considering the surface area shrinkage evidences the predictive potential of the proposed model. It has been elucidated that the extracellular moisture evaporates completely in the early stage of the drying process; thereafter, the process is driven by the diffusion of intracellular water towards the extracellular water vapor. Therefore, the water conductivity of the cell membrane strongly impacts the drying characteristics: a uniform spatio-temporal distribution of the moisture content is observed in a porous medium with low cell membrane water conductivity. In such a medium the temperature increases significantly after its extracellular moisture has been removed. By contrast, the temperature of a porous medium with high cell membrane water conductivity remains nearly at the saturation temperature and thus the drying rate remains high during a significant period of the drying process. The sensitivity analysis also indicated that a slower drying process and more uniform temperature and moisture content profiles are obtained with thin sample, compared to thick sample.

6.2 Future research work

In the context of steady state evaporation within the capillary porous wick, microfluidic experiments shall be carried out to validate the simulation results in the future. These measurements shall contribute to the identification of transport mechanisms at the pore level which later on could be incorporated into a pore network model. Following this outlook, an etched glass micro-model has been fabricated by the Institute of Micro- and Sensor-Systems (IMOS), Otto von Guericke University Magdeburg, Germany (c.f. Fig. 6.1). The micro-scale channels were etched in a borofloat glass plate, which is transparent to light, so that the internal liquid flow can be optically observed. An experimental system shown in Fig. 6.1 was developed to investigate the operating behavior of the evaporator. For the application in a loop heat pipe evaporator the current pore network model for the evaporator shall be coupled with models for other loop heat pipe components to simulate their operating characteristics as well as the influence of operating conditions on the heat transfer efficiency of loop heat pipes.

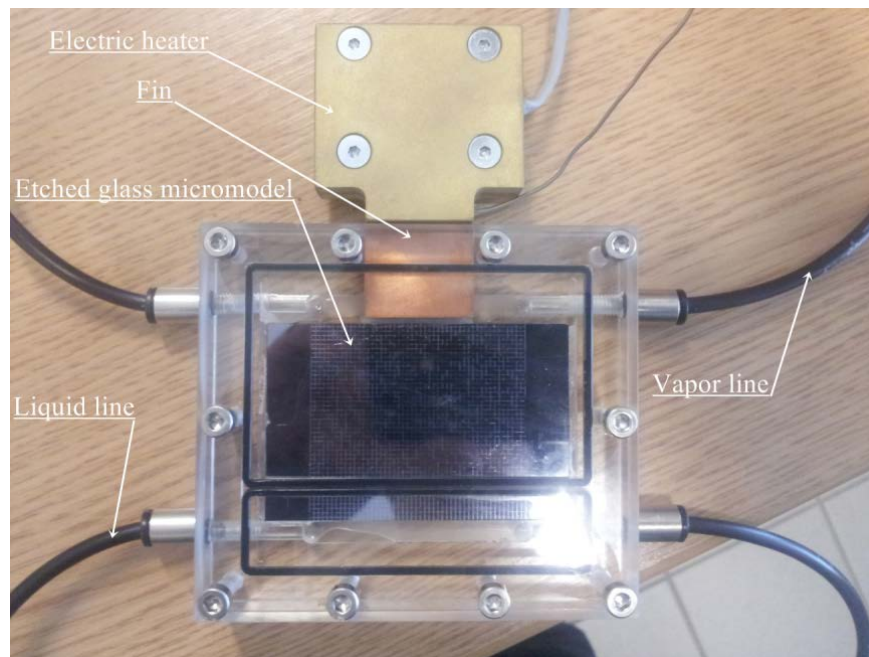


Figure 6.1: Illustration of microfluidic model and other components.

In the frame of superheated steam drying, a three-dimensional non-isothermal pore network model that accounts for viscous liquid flow shall be developed to simulate the SSD process of a capillary porous medium. Liquid viscosity cannot be neglected in several circumstances: fast drying, large porous media, and porous media with a narrow pore size distribution. Such a dynamic pore network model shall be used to explore systematically the influence of pore structure on the phase distributions and drying curves. Several effective macroscopic parameters such as the capillary pressure curve or the relative permeabilities may be obtained from a post-processing of the Monte-Carlo simulation

results. Furthermore, microfluidic experiments shall be carried out to confirm the simulation results and to reveal further pore-scale transport mechanisms that could be incorporated into a future pore network model.

Considering the drying process of plant porous material, in the future, gravimetric experiments shall be carried out to establish a correlation between intracellular water potential and intracellular moisture content at high temperatures for a set of agricultural products including potato. The evolution of sample temperature during the drying process shall be measured; this might be used for further model validation and for numerical estimation of the cell membrane water conductivity. Furthermore, model simplifications such as the absence of water diffusion between neighboring cells should be relaxed in a future advanced model. Under certain circumstances, the methodology proposed in this work can be applied to other drying techniques (e.g., convective hot air drying or vacuum contact drying) or thermal treatment processes (e.g., organic liquid extraction or cooling storage) to provide a better understanding on fluid transport under thermal effects involved in cellular plant porous media.

Following the upscaling strategy, the coupling of internal heat and mass transfer in a porous medium and the interaction between porous domain and the surrounding fluid phase are topics suggested for future studies. The reduction procedure is also suggested for the sophisticated continuous model of the SSD of porous plant materials presented in Chapter 5. The CDC model developed in Chapter 4 for SSD of porous materials structured by impermeable solid phase and the expected lump model for SSD of porous cellular plant materials can be incorporated into any SSD dryer model.

- [1] D.B. Ingham, I.I. Pop, *Transport phenomena in porous media*, 1st ed., Pergamon, Oxford, Danvers, MA, 1998.
- [2] P.S. Hammond, E. Unsal, A dynamic pore network model for oil displacement by wettability-altering surfactant solution, *Transport in Porous Media* 92 (2012) 789–817.
- [3] S.E. Powers, L.M. Abriola, W.J. Weber, An experimental investigation of nonaqueous phase liquid dissolution in saturated subsurface systems: Steady state mass transfer rates, *Water Resources Research* 28 (1992) 2691–2705.
- [4] Y.F. Maydanik, Loop heat pipes, *Applied Thermal Engineering* 25 (2005) 635–657.
- [5] A. Faghri, *Heat pipe science and technology*, Taylor & Francis, Washington, DC, 1995.
- [6] M. Herskowitz, J.M. Smith, Trickle-bed reactors: A review, *AIChE Journal* 29 (1983) 1–18.
- [7] P. Liu, G.-F. Chen, *Porous materials: Processing and applications*, 1st ed., Butterworth-Heinemann, Elsevier, Amsterdam, 2014.
- [8] K. Ishizaki, S. Komarneni, M. Nanko, *Porous materials: Process technology and applications*, Kluwer Academic, Dordrecht, 1998.
- [9] M.E. Davis, Ordered porous materials for emerging applications, *Nature* 417 (2002) 813–821.
- [10] X.S. Zhao, Novel porous materials for emerging applications, *Journal of Materials Chemistry* 16 (2006) 623–625.
- [11] T. Defraeye, Advanced computational modelling for drying processes – A review, *Applied Energy* 131 (2014) 323–344.
- [12] S. Whitaker, Simultaneous heat, mass, and momentum transfer in porous media: A theory of drying, in: Harnett, Irvine (Ed.) 1977 – *Advances in Heat Transfer*, pp. 119–203.
- [13] A.V. Luikov, *Heat and mass transfer in capillary-porous bodies*, 1st ed., Pergamon Press, Oxford, New York, 1966.
- [14] J. Gostick, M. Aghighi, J. Hinebaugh, T. Tranter, M.A. Hoeh, H. Day, B. Spellacy, M.H. Sharqawy, A. Bazylak, A. Burns, W. Lehnert, A. Putz, *OpenPNM: A pore*

- network modeling package, *Computing in Science & Engineering* 18 (2016) 60–74.
- [15] I. Fatt, The pore network model of porous media, *Petroleum Transactions* 207 (1956) 144–181.
- [16] Y. Sun, A. Kharaghani, E. Tsotsas, Micro-model experiments and pore network simulations of liquid imbibition in porous media, *Chemical Engineering Science* 150 (2016) 41–53.
- [17] A.R. Al-Dhahli, S. Geiger, M.I. van Dijke, Three phase pore network modeling for reservoirs with arbitrary wettability, *SPE Journal* 18 (2012) 285–295.
- [18] R. Wu, C.Y. Zhao, E. Tsotsas, A. Kharaghani, Convective drying in thin hydrophobic porous media, *International Journal of Heat and Mass Transfer* 112 (2017) 630–642.
- [19] R. Wu, Q. Liao, X. Zhu, H. Wang, Impacts of the mixed wettability on liquid water and reactant gas transport through the gas diffusion layer of proton exchange membrane fuel cells, *International Journal of Heat and Mass Transfer* 55 (2012) 2581–2589.
- [20] M. Prat, Pore network models for the study of transfer in the porous wick of loop heat pipe, *Heat Pipe Science and Technology* 1 (2010) 129–149.
- [21] M.J. Blunt, B. Bijeljic, H. Dong, O. Gharbi, S. Iglauer, P. Mostaghimi, A. Paluszny, C. Pentland, Pore-scale imaging and modelling, *Advances in Water Resources* 51 (2013) 197–216.
- [22] Y.F. Maydanik, M.A. Chernysheva, V.G. Pastukhov, Review: Loop heat pipes with flat evaporators, *Applied Thermal Engineering* 67 (2014) 294–307.
- [23] B. Siedel, V. Sartre, F. Lefèvre, Literature review: Steady-state modelling of loop heat pipes, *Applied Thermal Engineering* 75 (2015) 709–723.
- [24] C. Figus, Y.L. Bray, S. Bories, M. Prat, Heat and mass transfer with phase change in a porous structure partially heated: Continuum model and pore network simulations, *International Journal of Heat and Mass Transfer* 42 (1999) 2557–2569.
- [25] L. Mottet, T. Coquard, M. Prat, Three dimensional heat and mass transfer in capillary evaporator, *Proceeding of 5th International Conference on Porous Media and Their Applications in Science, Engineering and Industry, Kona, Hawaii* (2014).
- [26] L. Mottet, T. Coquard, M. Prat, Three dimensional liquid and vapour distribution in the wick of capillary evaporators, *International Journal of Heat and Mass Transfer* 83 (2015) 636–651.
- [27] M. Nishikawara, H. Nagano, L. Mottet, M. Prat, Formation of unsaturated regions in the porous wick of a capillary evaporator, *International Journal of Heat and Mass Transfer* 89 (2015) 588–595.
- [28] A.S. Mujumdar, *Handbook of industrial drying*, Fourth edition, CRC Press Inc, New York, 2014.

- [29] S. Jugjai, C. Phothiya, Liquid fuels-fired porous combustor-heater, *Fuel* 86 (2007) 1062–1068.
- [30] Y. Cao, A. Faghri, Conjugate analysis of a flat-plate type evaporator for capillary pumped loops with three-dimensional vapor flow in the groove, *International Journal of Heat and Mass Transfer* 37 (1994) 401–409.
- [31] Y. Cao, A. Faghri, Analytical solutions of flow and heat transfer in a porous structure with partial heating and evaporation on the upper surface, *International Journal of Heat and Mass Transfer* 37 (1994) 1525–1533.
- [32] J. Li, G.P. Peterson, 3D heat transfer analysis in a loop heat pipe evaporator with a fully saturated wick, *International Journal of Heat and Mass Transfer* 54 (2011) 564–574.
- [33] M.A. Chernysheva, Y.F. Maydanik, 3D-model for heat and mass transfer simulation in flat evaporator of copper-water loop heat pipe, *Applied Thermal Engineering* 33-34 (2012) 124–134.
- [34] X. Zhang, X. Li, S. Wang, Three-dimensional simulation on heat transfer in the flat evaporator of miniature loop heat pipe, *International Journal of Thermal Sciences* 54 (2012) 188–198.
- [35] T.S. Zhao, Q. Liao, On capillary-driven flow and phase-change heat transfer in a porous structure heated by a finned surface: Measurements and modeling, *International Journal of Heat and Mass Transfer* 43 (2000) 1141–1155.
- [36] A.S. Demidov, E.S. Yatsenko, Investigation of heat and mass transfer in the evaporation zone of a heat pipe operating by the ‘inverted meniscus’ principle, *International Journal of Heat and Mass Transfer* 37 (1994) 2155–2163.
- [37] T. Kaya, J. Goldak, Numerical analysis of heat and mass transfer in the capillary structure of a loop heat pipe, *International Journal of Heat and Mass Transfer* 49 (2006) 3211–3220.
- [38] R. Boubaker, V. Platel, A. Berges, M. Bancelin, E. Hannezo, Dynamic model of heat and mass transfer in an unsaturated porous wick of capillary pumped loop, *Applied Thermal Engineering* 76 (2015) 1–8.
- [39] C. Ren, Parametric effects on heat transfer in loop heat pipe’s wick, *International Journal of Heat and Mass Transfer* 54 (2011) 3987–3999.
- [40] C. Ren, Q.-S. Wu, M.-B. Hu, Heat transfer with flow and evaporation in loop heat pipe’s wick at low or moderate heat fluxes, *International Journal of Heat and Mass Transfer* 50 (2007) 2296–2308.
- [41] Q. Liao, T.S. Zhao, A visual study of phase-change heat transfer in a two-dimensional porous structure with a partial heating boundary, *International Journal of Heat and Mass Transfer* 43 (2000) 1089–1102.
- [42] Q. Liao, T.S. Zhao, Evaporative heat transfer in a capillary structure heated by a grooved block, *Journal of Thermophysics and Heat Transfer* 13 (1999) 126–133.

- [43] C. Byon, S.J. Kim, Effects of geometrical parameters on the boiling limit of bi-porous wicks, *International Journal of Heat and Mass Transfer* 55 (2012) 7884–7891.
- [44] C. Louriou, M. Prat, Pore network study of bubble growth by vaporization in a porous medium heated laterally, *International Journal of Thermal Sciences* 52 (2012) 8–21.
- [45] V.K. Surasani, T. Metzger, E. Tsotsas, Influence of heating mode on drying behavior of capillary porous media: Pore scale modeling, *Chemical Engineering Science* 63 (2008) 5218–5228.
- [46] E. Tsotsas, H. Martin, Thermal conductivity of packed beds: A review, *Chemical Engineering and Processing* 22 (1987) 19–37.
- [47] W. Wagner, A. Pruß, The IAPWS formulation 1995 for the thermodynamic properties of ordinary water substance for general and scientific use, *Journal of Physical and Chemical Reference Data* 31 (2002) 387–535.
- [48] T. Metzger, E. Tsotsas, M. Prat, Pore network models: A powerful tool to study drying at the pore level and understand the influence of structure on drying kinetics, in: E. Tsotsas, A.S. Mujumdar (Eds.), *Modern drying technology: Computational tools at different scales*, Wiley-VCH, Weinheim, Germany, 2007, pp. 57–102.
- [49] X.L. Cao, P. Cheng, T.S. Zhao, Experimental study of evaporative heat transfer in sintered copper bidispersed wick structures, *Journal of Thermophysics and Heat Transfer* 16 (2002) 547–552.
- [50] R. Boubaker, V. Platel, Vapor pocket behavior inside the porous wick of a capillary pumped loop for terrestrial application, *Applied Thermal Engineering* 84 (2015) 420–428.
- [51] J. Zhu, Q. Wang, X. Lu, Status and developments of drying low rank coal with superheated steam in China, *Drying Technology* 33 (2015) 1086–1100.
- [52] H.C. van Deventer, Feasibility of energy efficient steam drying of paper and textile including process integration, *Applied Thermal Engineering* 17 (1997) 1035–1041.
- [53] H. Romdhana, C. Bonazzi, M. Esteban-Decloux, Superheated steam drying: An overview of pilot and industrial dryers with a focus on energy efficiency, *Drying Technology* 33 (2015) 1255–1274.
- [54] H. Iyota, N. Nishimura, M. Yoshida, T. Nomura, Simulation of superheated steam drying considering initial steam condensation, *Drying Technology* 19 (2001) 1425–1440.
- [55] I. Hamawand, Drying steps under superheated steam: A review and modeling, *Energy and Environment Research* 3 (2013).
- [56] Z. Chen, W. Wu, P.K. Agarwal, Steam-drying of coal. Part 1. Modeling the behavior of a single particle, *Fuel* 79 (2000) 961–974.

- [57] A. Looi, Drying kinetics of single porous particles in superheated steam under pressure, *Chemical Engineering Journal* 87 (2002) 329–338.
- [58] Z. Pakowski, R. Adamski, S. Kwapisz, Effective diffusivity of moisture in low rank coal during superheated steam drying at atmospheric pressure, *Chemical and Process Engineering* 33 (2012).
- [59] P. Sa-adchom, T. Swasdisevi, A. Nathakaranakule, S. Soponronnarit, Mathematical model of pork slice drying using superheated steam, *Journal of Food Engineering* 104 (2011) 499–507.
- [60] S. Kittiworrawatt, S. Devahastin, Improvement of a mathematical model for low-pressure superheated steam drying of a biomaterial, *Chemical Engineering Science* 64 (2009) 2644–2650.
- [61] P. Suvarnakuta, S. Devahastin, A.S. Mujumdar, A mathematical model for low-pressure superheated steam drying of a biomaterial, *Chemical Engineering and Processing* 46 (2007) 675–683.
- [62] J. Hager, M. Hermansson, R. Wimmerstedt, Modelling steam drying of a single porous ceramic sphere: Experiments and simulations, *Chemical Engineering Science* 52 (1997) 1253–1264.
- [63] J. Hager, R. Wimmerstedt, S. Whitaker, Steam drying a bed of porous spheres: Theory and experiment, *Chemical Engineering Science* 55 (2000) 1675–1698.
- [64] S. Messai, J. Sghaier, M. El Ganaoui, L. Chrusciel, S. Gabsi, Low-pressure superheated steam drying of a porous media, *Drying Technology* 33 (2014) 103–110.
- [65] J. Sghaier, S. Messai, A. Belghith, Superheated steam and humid air drying of a packed bed of porous particles: Theoretical study, *International Journal of Heat and Technology* 26 (2008) 77–84.
- [66] M.J. Blunt, M.D. Jackson, M. Piri, P.H. Valvatne, Detailed physics, predictive capabilities and macroscopic consequences for pore-network models of multiphase flow, *Advances in Water Resources* 25 (2002) 1069–1089.
- [67] M. Prat, Recent advances in pore-scale models for drying of porous media, *Chemical Engineering Journal* 86 (2002) 153–164.
- [68] V. Joekar-Niasar, S.M. Hassanizadeh, Analysis of fundamentals of two-phase flow in porous media using dynamic pore-network models: A review, *Critical Reviews in Environmental Science and Technology* 42 (2012) 1895–1976.
- [69] M. Sahimi, *Flow and transport in porous media and fractured rock: From classical methods to modern approaches*, 2nd ed., Wiley-VCH, Weinheim, 2011.
- [70] T.W. Patzek, Verification of a complete pore network simulator of drainage and imbibition, *SPE Journal* 6 (2013) 144–156.

- [71] K.H. Le, A. Kharaghani, C. Kirsch, E. Tsotsas, Pore network simulations of heat and mass transfer inside an unsaturated capillary porous wick in the dry-out regime, *Transport in Porous Media* 114 (2016) 623–648.
- [72] D. Wilkinson, J.F. Willemsen, Invasion percolation: A new form of percolation theory, *Journal of Physics A: Mathematical and General* 16 (1983) 3365–3376.
- [73] V.K. Surasani, T. Metzger, E. Tsotsas, Consideration of heat transfer in pore network modelling of convective drying, *International Journal of Heat and Mass Transfer* 51 (2008) 2506–2518.
- [74] F. Plourde, M. Prat, Pore network simulations of drying of capillary porous media. Influence of thermal gradients, *International Journal of Heat and Mass Transfer* 46 (2003) 1293–1307.
- [75] S. Taslimi Taleghani, M. Dadvar, Two dimensional pore network modelling and simulation of non-isothermal drying by the inclusion of viscous effects, *International Journal of Multiphase Flow* 62 (2014) 37–44.
- [76] V.K. Surasani, T. Metzger, E. Tsotsas, Drying simulations of various 3D pore structures by a nonisothermal pore network model, *Drying Technology* 28 (2010) 615–623.
- [77] I.W. Eames, N.J. Marr, H. Sabir, The evaporation coefficient of water: A review, *International Journal of Heat and Mass Transfer* 40 (1997) 2963–2973.
- [78] M. Ghiaasiaan, *Gas-liquid two-phase flow: Boiling and condensation in conventional, mini and micro systems*, Cambridge University Press, New York, 2007.
- [79] G.M. Pound, Selected values of evaporation and condensation coefficients for simple substances, *Journal of Physical and Chemical Reference Data* 1 (1972) 135.
- [80] T.L. Bergman, A. Lavine, F.P. Incropera, D.P. DeWitt, *Introduction to heat transfer*, 6th ed., Wiley, Hoboken, NJ, 2011.
- [81] A. Al-Futaisi, T.W. Patzek, Extension of Hoshen–Kopelman algorithm to non-lattice environments, *Physica A: Statistical Mechanics and its Applications* 321 (2003) 665–678.
- [82] T. Metzger, A. Irawan, E. Tsotsas, Remarks on the paper “Extension of Hoshen–Kopelman algorithm to non-lattice environments” by A. Al-Futaisi and T.W. Patzek, *Physica A* 321 (2003) 665–678, *Physica A: Statistical Mechanics and its Applications* 363 (2006) 558–560.
- [83] N.B. Vargaftik, B.N. Volkov, L.D. Voljak, International tables of the surface tension of water, *Journal of Physical and Chemical Reference Data* 12 (1983) 817–820.
- [84] M.W. Woo, D. Stokie, W.L. Choo, S. Bhattacharya, Master curve behaviour in superheated steam drying of small porous particles, *Applied Thermal Engineering* 52 (2013) 460–467.

- [85] T. Metzger, A. Irawan, E. Tsotsas, Isothermal drying of pore networks: Influence of friction for different pore structures, *Drying Technology* 25 (2007) 49–57.
- [86] S. Devahastin, P. Suvarnakuta, S. Soponronnarit, A.S. Mujumdar, A comparative study of low-pressure superheated steam and vacuum drying of a heat-sensitive material, *Drying Technology* 22 (2004) 1845–1867.
- [87] A. Johansson, C. Fyhr, A. Rasmuson, High temperature convective drying of wood chips with air and superheated steam, *International Journal of Heat and Mass Transfer* 40 (1997) 2843–2858.
- [88] A.L. Redman, H. Bailleres, P. Perré, E. Carr, I. Turner, A relevant and robust vacuum-drying model applied to hardwoods, *Wood Science and Technology* 34 (2017) 1143.
- [89] X.-J. Li, B.-G. Zhang, W.-J. Li, Microwave-vacuum drying of wood: Model formulation and verification, *Drying Technology* 26 (2008) 1382–1387.
- [90] A.L. Redman, Evaluation of super-heated steam vacuum drying viability and development of a predictive drying model for four Australian hardwood species, *Forest & Wood Products Australia Limited*, Melbourne, 2011.
- [91] J. Ratnasingam, R. Grohmann, Superheated steam application to optimize the kiln drying of rubberwood (*Hevea brasiliensis*), *European Journal of Wood and Wood Products* 73 (2015) 407–409.
- [92] M. Defo, Y. Fortin, A. Cloutier, Modeling superheated steam vacuum drying of wood, *Drying Technology* 22 (2004) 2231–2253.
- [93] S. Pang, H. Pearson, Experimental investigation and practical application of superheated steam drying technology for softwood Timber, *Drying Technology* 22 (2004) 2079–2094.
- [94] R. Yamsaengsung, S. Tabtiang, Hybrid drying of rubberwood using superheated steam and hot air in a pilot-scale, *Drying Technology* 29 (2011) 1170–1178.
- [95] M.N. Haque, R. Sargent, Standard and superheated steam schedules for radiata pine single-board drying: Model prediction and actual measurements, *Drying Technology* 26 (2008) 186–191.
- [96] Y. Bao, Y. Zhou, Comparative study of moisture absorption and dimensional stability of Chinese cedar wood with conventional drying and superheated steam drying, *Drying Technology* 35 (2016) 860–866.
- [97] P. Perré, The proper use of mass diffusion equations in drying modeling: Introducing the drying intensity number, *Drying Technology* 33 (2015) 1949–1962.
- [98] R. Adamski, Z. Pakowski, Identification of effective diffusivities in anisotropic material of pine wood during drying with superheated steam, *Drying Technology* 31 (2013) 264–268.
- [99] C. Taechapiroj, S. Prachayawarakorn, S. Soponronnarit, Characteristics of rice dried in superheated-steam fluidized-bed, *Drying Technology* 22 (2004) 719–743.

- [100] C. Pronyk, S. Cenkowski, W.E. Muir, Drying foodstuffs with superheated steam, *Drying Technology* 22 (2004) 899–916.
- [101] S. Prachayawarakorn, P. Prachayawasin, S. Soponronnarit, Effective diffusivity and kinetics of urease inactivation and color change during processing of soybeans with superheated-steam fluidized bed, *Drying Technology* 22 (2004) 2095–2118.
- [102] P. Perré, Multiscale modeling of drying as a powerful extension of the macroscopic approach: Application to solid wood and biomass processing, *Drying Technology* 28 (2010) 944–959.
- [103] P. Perré, F. Pierre, J. Casalinho, M. Ayouz, Determination of the mass diffusion coefficient based on the relative humidity measured at the back face of the sample during unsteady regimes, *Drying Technology* 33 (2015) 1068–1075.
- [104] C. Fyhr, A. Rasmuson, Mathematical model of steam drying of wood chips and other hygroscopic porous media, *AIChE Journal* 42 (1996) 2491–2502.
- [105] T.T.H. Tran, M. Jaskulski, E. Tsotsas, Reduction of a model for single droplet drying and application to CFD of skim milk spray drying, *Drying Technology* (2017) 1571–1583.
- [106] M.W. Woo, W.R.W. Daud, A.S. Mujumdar, M.Z.M. Talib, W.Z. Hua, S.M. Tasirin, Comparative study of droplet drying models for CFD modelling, *Chemical Engineering Research and Design* 86 (2008) 1038–1048.
- [107] K.H. Le, A. Kharaghani, C. Kirsch, E. Tsotsas, Discrete pore network modeling of superheated steam drying, *Drying Technology* 35 (2017) 1584–1601.
- [108] J.C. Slattery, Flow of viscoelastic fluids through porous media, in: *Symposium on Mechanics of Rheologically Complex Fluids*, Society of Petroleum Engineers, 2013.
- [109] H.T. Vu, Influence of pore size distribution on drying behavior of porous media by a continuous model, PhD Dissertation, Otto von Guericke University Magdeburg, 2006.
- [110] J.M. Smith, H.C. van Ness, M.M. Abbott, *Introduction to chemical engineering thermodynamics*, 7th ed., McGraw-Hill, Boston, 2005.
- [111] Y. Komatsu, A. Sciazko, M. Zakrzewski, S. Kimijima, A. Hashimoto, S. Kaneko, J.S. Szmyd, An experimental investigation on the drying kinetics of a single coarse particle of Belchatow lignite in an atmospheric superheated steam condition, *Fuel Processing Technology* 131 (2015) 356–369.
- [112] R.B. Keey, *Drying principles and practice*, 1st ed., Pergamon Press, Oxford, New York, 1972.
- [113] B. Krupińska, I. Strømmen, Z. Pakowski, T.M. Eikevik, Modeling of sorption isotherms of various kinds of wood at different temperature conditions, *Drying Technology* 25 (2007) 1463–1470.

- [114] F. Sondej, A. Bück, K. Koslowsky, P. Bachmann, M. Jacob, E. Tsotsas, Investigation of coating layer morphology by micro-computed X-ray tomography, *Powder Technology* 273 (2015) 165–175.
- [115] R. Pashminehazar, A. Kharaghani, E. Tsotsas, Three dimensional characterization of morphology and internal structure of soft material agglomerates produced in spray fluidized bed by X-ray tomography, *Powder Technology* 300 (2016) 46–60.
- [116] W. Kwapinski, E. Tsotsas, Characterization of particulate materials in respect to drying, *Drying Technology* 24 (2006) 1083–1092.
- [117] W. Kwapinski, E. Tsotsas, Determination of kinetics and equilibria for adsorption of water vapor on single zeolite particles by a magnetic suspension balance, *Chemical Engineering & Technology* 27 (2004) 681–686.
- [118] M. Peglow, T. Metzger, G. Lee, R. Hampel, S. Heinrich, E. Tsotsas, Measurement of average moisture content and drying kinetics for single particles, droplets and dryers, in: E. Tsotsas, A.S. Mujumdar (Eds.), *Modern Drying Technology: Experimental techniques*, Wiley-VCH, Weinheim, 2009.
- [119] J.F. Bond, R.H. Crotofino, A.R.P. van Heiningen, W.J.M. Douglas, An experimental study of the falling rate period of superheated steam impingement drying, *Drying Technology* 10 (1992) 961–977.
- [120] T. Defraeye, A. Radu, D. Derome, Recent advances in drying at interfaces of biomaterials, *Drying Technology* 34 (2016) 1904–1925.
- [121] A. Halder, A.K. Datta, R.M. Spanswick, Water transport in cellular tissues during thermal processing, *AIChE Journal* 57 (2011) 2574–2588.
- [122] B. Xiao, J. Chang, X. Huang, X. Liu, A moisture transfer model for isothermal drying of plant cellular materials based on the pore network approach, *Drying Technology* 32 (2014) 1071–1081.
- [123] A. Caixeta, R. Moreira, M. Castell-Perez, Impingement drying of potato chips, *Journal of Food Process Engineering* 25 (2002) 63–90.
- [124] M. Jalili, A. Anca-Couce, N. Zobel, On the uncertainty of a mathematical model for drying of a wood particle, *Energy Fuels* 27 (2013) 6705–6717.
- [125] J. Eriksson, H. Johansson, J. Danvind, A mass transport model for drying wood under isothermal conditions, *Drying Technology* 25 (2007) 433–439.
- [126] L. Li, Numerical simulation of mass transfer during the osmotic dehydration of biological tissues, *Computational Materials Science* 35 (2006) 75–83.
- [127] G.H. Crapiste, S. Whitaker, E. Rotstein, Drying of cellular material—I. A mass transfer theory, *Chemical Engineering Science* 43 (1988) 2919–2928.
- [128] P.S. Nobel, *Physicochemical and environmental plant physiology*, 4th ed., Academic Press, Amsterdam, Boston, 2009.
- [129] VDI-Gesellschaft Verfahrenstechnik und Chemieingenieurwesen, *VDI Heat Atlas*, 2nd ed., Springer, Berlin, 2010.

- [130] S.V. Patankar, Numerical heat transfer and fluid flow, Hemisphere Publ. Corporation, Washington, New York, 1980.
- [131] P.P. Tripathy, S. Kumar, Modeling of heat transfer and energy analysis of potato slices and cylinders during solar drying, *Applied Thermal Engineering* 29 (2009) 884–891.
- [132] A.N. Califano, A. Calvelo, Thermal conductivity of potato between 50 and 100°C, *Journal of Food Science* 56 (1991) 586–587.
- [133] Y. Liu, W. Zhu, L. Luo, X. Li, H. Yu, A mathematical model for vacuum far-infrared drying of potato slices, *Drying Technology* 32 (2013) 180–189.
- [134] H. Iyota, N. Nishimura, T. Onuma, T. Nomura, Drying of sliced raw potatoes in superheated steam and hot air, *Drying Technology* 19 (2001) 1411–1424.
- [135] E.-U. Schlünder, Drying of porous material during the constant and the falling rate period: A critical review of existing hypotheses, *Drying Technology* 22 (2004) 1517–1532.
- [136] N. Vorhauer, T. Metzger, E. Tsotsas, On the influence of temperature gradients on drying of pore networks, in: *Proceedings of European Drying Conference*, October 26-28, 2011.
- [137] G.L. Morini, Viscous heating in liquid flows in micro-channels, *International Journal of Heat and Mass Transfer* 48 (2005) 3637–3647.
- [138] D. Han, K.-J. Lee, Viscous dissipation in micro-channels, *Journal of Mechanical Science and Technology* 21 (2007) 2244–2249.

A Thermal properties of water

Table A.1: Thermal properties of water at 100 °C used in the continuum-scale simulations presented in Sec. 4.5 and Sec. 5.4.

Parameter	Value/Equation
Vapor specific heat capacity, $c_{p,v}$ [130]	2.077 kJ/kgK at 100 °C
Liquid specific heat capacity, $c_{p,l}$ [130]	4.217 kJ/kgK at 100 °C
Vapor density, ρ_v [130]	$0.598 \frac{p_v}{p_{v,sat}(100\text{ }^\circ\text{C})} \frac{373.15}{(T[^\circ\text{C}] + 273.15)} \text{ kg/m}^3$
Liquid density, ρ_l [130]	958.35 kg/m ³ at 100 °C
Vapor dynamic viscosity, μ_v [130]	12.23×10^{-6} Pa s at 100 °C
Liquid dynamic viscosity, μ_l [130]	281.6×10^{-6} Pa s at 100 °C
Liquid thermal conductivity, λ_l [130]	0.68 W/mK at 100 °C
Saturated vapor pressure, $p_{v,sat}$ [130]	$p_{v,sat}(T[^\circ\text{C}]) = \exp\left(23.462 - \frac{3978.205}{233.349 + T}\right) \text{ Pa}$
Evaporation enthalpy, Δh_{evp} [130]	$\Delta h_{evp}(T_{ref}) = 2500 \text{ kJ/kg}$ at $T_{ref} = 0 \text{ }^\circ\text{C}$
Surface tension, σ [110]	$\sigma(T[^\circ\text{C}]) = 1.310^{-7} T^2 - 1.5810^{-4} T + 0.076 \text{ N/m}$

B Influence of convergence parameter on the vapor pocket pattern and on the computation time

As stated in Sec. 2.3.5, a convergence criterion parameter of $\zeta = 0.01$ was chosen as a compromise between the computational time and the accuracy of results. In this Appendix, the influence of convergence parameter ζ on the vapor pocket pattern and on the computation time is explored to confirm this compromise. The pore network simulations are performed for four different values of the convergence parameter ζ . All other parameters used in the simulations are given in Table 3.2. Figure B.1 shows the dependency of the normalized computation time τ and of the vapor area fraction f_v on the values of ζ . The normalized time is defined as the ratio of the time required for the simulation with a given value of ζ to the simulation time with $\zeta = 0.00$, which varies from 4 to 7 hours depending on throat size distribution. Due to less iterations for a larger value of ζ , the computation time can be reduced by about 10% by increasing ζ from 0.00 to 0.01. Since the results obtained for these two values of ζ do not deviate too much, $\zeta = 0.01$ is chosen for all simulations presented in this study. As can also be seen, the vapor pocket patterns obtained for the values of $\zeta = 0.00$ and 0.01 differ only very slightly.

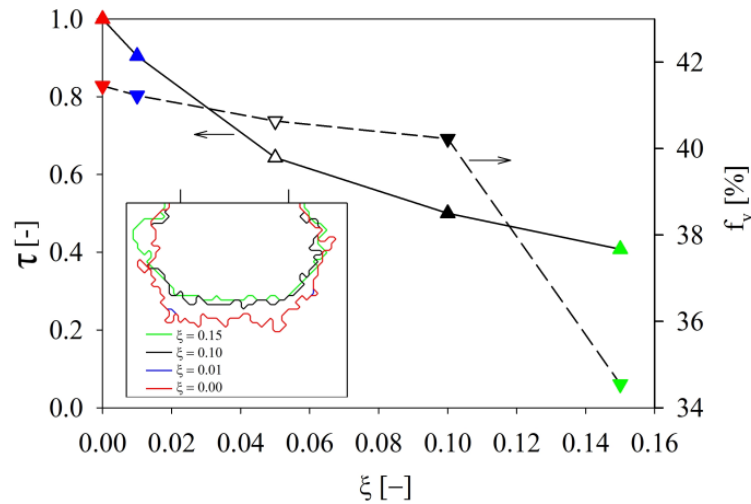


Figure B.1: Influence of convergence parameter ζ on the vapor area fraction and on the normalized computation time τ . The inset figure shows the vapor pocket patterns obtained from simulations with different values of ζ .

C Contribution of convective heat transfer and viscous dissipation on energy conservation

To develop the pore network model of the loop heat pipe evaporator, several simplifications were made. One of these simplifications is that the convective heat transfer and the viscous dissipation are assumed to be negligible. In this Appendix, an investigation is made to examine the validity of these simplifications. The simulations are performed with water as the working fluid and with the input parameters stated in Table 2.1. From the pressure and phase distributions, the mass flow rate \dot{M}_{ij} in each throat is calculated by Eq.

2.1. The fluid interstitial velocity in each throat is computed as

$$v_{0,ij} = \frac{\dot{M}_{ij}}{\rho_f \pi r_{ij}^2}. \quad (\text{C.1})$$

With the transfer area between two neighboring pores $A_{cv, ij} = WL$, the superficial velocity v_{ij} is calculated by

$$v_{ij} = \frac{v_{0,ij} \pi r_{ij}^2}{WL}. \quad (\text{C.2})$$

To evaluate the contribution of heat transported by convection to the total heat flux, the Péclet number Pe , which is a dimensionless value representing the ratio between convective heat transfer and conductive heat transfer is used

$$Pe = \frac{\text{convective heat flux}}{\text{conductive heat flux}} \approx \frac{v \rho_f c_{p,f}}{\lambda_{\text{eff}} / L}. \quad (\text{C.3})$$

The superficial velocity used in this calculation is the average value for the vapor and liquid regions. The evolution of the Péclet number in vapor and liquid regions for different values of the heat load \dot{q} is presented in Fig. C.1. As can be seen, the Péclet number in both vapor and liquid regions is very small (lower than 0.002). This implies that the convective heat transfer is very small (approximately 0.2%) compared to the conductive heat transfer, and thus the heat transported by convection is negligible in the heat flux calculations with the network configurations used in these simulations. This result also indicates that with wicks composed of non-insulating solid materials, i.e. $\lambda_s > 1$ W/mK, the heat transported by convection can be neglected (lower than 2%). However, in the case of a solid skeleton made by low thermal conductivity material such as a polymer or plastic (for which the thermal conductivity varies from 0.5 to 0.2 W/mK), the contribution of the convective heat transfer to the total heat flux is significant and this term should be considered in a more comprehensive pore network model.

In viscous flow, the mechanical energy is converted into thermal energy by viscous dissipation; thus, the temperature of the fluid increases. Morini [138], Han and Lee [139] proposed an equation to compute the fluid temperature gradient along a smooth cylindrical throat due to the viscous heating as follows:

$$\frac{dT}{dL} = \frac{8v_o v_f}{c_{p,f} r_t^2}. \quad (C.4)$$

The computational results are presented in Fig. C.2. The temperature gradient in the vapor flow is significantly higher than in the liquid flow because of the higher kinematic viscosity and lower density. The temperature gradient in vapor throats varies from 0.63 K/m to 11.61 K/m in a heat load range from $\dot{q} = 20 \text{ kW/m}^2$ to $\dot{q} = 140 \text{ kW/m}^2$. The maximum increase of the vapor temperature (for a heat load of $\dot{q} = 140 \text{ kW/m}^2$) due to the viscous heating in a throat with length of $L_t = 1 \text{ mm}$ and $L_y = 44 \text{ mm}$ is 0.011 K and 0.51 K, respectively. These temperature differences are extremely small compared to the fin superheat value (164.32 K) at these operating conditions. Therefore, the influence of viscous dissipation on the fluid flow is truly negligible in the pore network configurations used in this study.

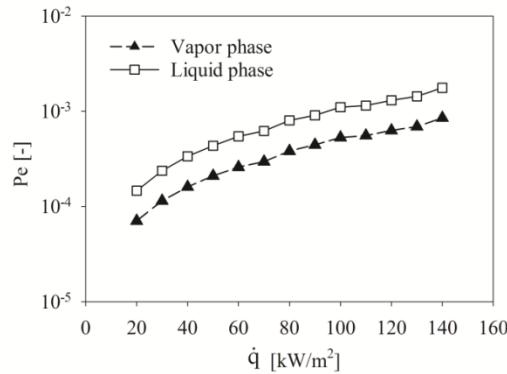


Figure C.1: Variation of averaged Péclet number for different values of heat load \dot{q} .

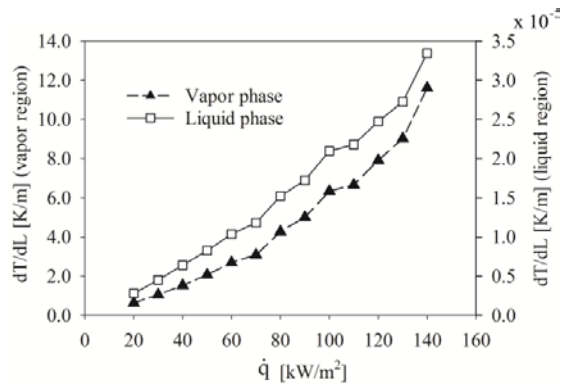


Figure C.2: Variation of temperature gradient due to viscous heating for different values of heat load \dot{q} .

D Experimental data obtained from single wood particle drying

The superheated steam drying experiments on single wood particles were performed by Dr.-Ing. Neli Hampel in the frame of IGF project no. 18971 BR/1 funded by Forschungsgesellschaft Verfahrens-Technik (GVT). The experiments were performed for single particles with a mean diameter of 6.3 mm, at a steam velocity of 0.015 m/s and four different temperatures (120 °C, 140 °C, 160 °C and 180 °C). This data is used to assess the continuum and characteristic drying curve models developed in Chapter 4, i.e. Figs. 4.7 and 4.12.

Table D.1: Evolution of wood particle mass during SSD drying at $T_{steam} = 120$ °C.

Time (min)	Drying chamber temperature (°C)	Sample mass (g)	Time (min)	Drying chamber temperature (°C)	Sample mass (g)
0.00	119.33	0.149112	30.08	119.67	0.104538
1.00	119.46	0.160717	31.06	119.69	0.103022
2.00	119.57	0.158388	32.06	119.85	0.101788
3.00	119.72	0.156035	33.06	120.02	0.100329
4.00	119.83	0.153745	34.06	120.18	0.099118
5.00	119.95	0.151470	35.08	120.28	0.097746
6.00	119.91	0.148907	36.06	120.38	0.096564
7.00	119.93	0.146622	37.07	120.36	0.095471
8.07	119.95	0.144148	38.31	120.45	0.094145
9.07	119.96	0.141800	38.98	120.40	0.093606
10.07	119.95	0.139629	39.98	120.40	0.092745
11.07	119.95	0.137521	40.98	120.42	0.092086
12.07	119.92	0.135611	41.98	120.36	0.091533
13.07	119.93	0.133710	42.98	120.34	0.091079
14.07	119.93	0.131922	44.98	120.31	0.090393
15.07	119.93	0.129911	45.98	120.29	0.090144
16.07	119.94	0.128183	46.98	120.28	0.089962
17.07	119.92	0.126197	48.41	120.25	0.089749
18.15	119.88	0.124291	49.08	120.23	0.089680
18.98	119.87	0.122751	50.08	120.20	0.089591
19.98	119.85	0.120916	51.08	120.19	0.089520
21.00	119.82	0.119209	52.08	120.16	0.089463
21.98	119.81	0.117503	53.08	120.16	0.089414
22.98	119.81	0.115858	54.08	120.16	0.089384
23.99	119.81	0.114182	55.08	120.15	0.089350
24.99	119.80	0.112509	56.08	120.10	0.089330
26.00	119.72	0.110744	57.08	120.07	0.089313
26.99	119.72	0.109319	58.49	120.06	0.089291
28.23	119.70	0.107334	59.01	120.06	0.089279
29.06	119.68	0.106150	59.99	120.03	0.089271

Table D.2: Evolution of wood particle mass during SSD drying at $T_{steam} = 140$ °C.

Time (min)	Drying chamber temperature (°C)	Sample mass (g)
0.00	140.24	0.139847
1.00	139.94	0.147233
2.00	140.13	0.142824
3.00	140.21	0.138216
3.93	140.28	0.134210
4.93	140.28	0.130361
5.93	140.33	0.126824
6.93	140.31	0.123204
8.17	140.34	0.118910
9.29	140.33	0.114924
10.01	140.34	0.112581
10.93	140.39	0.109463
11.93	140.37	0.106246
12.93	140.42	0.103138
13.93	140.41	0.099945
14.93	140.43	0.096939
15.93	140.43	0.096586
16.93	140.43	0.093632
18.34	140.44	0.091867
19.01	140.47	0.090175
20.01	140.45	0.086288
21.01	140.47	0.084665
22.01	140.49	0.083393
23.01	140.49	0.082529

Time (min)	Drying chamber temperature (°C)	Sample mass (g)
24.01	140.49	0.082021
25.01	140.51	0.081654
26.01	140.54	0.081423
27.01	140.54	0.081279
28.42	140.55	0.081216
29.09	140.53	0.081168
30.09	140.55	0.081092
31.09	140.51	0.081058
32.09	140.58	0.081048
33.09	140.56	0.081035
34.09	140.58	0.081021
35.09	140.53	0.081012
36.09	140.55	0.080999
37.09	140.55	0.080994
38.52	140.55	0.080991
39.02	140.55	0.080989
40.04	140.53	0.080969
41.02	140.55	0.080962
42.02	140.54	0.080952
43.02	140.55	0.080949
44.02	140.55	0.080949
45.04	140.50	0.080940
46.02	140.52	0.080941
47.02	140.55	0.080942

Table D.3: Evolution of wood particle mass during SSD drying at $T_{steam} = 160$ °C.

Time (min)	Drying chamber temperature (°C)	Sample mass (g)
0.00	159.91	0.160481
1.00	159.67	0.168793
2.00	159.81	0.161881
3.00	159.55	0.154830
4.02	159.33	0.148214
5.00	159.31	0.142885
6.00	159.28	0.137036
7.57	159.41	0.128722
8.09	159.44	0.126226
9.07	159.56	0.121261
10.07	159.65	0.116343
11.07	159.73	0.111613
12.07	159.80	0.107674
13.09	159.90	0.103610
14.08	160.01	0.100279
15.08	160.05	0.097745
16.08	160.15	0.096092
17.65	160.23	0.094768
17.99	160.25	0.094591
18.99	160.33	0.094277
19.99	160.36	0.094117
21.03	160.43	0.094003
22.03	160.55	0.093962
23.03	160.56	0.093930
24.03	160.62	0.093904
25.03	160.64	0.093888
26.03	160.70	0.093871
26.87	160.67	0.093859
28.11	160.72	0.093845
28.95	160.75	0.093841
29.95	160.63	0.093837
30.95	160.43	0.093834
31.95	160.26	0.093830
32.96	160.15	0.093836
33.95	160.01	0.093837
34.95	159.90	0.093838
35.95	159.84	0.093836
36.95	159.83	0.093832

Table D.4: Evolution of wood particle mass during SSD drying at $T_{steam} = 180$ °C.

Time (min)	Drying chamber temperature (°C)	Sample mass (g)
0.00	179.44	0.150169
1.00	178.77	0.154996
2.00	179.31	0.146436
3.00	179.66	0.137588
4.00	179.81	0.130364
5.00	179.81	0.123256
6.00	179.77	0.116350
7.00	179.71	0.110211
8.07	179.64	0.103690
9.07	179.58	0.098037
10.07	179.57	0.093280
11.07	179.53	0.089622
12.07	179.51	0.087660
13.07	179.54	0.086801
14.07	179.53	0.086397
15.07	179.52	0.086229
16.08	179.50	0.086153
17.08	179.49	0.086111
18.15	179.48	0.086094
18.99	179.48	0.086078
19.99	179.46	0.086068
21.00	179.39	0.086059
21.99	179.41	0.086045
22.99	179.40	0.086033
23.99	179.37	0.086027
24.99	179.33	0.086018
26.00	179.30	0.086010
26.99	179.28	0.086002
28.23	179.25	0.086005
29.06	179.21	0.085996
30.08	179.19	0.085992
31.06	179.18	0.085988
32.06	179.17	0.085983
33.06	179.11	0.085978
34.06	179.06	0.085970
35.08	179.05	0.085963
36.06	179.07	0.085957
37.06	179.08	0.085953
38.31	179.06	0.085947
38.98	179.05	0.085946
39.98	178.99	0.085940

E Experimental data obtained from potato sample drying

The superheated steam drying experiments of potato samples were performed with the help of M.Sc. Saeedeh Imani Moqadam. The experiments were performed for potato samples with a mean thickness of 2 mm, at a steam mass flow rate of 0.25 g/min and three different temperatures (160 °C, 180 °C and 200 °C). The experiments were repeated three times denoted as Exp. 1, Exp. 2 and Exp. 3 at each temperature. This experimental data is used to validate the continuum models developed in Chapter 5, i.e. Fig. 5.4.

Table E.1: Evolution of potato sample mass during SSD drying at $T_{steam} = 160$ °C (Exp. 1).

Time (min)	Drying chamber temperature (°C)	Sample mass (g)
0.00	159.00	0.146804
1.00	159.22	0.160231
2.00	159.48	0.153696
3.00	159.70	0.145939
4.00	159.78	0.138668
4.83	159.79	0.132318
6.08	159.80	0.123034
7.08	159.78	0.116004
8.08	159.79	0.108746
9.08	159.74	0.101762
10.08	159.74	0.095112
11.08	159.71	0.088563
12.08	159.71	0.082476
13.08	159.66	0.076183
14.08	159.66	0.070451
15.99	159.70	0.059947
17.01	159.72	0.054765
17.99	159.70	0.050318
18.99	159.69	0.046154
19.99	159.67	0.042233
20.99	159.65	0.038510
22.01	159.65	0.035167
22.99	159.63	0.032400
23.99	159.63	0.029785
24.99	159.58	0.027813
26.08	159.59	0.026794
27.07	159.59	0.026346
28.07	159.56	0.026098
29.07	159.58	0.025921
30.07	159.57	0.02579
31.09	159.59	0.025707
32.07	159.55	0.025642
33.07	159.56	0.025591
34.07	159.52	0.025553
35.07	159.5	0.025515

Table E.2: Evolution of potato sample mass during SSD drying at $T_{steam} = 160$ °C (Exp. 2).

Time (min)	Drying chamber temperature (°C)	Sample mass (g)
0.00	159.12	0.153662
1.00	159.45	0.165128
2.00	159.76	0.158182
3.00	159.99	0.150511
3.84	160.05	0.144658
5.08	160.11	0.135785
6.08	160.11	0.129018
7.08	160.08	0.122572
8.08	160.06	0.116359
9.08	160.06	0.110051
10.03	160.03	0.104175
11.03	160.03	0.098729
12.05	160.00	0.093040
13.03	159.98	0.088052
14.03	159.94	0.082966
14.94	159.93	0.078329
15.94	159.92	0.073708
16.94	159.91	0.068969
17.94	159.87	0.064732
18.94	159.85	0.060460
19.94	159.83	0.056541
20.94	159.84	0.052797
21.94	159.81	0.049419
22.94	159.82	0.046074
23.94	159.84	0.043183
25.02	159.82	0.039789
26.02	159.83	0.037316
27.02	159.81	0.035126
28.02	159.85	0.033664
29.02	159.83	0.032816
30.02	159.85	0.032343
31.02	159.84	0.032019
32.02	159.84	0.031802
33.02	159.83	0.031656
34.02	159.83	0.031557

Table E.3: Evolution of potato sample mass during SSD drying at $T_{steam} = 160$ °C (Exp. 3).

Time (min)	Drying chamber temperature (°C)	Sample mass (g)
0.00	159.21	0.153985
1.02	159.41	0.162585
2.00	159.75	0.154658
3.00	159.95	0.146576
4.00	160.06	0.138587
5.00	160.11	0.130888
6.02	160.10	0.123217
7.00	160.06	0.116191
8.08	160.00	0.108318
9.08	159.97	0.101531
10.10	159.88	0.094787
11.08	159.87	0.088309
12.08	159.83	0.082441
13.08	159.81	0.076315
14.08	159.76	0.070547
15.10	159.73	0.065168
16.08	159.74	0.059962
17.08	159.75	0.055463
17.99	159.70	0.051228
18.99	159.65	0.046490
19.99	159.63	0.042460
20.99	159.64	0.038682
21.99	159.62	0.035771
22.99	159.62	0.033266
23.99	159.63	0.031772
24.99	159.64	0.031159
26.00	159.61	0.030746
27.00	159.62	0.030469

Table E.4: Evolution of potato sample mass during SSD drying at $T_{steam} = 180\text{ }^{\circ}\text{C}$ (Exp. 1).

Time (min)	Drying chamber temperature ($^{\circ}\text{C}$)	Sample mass (g)
0.00	179.98	0.144237
1.02	180.60	0.149474
2.00	181.11	0.138710
3.00	181.36	0.128325
4.00	181.48	0.117945
5.00	181.56	0.108101
6.02	181.62	0.098576
7.00	181.63	0.089461
8.07	181.65	0.080347
9.08	181.64	0.071561
10.08	181.45	0.062962
11.08	181.12	0.055749
12.10	180.89	0.048486
13.08	180.73	0.042217
14.08	180.60	0.036085
15.08	180.49	0.030878
16.08	180.45	0.027156
17.10	180.42	0.025574
18.01	180.41	0.025117
19.01	180.41	0.024903
20.01	180.38	0.024773
21.01	180.38	0.024694
22.01	180.35	0.024637
23.01	180.33	0.024599
24.01	180.32	0.024557
25.01	180.29	0.024521
26.01	180.28	0.024500
27.01	180.31	0.024469

Table E.5: Evolution of potato sample mass during SSD drying at $T_{steam} = 180$ °C (Exp. 2).

Time (min)	Drying chamber temperature (°C)	Sample mass (g)
0.00	179.65	0.147405
1.00	179.81	0.153455
2.00	180.21	0.142489
3.00	180.32	0.132243
4.00	180.38	0.122225
5.00	180.37	0.112448
6.00	180.31	0.103388
7.00	180.29	0.094124
7.83	180.29	0.08737
9.08	180.12	0.077247
10.08	180.38	0.069384
11.08	180.48	0.061981
12.08	180.49	0.054686
13.08	180.38	0.047567
14.08	180.28	0.041006
15.08	179.97	0.035526
16.08	180.09	0.031347
17.08	180.14	0.029226
17.91	180.21	0.028635
18.99	180.29	0.028337
20.01	180.27	0.028181
20.99	180.34	0.028085
21.99	180.3	0.028018
22.99	180.31	0.027976
23.99	180.33	0.027931
25.01	180.29	0.027902
25.99	180.28	0.027869
26.99	180.22	0.027851
27.99	180.21	0.027821

Table E.6: Evolution of potato sample mass during SSD drying at $T_{steam} = 180\text{ }^{\circ}\text{C}$ (Exp. 3).

Time (min)	Drying chamber temperature ($^{\circ}\text{C}$)	Sample mass (g)
0.00	179.54	0.158924
1.00	179.82	0.166361
2.00	180.14	0.15555
3.00	180.32	0.145305
4.00	180.36	0.135008
5.00	180.28	0.125281
6.00	180.22	0.115884
6.83	180.16	0.108133
8.07	180.04	0.097208
9.07	180.00	0.088418
10.07	179.93	0.080192
11.07	179.93	0.072555
12.07	179.87	0.065314
13.07	179.86	0.057748
14.07	179.82	0.050961
15.07	179.79	0.044611
16.07	179.8	0.039229
16.91	179.78	0.035387
18.15	179.76	0.031357
19.00	179.76	0.029667
19.98	179.77	0.028771
20.98	179.79	0.028442
21.98	179.77	0.028263
22.98	179.77	0.028151
24.00	179.74	0.028085
24.99	179.75	0.028032
25.99	179.73	0.027994

Table E.7: Evolution of potato sample mass during SSD drying at $T_{steam} = 200$ °C (Exp. 1).

Time (min)	Drying chamber temperature (°C)	Sample mass (g)
0.00	199.30	0.15861
1.00	199.28	0.162194
2.02	199.31	0.148203
3.00	199.39	0.135179
4.00	199.42	0.12318
5.00	199.42	0.110857
6.00	199.41	0.099751
8.08	199.38	0.077396
9.08	199.36	0.067904
10.08	199.33	0.058142
11.10	199.31	0.050094
12.08	199.30	0.043499
13.08	199.36	0.038385
14.08	199.39	0.034961
15.08	199.41	0.033982
16.10	199.43	0.033631
17.33	199.46	0.033439
17.99	199.49	0.033367
18.99	199.46	0.033269
20.00	199.46	0.033232
21.00	199.46	0.033187
22.00	199.43	0.03315
23.00	199.43	0.033114
24.00	199.44	0.033088
25.00	199.42	0.033059
26.05	199.38	0.03304
26.55	199.40	0.033028

Table E.8: Evolution of potato sample mass during SSD drying at $T_{steam} = 200$ °C (Exp. 2).

Time (min)	Drying chamber temperature (°C)	Sample mass (g)
0.00	199.88	0.152312
1.00	199.55	0.178718
2.02	199.92	0.164293
3.00	200.07	0.151034
4.00	200.07	0.138664
5.00	199.93	0.126594
6.00	199.79	0.114944
7.02	199.67	0.103792
8.00	199.62	0.093513
9.01	199.53	0.082303
10.01	199.46	0.071472
11.10	199.42	0.061263
12.08	199.42	0.052835
13.08	199.39	0.045015
14.08	199.37	0.038775
15.08	199.34	0.034232
16.10	199.31	0.031385
17.08	199.37	0.030581
18.08	199.35	0.030312
19.08	199.30	0.030177
20.08	199.30	0.030088
21.10	199.31	0.030017
22.08	199.30	0.029964

Table E.9: Evolution of potato sample mass during SSD drying at $T_{steam} = 200$ °C (Exp. 3).

Time (min)	Drying chamber temperature (°C)	Sample mass (g)
0.00	199.88	0.153034
1.00	199.55	0.178718
2.02	199.92	0.164293
3.00	200.07	0.151034
4.00	200.07	0.138664
5.00	199.93	0.126594
6.00	199.79	0.114944
7.02	199.67	0.103792
8.00	199.62	0.093513
9.01	199.53	0.082303
10.01	199.46	0.071472
11.10	199.42	0.061263
12.08	199.42	0.052835
13.08	199.39	0.045015
14.08	199.37	0.038775
15.08	199.34	0.034232
16.10	199.31	0.031385
17.08	199.37	0.030581
18.08	199.35	0.030312
19.08	199.30	0.030177
20.08	199.30	0.030088
21.10	199.31	0.030017
22.08	199.30	0.029964

Peer-review journal/conference proceeding papers

1. **Kieu Hiep Le**, Abdolreza Kharaghani, Christoph Kirsch and Evangelos Tsotsas. *Pore network simulations of heat and mass transfer inside the porous wick of loop heat pipe evaporators*. *Transport in Porous Media* 114(3), 623-648. DOI: 10.1007/s11242-016-0737-4.
2. **Kieu Hiep Le**, Abdolreza Kharaghani, Christoph Kirsch and Evangelos Tsotsas. *Discrete pore network modeling of superheated steam drying*. *Drying Technology* 33(13), 1584-1601, DOI: 10.1080/07373937.2016.1264414.
3. **Kieu Hiep Le**, Neli Hampel, Abdolreza Kharaghani, Andreas Bück and Evangelos Tsotsas. *Superheated steam drying of single wood particles: A characteristic drying curve model deduced from continuum model simulations and assessed by experiments*. *Drying Technology* (accepted).
4. **Kieu Hiep Le**, Evangelos Tsotsas and Abdolreza Kharaghani. *Continuum-scale modeling of superheated steam drying of cellular plant porous media*. *International Journal of Heat and Mass Transfer* (submitted).
5. **Kieu Hiep Le**, Abdolreza Kharaghani and Evangelos Tsotsas. *Pore network simulation of heat and mass transfer in superheated steam drying*. 5th European Drying Conference (EuroDrying'2015), October 21-23, 2015, Budapest, Hungary, ISBN: 978-963-9970-62-5.
6. **Kieu Hiep Le**, Abdolreza Kharaghani and Evangelos Tsotsas. *Pore network simulations of superheated steam drying*. International Congress on Particle Technology (PARTEC 2016), April 19-21, Nuremberg, Germany.
7. **Kieu Hiep Le**, Abdolreza Kharaghani, Christoph Kirsch and Evangelos Tsotsas. *Discrete pore network modeling of superheated steam drying*. 20th International Drying Symposium (IDS 2016), August 7-10, 2016, Gifu, Japan.
8. **Kieu Hiep Le**, Abdolreza Kharaghani and Evangelos Tsotsas. *Water diffusion across cellular membrane during superheated steam drying: A continuum-scale approach*. 18. Forschungskolloquium am Fraunhofer IFF Magdeburg, November 25, 2016, Magdeburg, Germany, ISSN: 21918783.
9. **Kieu Hiep Le**, Abdolreza Kharaghani and Evangelos Tsotsas. *Impact of heating modes on the behavior of superheated steam drying in capillary porous media*. 6th

European Drying Conference (EuroDrying'2017), June 19-21, 2017, Liège, Belgium.

10. **Kieu Hiep Le**, Neli Hampel, Thi Thu Hang Tran, Evangelos Tsotsas and Abdolreza Kharaghani. *Simulations and experiments on superheated steam drying: From a single porous particle to a batch fluidized bed dryer*. 19th Forschungskolloquium am Fraunhofer IFF Magdeburg, November 25, 2017, Magdeburg, Germany.

Conference presentations (oral and poster)

1. **Kieu Hiep Le**, Abdolreza Kharaghani and Evangelos Tsotsas. *Pore network simulations of fluid transport in capillary porous wick*. 7th International Conference on Porous Media & Annual Meeting (INTERPORE 2015) (oral presentation), May 18 - 21, Padova, Italy.
2. **Kieu Hiep Le**, Abdolreza Kharaghani and Evangelos Tsotsas. *Pore network modelling of transport processes inside a capillary porous wick*. Annual Meeting of ProcessNet Working Party on Heat and Mass Transfer (oral presentation), March 01 – 02, 2016, Kassel, Germany.
3. **Kieu Hiep Le**, Abdolreza Kharaghani and Evangelos Tsotsas. *Pore network simulation of heat and mass transfer in superheated steam drying*. 5th European Drying Conference (EuroDrying'2015) (poster presentation), October 21-23, 2015, Budapest, Hungary, ISBN: 978-963-9970-62-5.
4. **Kieu Hiep Le**, Abdolreza Kharaghani and Evangelos Tsotsas. *Pore network simulations of superheated steam drying*. International Congress on Particle Technology (PARTEC 2016) (oral presentation), April 19-21, Nuremberg, Germany.
5. **Kieu Hiep Le**, Abdolreza Kharaghani, Christoph Kirsch and Evangelos Tsotsas. *Discrete pore network modeling of superheated steam drying*. 20th International Drying Symposium (IDS 2016) (oral presentation), August 7-10, 2016, Gifu, Japan.
6. **Kieu Hiep Le**, Abdolreza Kharaghani and Evangelos Tsotsas. *Water diffusion across cellular membrane during superheated steam drying: A continuum-scale approach*. 18. Forschungskolloquium am Fraunhofer IFF Magdeburg (oral presentation), November 25, 2016, Magdeburg, Germany, ISSN: 21918783.
7. **Kieu Hiep Le**, Evangelos Tsotsas and Abdolreza Kharaghani. *3D pore network modeling of superheated steam drying process within a capillary porous medium* First German National Chapter Meeting of Interpore (poster presentation), December 4 - 6, 2016, Leipzig, Germany.
8. **Kieu Hiep Le**, Arman Rahimi, Christoph Kirsch, Abdolreza Kharaghani and Evangelos Tsotsas. *Impact of heating modes on superheated steam drying characteristics of capillary porous media*, Annual Meeting of ProcessNet Working Party on Drying (poster presentation), March 01 – 02, 2017, Kassel, Germany.

9. **Kieu Hiep Le**, Abdolreza Kharaghani, Christoph Kirsch and Evangelos Tsotsas. *An investigation of pore condensation during superheated steam drying process involved in a capillary porous medium*. 9th International Conference on Porous Media & Annual Meeting (Interpore 2017) (short oral presentation), May 8 - 11, 2017, Rotterdam, Netherlands.
10. **Kieu Hiep Le**, Abdolreza Kharaghani and Evangelos Tsotsas. *Impact of heating modes on the behavior of superheated steam drying in capillary porous media*. 6th European Drying Conference (EuroDrying'2017) (poster presentation), June 19-21, 2017, Liège, Belgium.
11. **Kieu Hiep Le**, Neli Hampel, Abdolreza Kharaghani and Evangelos Tsotsas. *Heat and mass transfer involved in a single wood particle during the superheated steam drying process*. Annual Meeting of ProcessNet Working Party on Heat and Mass Transfer (submitted), March 06 - 07, 2018, Bremen, Germany.
12. Neli Hampel, **Kieu Hiep Le**, Abdolreza Kharaghani, Andress Bück and Evangelos Tsotsas. *Heißdampftrocknung: Kinetik, produktqualität modellbasierte beschreibung des prozesses*. Annual Meeting of ProcessNet Working Party on Drying (submitted), February 26 - 28, 2018, Merseburg, Germany.

Student works conducted in the frame of this thesis

1. Saeedeh Imani Moqadam. *Superheated steam drying of porous materials: Model development and parametric study*. Master thesis supervised by M.Sc. **Kieu Hiep Le** and Dr.-Ing. Abdolreza Kharaghani, Otto von Guericke University Magdeburg, 2016.

Curriculum Vitae

Personal Data

Name	Kieu Hiep Le
Date of birth	March 20, 1985
Place of birth	Ha Tinh, Vietnam
Nationality	Vietnamese

Education

2014-present:	Otto von Guericke University, PhD in Thermal Process Engineering
2008-2010	Hanoi University of Technology and Science, M.Sc. Heat and Refrigeration Engineering
2003-2008	Hanoi University of Technology and Science, B.Sc. Heat and Refrigeration Engineering

Work experience

2008-2014	Hanoi University of Technology and Science, Lecturer in Thermal Engineering Department
-----------	---